Constraining seismic hazard in the Pacific Northwest through observation and direct modeling of earthquakes

Ian Patrick Stone

A dissertation

submitted in partial fulfillment of the

requirements for the degree of

Doctor of Philosophy

University of Washington

2020

Reading Committee:

Erin A. Wirth, Chair

Kenneth C. Creager

John E. Vidale

Program Authorized to Offer Degree:

Department of Earth and Space Sciences

University of Washington

Abstract

Constraining seismic hazard in the Pacific Northwest through observation and direct modeling of earthquakes

Ian Patrick Stone

Chair of the Supervisory Committee:

Erin A. Wirth

Department of Earth and Space Sciences

In this dissertation, we seek to expand knowledge of the processes controlling seismic hazard in the Pacific Northwest through observing and interpreting earthquake records, as well as through directly modeling earthquake source processes.

In Chapter 2, we develop a catalog of earthquakes occurring in the vicinity of the Cascadia Subduction Zone using a four-year dataset of seismograms recorded with ocean bottom seismometers (OBS). We locate 271 earthquakes of M0.4-4.0 with epicenters in or directly adjacent to the subduction zone. The distribution of near-interface seismicity shows distinct along-strike variability, which we associate with changes in plate deformation and the amount of subducted sediments. Earthquakes off the coast of Vancouver Island and Northern Washington are typically sparse, coinciding with a relatively undeformed subducting plate and a thin layer of

subducted sediments. Near-interface seismicity is relatively abundant off Southern Washington and Northern Oregon, where subduction bending has roughened the lower plate and where entrained sediments are still relatively thin. Seismicity abruptly decreases between Central and Southern Oregon. Despite significant deformation in the subducting plate, seismicity is only clustered in a few distinct swarms. We suggest this is due to a thick layer of largely unconsolidated sediments entering the subduction zone at this location, which encourages geodetically observed partial creeping; the earthquake swarms are likely related to seamounts on the subducting plate, which pierce through the thick sediment sequence to come in contact with the overriding plate. In Southern Oregon and Northern California, seismicity is abundant, corresponding with very little entrained sediments and a subducting slab significantly deformed by the complex plate interactions near the Mendocino Triple Junction.

In Chapter 3, we explore the effect of topography on earthquake ground motion during finite fault ruptures by directly modeling M7 earthquakes on the Seattle Fault. Our study focuses on a ~60 X 60 km region centered on the Seattle Fault and simulates seismic wave propagation via a spectral element method (SEM) code. We accurately model ground motion up to 3 Hz using a realistic 3-D velocity model and a model mesh built with a 30 m topographic surface. We ultimately test nine different kinematic rupture scenarios, in which we vary the slip distribution and hypocenter location, to judge the sensitivity of topographic amplification to kinematic rupture parameters. We demonstrate that adding topography to a simulation does not significantly change the average strength of ground motion; however, amplification of shaking is common, with over a quarter of the model area experiencing short period (≤2 s) ground motion 25-35% greater than in a flat simulation. This amplification typically occurs at the top of topographic features, while the bottom of features experience either less amplification or de-

amplification. S- and surface waves are more affected by amplification than P-waves. Amplification is sensitive to period, with ground motion experiencing the greatest amplification near a feature's analytically predicted resonance frequency; shaking is also typically greatest at azimuths perpendicular to a feature's primary axis of elongation. However, topographic response shows a strong sensitivity to kinematic rupture parameters, particularly at periods <1 s. Our results suggest that while topographic resonance does contribute to the ground motion modeled on a feature, other processes (e.g., localized focusing, improved free surface incidence, and scattering) also play a significant role in determining topographic response.

In Chapter 4, we map depth to basement and calculate Qp-Qs relations in the Seattle and Tualatin Basins using converted seismic phases. We identify P-, P-to-S (Ps), S-to-P (Sp), and S-wave phase arrivals in records of earthquakes observed near these basins. The Ps and Sp phases are assumed to represent conversions off of the crystalline basement beneath the basins, as well as at interfaces within the basins. By looking at the relative arrival times between the parent and converted phases, we are able to calculate depth to basement in both the Seattle and Tualatin Basins using a simple velocity model. These depth values are generally similar to those predicted by other active and passive source geophysical methods. In addition, by taking the spectral ratio of the converted and parent phases, we determine the average Qp-Qs relationships within each basin. Through comparisons with linear Qp/Qs relationships, we find that the average Qp value in the Seattle Basin is near 71, while average Qs is near 60 for waves with frequencies between 2-25 Hz. In the Tualatin Basin, the Qp-Qs relationship suggests that average body wave attenuation is higher than in the Seattle Basin

Table of Contents

List of Figures

List of Tables

I. Introduction

The Pacific Northwest is one of North America's most seismically active regions. In the broadest sense, this hazard is the result of continent-scale collisions between the North American, Pacific, and Juan de Fuca tectonic plates, which are in a constant state of motion relative to one another.

Just off the coast, the Juan de Fuca plate thrusts beneath North America at a rate of 3-4 cm/year (DeMets et al., 2010). This process has formed the Cascadia Subduction Zone, a thousand-kilometer-long fault stretching from British Columbia to Northern California. Paleoseismic investigations have revealed that this fault is capable of producing large magnitude (M8+) earthquakes, the greatest of which rupture the entire subduction zone in single magnitude 9 events. These "megathrust" earthquakes occur on average every 400-500 years, the last of which happened in the year 1700 AD (Goldfinger et al., 2012). Besides generating widespread strong ground motions at the coast, these events have produced tsunamis significant enough to inundate villages in coastal Japan (Satake et al., 2003).

As the Juan de Fuca plate subducts, it releases fluids that increase intraplate pore pressures. This process encourages brittle fracturing within the plate as it bends down into the mantle and occasionally results in significant normal faulting earthquakes (i.e., Wadati-Benioff zone earthquakes) (Wada et al., 2008). These largest of these events tend to cluster beneath the Puget Sound region of Washington and have focal depths between 40-60 km. Over the last century, several of these events have had significant magnitudes (>M6), the last of which was the 2001 M6.8 Nisqually earthquake. Though not as large as earthquakes in the subduction zone, these events are more common and occur much closer to large population centers.

At the south end of the Cascadia Subduction Zone, all three plates meet at the Mendocino Triple Junction. The abrupt south-to-north transition from a transform plate boundary to a convergent boundary produces a complex stress field, which leads to deformation in all three plates. Within the North American plate, the incipient northward propagation of the transform boundary and the oblique northeast subduction of the Juan de Fuca plate results in broad, clockwise rotation of the Pacific Northwest (Wells et al., 1998). The resulting deformation is not uniformly distributed. The sturdy Sierra Nevada and Oregon Coast crustal blocks translate to the north as singular units. British Columbia, sitting well away from the triple junction, is largely stationary with respect to the rest of the North American plate. As a result, Western Washington is subject to north-south compression, which is facilitated by a series of subparallel reverse faults. The most notable of these features are the Seattle, Tacoma, and South Whidbey Island Faults, which cross the Puget Sound and have collectively accommodated tens of kilometers of compression over the Cenozoic (Pratt et al., 1997). Each of these faults is capable of producing M6+ earthquakes, with the potential to severely impact the population- and infrastructure-heavy region. The Seattle Fault, which passes just south of downtown Seattle, has produced several M6.5+ earthquakes in the last 16 kyrs, the last of which was an ~M7 event that occurred in the year 900 AD (Bucknam et al., 1992; Nelson et al., 2003). Besides generating extreme localized ground motion, a repeat of this event today would likely result in widespread landslides throughout the city, as well as localized tsunamis and liquefaction.

Despite the abundance of seismic sources, strong earthquakes are not as common in the Pacific Northwest as in other parts of the country (e.g., California and Alaska). This quiescence is both a source of relief and concern. A lack of devastating earthquakes has allowed the region to go relatively unscathed by significant quakes over the last century. But our understanding of

seismic hazard (particularly, the ways in which an earthquake from a given source will control ground motions at a given location) is largely driven by direct observation of earthquakes. Only a handful of large earthquakes have struck the region since written records have been kept. Even fewer have occurred in the era of modern seismological instrumentation. As a result, we have an incomplete understanding of the region's seismic hazard.

Fortunately, by studying seismic sources, the geology of the region, and the ways in which site conditions affect ground motions, we can continue to grow and improve the body of knowledge surrounding the region's seismic hazard. In this thesis, we address three questions about earthquake science in the Pacific Northwest through observation of earthquake records, and through direct modeling of earthquake ground shaking.

In Chapter 2, we seek to characterize the present-day distribution of microseismicity in the Cascadia Subduction Zone through developing a catalog of earthquakes observed on ocean bottom seismometers (OBS). By applying a modified short-term-average/long-term-average filtration method, we are able to locate 271 earthquakes with magnitudes between M0.4-4.0 in and directly adjacent to the subduction zone. Earthquakes are located using a velocity model considerate of the complex geology on the plate boundary. We observe that the distribution of near-interface earthquakes is highly variable along the strike of the subduction zone. We attribute this variability to differences in deformation in the subducting plate and the amount of subducted sediments, which controls the roughness and hydration of the plate interface.

In Chapter 3, we explore how much topography could affect ground motions in and around Seattle during an M7 earthquake on the Seattle Fault. To constrain amplification due to topography, we directly simulate ground motions using a spectral element method (SEM) code and a kinematic finite fault source. By employing a mesh with a 30 m topographic surface and a

realistic 3-D velocity model, we are able to model ground motions up to 3 Hz. Our analysis shows that adding topography to the simulation only marginally increases average ground motions (<5%); however, a quarter of sites experience ground motions amplified by more than 25-35%. This amplification, which primarily affects S- and surface waves, is generally greatest on a given topographic feature near a characteristic resonance frequency and at an azimuth perpendicular to the feature's primary axis of elongation. However, while amplification is influenced by topographic resonance, we demonstrate that the response during any one earthquake is also significantly affected by other localized seismic wave phenomena, like focusing, improved free surface incidence, and scattering.

Finally, in Chapter 4, we use converted phases in local earthquake records to calculate the depth to basement and Qp-Qs attenuation relationships in the Seattle and Tualatin Basins. Recordings of local earthquakes in these basins are shown to contain P- and S-wave arrivals that correspond to converted phases generated at basin/basement boundaries, as well as at internal layer boundaries. By using simple 1-D velocity models, we estimate the depth to basement in both of these basins, producing depth values similar to those estimated by other geophysical methods. Then, by taking the spectral ratio of the parent and converted wave phases, we are able to estimate the Qp-Qs relationships in each basin, showing that body wave attenuation in the Tualatin Basin is likely greater than that in the Seattle Basin.

II. Catalog of off-shore seismicity in Cascadia: Insights into the regional distribution of microseismicity and its relation to subduction processes

The content of this chapter was published in:

Stone, I., Vidale, J. E., Han, S., and Roland, E. (2018). Catalog of off-shore seismicity in Cascadia: Insights into the regional distribution of microseismicity and its relation to subduction processes. *Journal of Geophysical Research – Solid Earth*, *123* (1). Pp. 641-652. http://doi.org/ 10.1002/2017JB014966.

1. Introduction

The Cascadia subduction zone (CSZ), located off the coast of northwestern North America, facilitates a continent-scale collision between the Juan de Fuca (JdF) and North American tectonic plates. Here the JdF, which can be subset into into a central primary plate flanked to the north and south by the smaller Explorer and Gorda plates (Dziak et al., 2011; Gulick et al., 2001; Hyndman et al., 1979; Wilson, 1993), thrusts northeastwardly at 30-45mm/yr (DeMets et al., 2010) into the upper-mantle beneath North America. This collision creates a thousand-kilometer-long "megathrust" fault, which extends from the Queen Charlotte triple junction off Vancouver Island to the Mendocino triple junction off California. An extensive regional paleoseismic record indicates that the CSZ has hosted dozens of megathrust earthquakes in the past, with M8+ events occurring at ~250 year intervals, and ~M9, full-margin events at ~500 year intervals (Goldfinger et al., 2003, 2012). The last such M8+ event in Cascadia happened in the year 1700, when a M~9 event ruptured the full length of the subduction zone

(Satake et al., 2003), and the only other historically recorded major event was the 1992 M7.2 Petrolia earthquake, which occurred just north of the Mendocino triple junction (Oppenheimer et al., 1993). Observations of present day microseismicity along the margin are sparse, and only a handful of these events are believed to have occurred on the megathrust itself. While the CSZ's quiescence may be related to relatively low rates of convergence and near-total locking on the plate interface (Wang & Tréhu, 2016), the paucity of observed events may be partially attributed to difficulty in monitoring.

Regional seismic networks, like the Pacific Northwest Seismic Network (PNSN), the Northern California Seismic Network (NCSN), the Canadian National Seismograph Network (CNSN), and the USArray transportable array (TA) deployment have provided the majority of our seismic observations of the CSZ. Despite covering an extensive geographic area, these networks are almost exclusively based on land. Because the CSZ's seismogenic zone is primarily offshore (Hyndman & Wang, 1995; McCaffrey et al., 2013; Schmalzle et al., 2014), seismic records of offshore events can be noisy with large azimuthal gaps, and smaller earthquakes are often missed altogether. Further, the velocity models used by the networks for locating offshore events have been necessarily simplified, failing to account for the complex source-to-receiver ray-paths and lateral heterogeneities associated with the plate interface. As a result, significant location errors have been documented in some offshore event records (Tréhu et al., 2008, 2015; Williams et al., 2011). This implies that areas along the subduction zone with sparse, azimuthally restricted coverage and poor velocity characterization likely have severely biased earthquake locations.

Considering the disadvantages of using land-based seismic networks to monitor the subduction zone, offshore recordings of earthquakes are extremely valuable for determining

more precise seismicity rates and earthquake locations. Offshore seismometer arrays are closer to the megathrust while also having source-to-receiver paths that are simpler than those associated with land-based networks. However, deploying and maintaining ocean bottom seismometers (OBS) or cabled arrays is difficult both technically and logistically; and until recently, only a handful of studies utilizing OBS networks had been conducted on the CSZ.

Dziak et al. (2011) reviewed hydroacoustic data from 1991 to 2008 recorded on the US Navy's submarine Sound Surveillance System (SOSUS) across the entire JdF and the CSZ. This work, which analyzed earthquake T-phases propagating through the North Pacific Ocean, cataloged over 45,000 earthquakes within and along the margins of the JdF. While the majority of these events were associated with spreading ridges and transform faults on the west and south edges of the JdF, many were located in the interior of the plate as well, with the highest rates of seismicity south of 46°N. Several hundred events were also recorded near the subduction zone.

Oregon State University deployed a 16-station short-period array of OBS off the coast of Newport, OR (~44.5°N), from September 2007 to July 2009 to monitor persistent swarm activity (Tréhu et al., 2012; Williams et al., 2011). These observations confirmed that there is seismic activity occurring directly on the plate interface. Further, these studies demonstrated that the PNSN was systematically overestimating the depth of offshore events. In 2010, the Seafloor Earthquake Array Japan-Canada Cascadia Experiment (Sea-Jade) collected continuous seismic data off the coast of Vancouver Island with a dense (~20km spacing) array positioned directly over the CSZ (Scherwath et al., 2011). Although only deployed for 3 months, this array detected over 1200 earthquakes, most of which were concentrated along the Nootka fault zone and in the forearc of the overriding plate (Obana et al., 2015).

In each of these studies, the use of OBS deployments and velocity models appropriate for offshore geologic structure provided more detailed, accurate, and complete observations than those from regional land-based networks alone. The success of such projects provided an impetus for pursuing significantly larger deployments offshore.

Subsequently, the Cascadia Initiative (CI) was developed and implemented. The CI was a four-year, community organized OBS experiment that spanned the entirety of the CSZ, as well as most of the JdF (Toomey et al., 2014). It was the largest deployment of OBS in the region to date, and it vastly improved regional seismometer coverage. In this study, we present a catalog of seismicity developed from CI records, focusing primarily on earthquakes with epicenters in and adjacent to the CSZ. Our primary objective was to develop a standard seismic catalog that utilized near-source, offshore stations associated with the CI, potentially capable of detecting and determining improved locations for events associated with the CSZ's seismogenic zone. Further, we sought to characterize along-strike variations in interplate slip behaviors and intraplate deformation using trends in observed seismicity. Earthquakes were detected using a short time average/long time average (STA/LTA) trigger and located using a combination of 1D velocity models developed from active source seismic surveys along the CSZ (Flueh et al., 1998; Gerdom et al., 2000). The results show a higher rate of seismicity in the subduction zone than was observed from land-based networks at the time of deployment. Further, the along-strike pattern of earthquake distribution supports observations that there are geologically and structurally distinct sections of the JdF that may affect seismic behavior in the subduction zone.

2. Data and Methods

The Cascadia Initiative was an NSF supported, onshore/offshore seismic and geodetic experiment developed to increase observational coverage of the CSZ and the JdF. During this

experiment, an OBS array was deployed off the coasts of Vancouver Island, Washington, Oregon, and Northern California. The array was emplaced in alternating northern and southern sections between 2011 and 2015, with each deployment consisting of 60-70 stations recording for approximately 10 months at a time. Station spacing varied depending on location, with stations on the JdF in a regular 70km grid, and near-shore stations in a less regular ~50km grid. There were also two dense arrays located on the continental shelf off Cape Mendocino, CA, and Grays Harbor, WA. The OBS recorded continuous broadband seismic timeseries at sampling rates of 50, 100, or 125sps, depending on the instrument and deploying institution.

We selected stations to use in the detection based on their proximity to the subduction zone, their geometry relative to other stations, and by the quality of the data they produced (Figure 2.1). These data were supplemented with records from EarthScope transportable array stations on land, as well as records from regional land-based seismic networks. To begin, we searched for earthquakes sorting STA/LTA ratios on vertical traces (years 1-4) and horizontal traces (years 2-4) filtered between 3 and 15 Hz. To be considered a detection, the amplitude of the ratio needed to exceed a threshold value for a given duration of time. We identified optimal threshold values by first inspecting offshore events recorded by the PNSN during the time of the CI deployment. Upon finding a range of values that maximized the detection of known events, we applied the values to several week-long portions of the CI data, ultimately choosing a single set of values to apply to an entire year. The chosen STA/LTA and threshold values are shown in Table 2.1.

After running a detection on a year of data, we associated triggers on the basis of arrival time and station location, and the resultant events were visually inspected for validity. For detections to be flagged as an event, association of detections on at least 3 adjacent stations was

required. We adjusted and added P- and S-phase arrivals by hand and relocated the events with a generic velocity model (IASP91). Locations were refined using phase picks from as many stations as possible, including CI and land stations not used in the initial detection. Even using the full deployment and land stations, events that occurred early or late in a particular year may suffer from poor coverage, as station siting and recovery spanned several weeks. Events from highly active areas that have already been characterized in recent studies, like the Nootka fault zone/Vancouver Island north of 48.5°N (Obana et al., 2015) and the Mendocino triple junction region south of 41°N (Chen & McGuire, 2016), were largely excluded from processing during the verification and location steps. Further, catalog completeness drops significantly ~70km west of the deformation front and ~30km east of the coastline, corresponding to the aerial distribution of detection stations in a given year.

After the initial location, events with epicenters within or directly adjacent to the CSZ were relocated using Hypoinverse (Klein, 2002). During processing, we employed the same program settings and velocity models used by the PNSN to locate offshore events, providing a means for direct comparison between events recorded by the PNSN and the CI. However, the 1D velocity models utilized by the PNSN do not adequately account for the large lateral heterogeneities present in the velocity structure offshore; depending on the location, offshore events were located with a velocity model representing continental crust or the JdF, neither of which reflect the sedimentary mélange and subducting plate beneath the continental shelf. Further, when iterating to find the event location, the PNSN adopts a relatively liberal phase arrival weighting scheme. Hypoinverse weights phase arrivals relative to the distance between the epicenter and the 2nd-nearest station (dx2). The PNSN gives non-zero weight to phase arrivals from stations up to 7-times-dx2, which is adequate for the land-based network, but is not

appropriate for the CI data, where station spacing was sparse and the velocity structure varied significantly over short distances.

To develop velocity models more attuned to the large lateral geologic heterogeneities, we started with the cross-sections presented in Flueh et al. (1998) and Gerdom et al. (2000) developed using active seismic surveys off the coasts of Washington and Oregon. Three 2D velocity models along lines SO10 and SO12 (Flueh et al., 1998) and profile 7 (Gerdom et al., 2000) were assigned to their corresponding regions: Northern Washington/Vancouver Island, Southern Washington, and Oregon/Northern California. Within these larger regional designations, we subdivided the area east of the CSZ trench and west of the shore into three 1D velocity models for input into Hypoinverse; these models correspond to the trench, shelf, and shoreward portions of the subduction zone. Areas outside of the subduction zone (east of the coastline and on the JdF) were assigned the 1D velocity models in use for those regions by the PNSN. To avoid abrupt transitions crossing from one velocity model to another, we designated 15-25km buffer zones between adjacent models; the velocity structure in these zones is a linear combination of the neighboring profiles. All velocity profiles are shown in Figure 2.2, and their corresponding spatial extent in Figure 2.3. A Vp/Vs ratio of 1.78 was used for all locations, which is the same ratio used by the PNSN. For the phase arrival weighting scheme, we adopted a more conservative distance relation. Phase arrivals within 1.5-times-dx2 are given full weight, and weights are tapered to zero by 4-times-dx2. As such, records from the nearest few stations are given full weight, while enough distant records are retained to reduce azimuthal gaps; very distant records (generally >150-200km) are not considered.

Magnitudes were determined using a modified version of the local magnitude calculation, wherein a 3-20Hz, 8-pole bandpass filter was applied to the data before typical magnitude

calculation. This step was added to account for low frequency noise, which overpowered earthquake signal and skewed magnitude values upward. Filtration parameters were chosen such that events recorded both by the CI and PNSN had similar magnitudes. Average deviation of CI magnitudes from PNSN magnitudes is less than 0.25 magnitude units (see supplemental material for an expanded discussion of our magnitude calculation).

3. Results

From the four years of CI data, we were able to locate 271 earthquakes with epicenters between the Cascadia deformation front and the coastline (Figures 2.4 & 2.5). These events have phase arrivals on at least 3 stations, with a median number of 13 phase arrivals per event. Two example events are shown in Figure 2.6 with predicted and operator phase picks highlighted. Based on the estimation of Hypoinverse, the median vertical standard error is 1.3km, and the median horizontal standard error is 2.0km (Klein, 2002, Appendix 4). 35 events have a vertical standard error greater than 10km. The majority of these high-uncertainty events are off Northern California and Vancouver Island, which correspond to the regions with the poorest velocity model characterization. The median root mean square misfit value (RMS) for the whole dataset was 0.46 seconds. As with location uncertainty, the majority of the 43 events with RMS greater than 1 second occur off Northern California.

The magnitudes of our detected earthquakes range from M0.4 to 4.0, with an average uncertainty of +/- M0.48 (Figure 2.7). The cumulative magnitude curves deviate somewhat from a typical Gutenberg-Richter (GR) distribution, both with respect to slope and smoothness, making it difficult to determine a magnitude of completeness (Mc) value. This deviation likely results from large variations in station distribution through the deployment, stringent detection thresholds to account for high noise, and a relatively small catalog size. The northern section of

the catalog (north of 46°N) seems to have the highest Mc value, with the slope of the cumulative magnitude curve deviating from a typical GR slope between M2.0-2.5, whereas the central and southern sections have Mc around M1.0 -1.5. This particular difference can be partially attributed to the limited extent of the detection stations in the first year, as well as the detection gap off central Washington resulting from noisy, unusable data. While this could affect the observed north-to-south distribution of lower magnitude events (<M2.0) and make it difficult to compare along strike variations in seismicity, it should be noted that when only comparing the number of higher magnitude events (>M2.0), the large-scale trends in along-strike seismicity persist. A similar comparison using only the PNSN catalog in the decade preceding the experiment (2006-2016) shows a similar trend, with higher magnitude events increasing in frequency from north to south.

The seismicity observed within the subduction zone can be subset into 3 major regions based on amount and clustering of activity: north (north of 46°N), central (46°N-43°N), and south (south of 43°N) (Figure 2.5). The north region is characterized by very sparse seismicity, with greater event frequency near the coast of Vancouver Island and the Nootka fault zone (Figure 2.4). Within the central region, activity is associated primarily with the previously identified swarms off Newport, OR, between 44.3°N and 44.7°N (Tréhu et al., 2015), though there is also an active zone of seismicity between 46°N and 45°N. Events in this region are distributed across a wide range of depths, extending from the surface down to the interior of the subducting JdF plate (Figure 2.5B). In the southern region, seismicity is abundant and widespread, also spanning a wide range of depths (Figure 2.5C). While many earthquakes were recorded in the historically active region off Northern California near the Mendocino triple junction, many earthquakes were also observed off southern Oregon and Northern California

between 43°N and 41°N as well, including an active swarm at 42.2°N and 124.7°W with ~60 events.

An additional 440 events were located in the incoming plates west of the deformation front (Figure 2.8). These events were located with only the IASP91 velocity model and are generally associated with higher uncertainty in location. The completeness of this portion of the catalog is strongest within ~70km of the CSZ, where the events fall within the subset of stations used during event detection. We observe abundant earthquakes along the Blanco fracture zone and some earthquakes associated with the Nootka fault zone. In the outer rise region of the incoming JdF plate, the distribution of earthquakes shows a distinct N-S difference across 46°N (Figure 2.8). Very few earthquakes are detected offshore Washington, whereas abundant earthquakes are observed south of 46°N offshore Oregon. Offshore Northern California, many earthquakes are detected in the incoming Gorda plate.

During the time of deployment, the PNSN recorded 53 events between the coastline and the deformation front. Of these, 38 were also detected within the CI data; our catalog includes 139 events not detected by the PNSN in its reporting area. Those not detected in the CI data generally occurred during the time of station siting or retrieval, or were too weak to be detected on the requisite 3 stations. Within the NCSN reporting area north of 41°N, 17 events occurred during the deployment, 7 of which were also detected in the CI data; our catalog includes 49 events not detected by the NCSN. In the CNSN catalog south of 49.2°N (south of the Nootka fault zone), 33 events were detected, only 9 of which were detected in the CI data; we located 2 events not detected by the CNSN. It should be noted that detection parameters were initially developed using records from the PNSN catalog, so less emphasis was necessarily given to locating all the events present in the NCSN and CNSN catalogs. Further, the lack of detection

stations north of 47°N during the deployment's first year likely impeded our ability to detect events occurring in the CNSN reporting area.

4. Discussion

Our catalog of offshore seismicity from 41˚N to 49˚N provides important information about the deformation of the incoming JdF and Gorda plates, as well as the Cascadia forearc. In the outer rise region of the incoming plates, our data reveal an abrupt transition across 46°N from extremely low seismicity in the north to high seismicity in the south. This trend mirrors seismicity rates observed in the SOSUS (Dziak et al., 2011) and land based catalogs, and suggests active deformation south of 46°N (Figure 2.8). This inference is consistent with structural observations from active source seismic studies (Canales et al., 2017; Gulick et al., 2001; Han et al., 2016, 2017; Horning et al., 2016). During the recent Ridge-to-Trench experiment, small offset normal faults confined to the upper-middle crust were imaged in the JdF seaward of the deformation front offshore Washington using multichannel seismic (MCS) reflection data. In contrast, offshore Oregon, large offset normal faults that transect the oceanic crust and extend ~6-7 km into the uppermost mantle were imaged, accompanied by a reduction in Vp in the lower crust (Han et al., 2016; Horning et al., 2016). Coincident MCS and OBS data from an along-strike line just seaward of the deformation front show a transition in crustal reflectivity and lower crustal Vp in the JdF near 45.8°N, suggesting more extensive faulting and a more fractured, hydrated crust offshore Oregon in comparison to Washington (Canales et al., 2017). Offshore of Northern California, where our catalog documents an even higher rate of seismicity in the incoming Gorda plate, normal faults originally formed near the Gorda ridge are reactivated under north-south compression across the Gorda-Pacific plate boundary as strike slip faults, causing extensive intraplate deformation (Gulick et al., 2001).

Between the deformation front and the coastline, our catalog shows significant north-south variations in the rate of seismicity at near-plate-interface depths (Figures 2.4 & 2.5). If these events are occurring on the plate boundary, this change in seismicity may reflect the locking status and distribution of asperities on the plate interface. Regardless of their source, it seems likely that the change in forearc seismicity rates within the CSZ is linked to the along-strike variations in deformation of the incoming plates, as well as to the amount of subducted sediments (Han et al., 2016, 2017; Horning et al., 2016). Both factors affect the roughness/smoothness of the plate interface and the amount of fluid entering the subduction zone, which are important for megathrust slip behavior (Nishikawa & Ide, 2017; Saffer & Tobin, 2011; Wang & Bilek, 2014), as well as the strength and heterogeneity of the subducting slab. In addition, actively deforming strike-slip faults mapped in the overriding North American plate may account for a portion of the increased forearc seismicity observed in southern Cascadia (Gulick & Meltzer, 2002).

Here we elaborate on the possible causes of seismicity within the CSZ from north to south. A region-by-region comparison of the influence from underthrust sediments and incoming plate deformation on possible near-plate-interface seismicity is shown in Table 2.2. In the northern region (north of 46°N), only 33 earthquakes were detected during the OBS deployment period. The relative scarcity of earthquakes on the plate interface offshore Washington mirrors the lack of interface seismicity observed off Vancouver Island during the 3 month SeaJade OBS deployment (Obana et al., 2015). This regionally subdued rate of interplate seismicity is consistent with a pervasively locked megathrust north of 46°N, as indicated by land-based geodetic observations (Burgette et al., 2009; McCaffrey et al., 2013; Schmalzle et al., 2014). In this region, the incoming JdF is also less deformed than in its southern portion; the top of the

oceanic crust is comparatively smooth with relief less than 150m (Canales et al., 2017; Han et al., 2016). Over-consolidated sediments are observed near the deformation front and in the outer wedge, with sediments ≤600m thick being subducted (Adam et al., 2004; Booth-Rea et al., 2008; Han et al., 2017). The inferred smooth and fluid-poor interface is favorable for strain accumulation over a larger region.

In the central region (43°N-46°N), many of our detected earthquakes are scattered around the previously identified earthquake clusters between 44.3°N and 44.7°N (Tréhu et al., 2008, 2012, 2015). These clusters have generated several moderately sized earthquakes (M4+) in the past with foci near or on the plate interface (Tréhu et al., 2015), and subspace detection of first-year CI timeseries gathered near the cluster has indicated the presence of active ongoing microseismicity (Morton & Bilek, 2015). Some events from this cluster have been large enough to develop focal mechanisms, most of which show motion characteristic of low-angle thrusting (Tréhu et al., 2012; Williams et al., 2011). Outside of the clusters, the region has had very little observed seismicity. Offshore Central Oregon, partial creeping of the plate interface has been inferred from the land-based geodetic data (Schmalzle et al., 2014). Here a thick sequence (1.4-1.7 km) of under-consolidated sediments are subducting beneath the forearc (MacKay, 1995; MacKay et al., 1992). The abundant fluid contained in the underthrust sediments along with the permeability structure of the upper plate (Schmalzle et al., 2014) may contribute to the partial creeping of plate interface, which might account for the general lack of seismicity outside of the clusters. Near the earthquake clusters, tomographic, seismic, and magnetic observations indicate the possible presence of a group of subducting seamounts, which could pierce through the sediment sequence and come in contact with the rigid overriding plate (Tréhu et al., 2012; Williams et al., 2011). The earthquakes detected near these clusters in our catalog are distributed

over a depth range of ~10km in both the upper plate and lower plate. If this depth distribution is true, it may indicate that as the seamounts subduct, faults and fractures develop in both the upper and lower plates, which generate small earthquakes and create heterogeneous stress on the plate interface (Wang & Bilek, 2014). Between 45°N and 46°N, earthquakes are observed over a wide spatial range near the plate interface. With less subducted sediments (≤400m thick) (Booth-Rea et al., 2008; Han et al., 2017; MacKay, 1995) and extensive subduction bending deformation in the oceanic crust, the plate interface in this region may be rougher in comparison to the 43°N-45°N region, and has conditions favorable for the generation of small earthquakes.

In the southern region (south of 43°N), abundant earthquakes are detected in the upper plate, near the plate interface, and in the subducting plate. While a high level of seismicity south of 41°N was previously observed from land-based seismic networks, attributed largely to the effect of the Mendocino triple junction on the forearc and the warping of the slab (McCrory et al., 2012), this is the first time that many small earthquakes have been detected in the expected depth range of the plate interface between 41°N and 43°N. If these events are happening on the plate interface, it may be linked to relatively thin subducted sediments (250-600m) (Gulick et al., 1998), and pervasive large-offset faults within the Gorda plate caused by north-south compression (Gulick et al., 2001). The combined effect of these two factors are a relatively rough plate interface and a significantly hydrated oceanic crust. Further, the Blanco fracture zone is subducted near 42.5°N, separating the Gorda plate from the Juan de Fuca plate. This shear zone and two nearby pseudofaults represent major topographic offsets at the basement (Goldfinger et al., 2012) and may locally enhance hydration of the oceanic crust. The associated stress and pore fluid pressure heterogeneities at the plate interface could give rise to small earthquakes in this region.

Shallow, near-shore earthquakes occurring in the southern region's upper plate forearc may represent oblique-slip and transpressional faulting. Seismic reflection surveys within the Eel River forearc basin just north of the Mendocino triple junction have mapped a number of active faults in the upper plate (Gulick & Meltzer, 2002). These faults may accommodate the incipient northward propagation of the Pacific-North American transform boundary (Gulick & Meltzer, 2002), or relative motion between the northwestern-translating Sierra Nevada-Central Valley microplate and the northern-translating Oregon Coast block (Unruh & Humphrey, 2017). Additionally, north-south compression from the northward migration of the triple junction has rotated the southernmost portion of the forearc relative to the rest of the margin, creating an actively faulting transpressional regime at the very southern end of our study area (Gulick & Meltzer, 2002).

5. Conclusions

Using four years of CI array data, we locate 271 earthquakes with epicenters between Cascadia's deformation front and the coastline. Little seismicity is observed south of the Nootka fault zone and north of the Washington/Oregon border (49°N-46°N). Off the coast of northern and central Oregon (46°N-43°N), abundant seismicity is observed between 45°N-46°N and near the previously identified earthquake swarms off Newport, OR (44.3°N-44.7°N). Offshore southern Oregon and Northern California, seismicity is abundant, including a very active swarm off the coast of southern Oregon at 42.2°N and 124.7°W. This distribution of microseismicity illustrates that current near-plate-interface activity within the CSZ is likely related to along-strike variations in subducting plate smoothness and hydration, which are controlled by plate deformation and the thickness of underthrust sediments. Further, abundant upper plate seismicity in the southern portion of the forearc is likely related to the complex stress field surrounding the

Mendocino triple junction. On the incoming plates west of the trench, intraplate seismicity increases significantly south of 46°N. These observations agree with recent active source seismic reflection/refraction studies on the JdF that show more extensive deformation of the subducting plate as the influence of subduction-bending and north-south compression from the Mendocino triple junction increases. While the data from the CI have been invaluable for characterizing present-day seismicity in the CSZ, further robust observations with both temporary and permanent OBS facilities in the subduction zone would likely resolve uncertainties around the origin and distribution of microseismicity, as well as its significance in the larger CSZ seismic cycle.

6. Figures

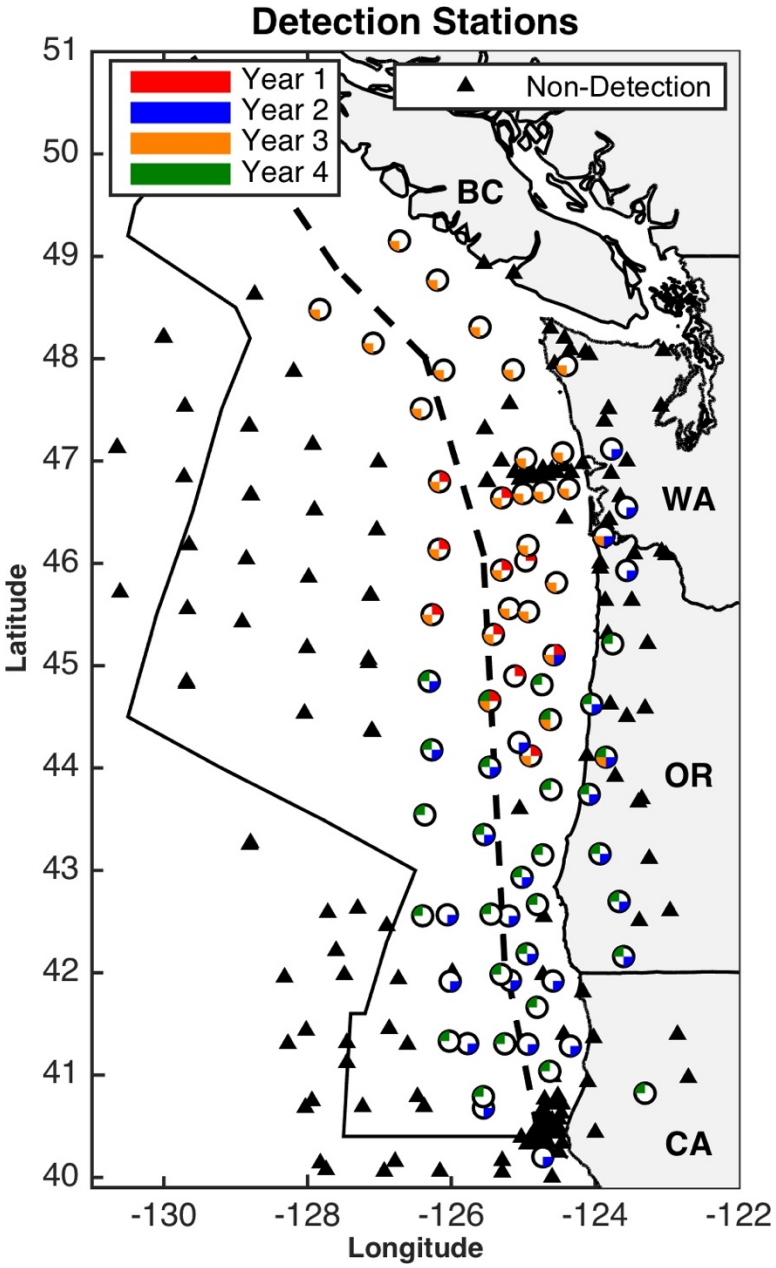

Figure 2.1. Cascadia Initiative (CI) OBS locations (offshore) and regional land-based seismometers.
OBS and land stations used in earthquake detection are circles; colored quarters correspond to the year(s) the site was used for detection. Other CI OBS and land stations used in location but not detection are black triangles. The dashed line shows the location of the Cascadia deformation front, the western extent of the Cascadia subduction zone.

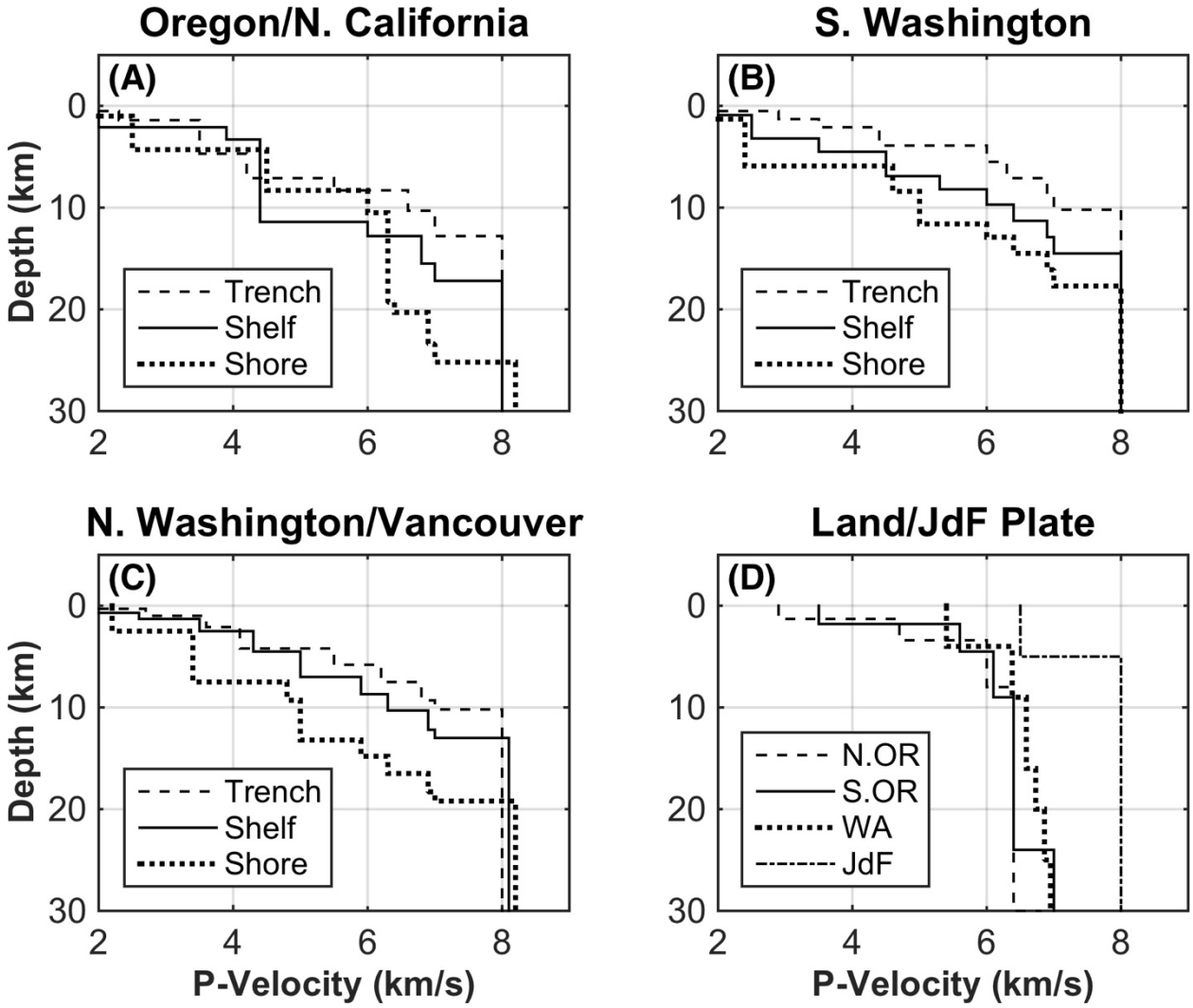

Figure 2.2. Velocity models used in Hypoinverse for event location.
Trench/Shelf/Shore velocity models were taken from active source seismic experiments (Flueh et al., 1998; Gerdom et al., 2000). The land/JdF plate velocity models (bottom right plot) are the same as those used by the PNSN in these regions.

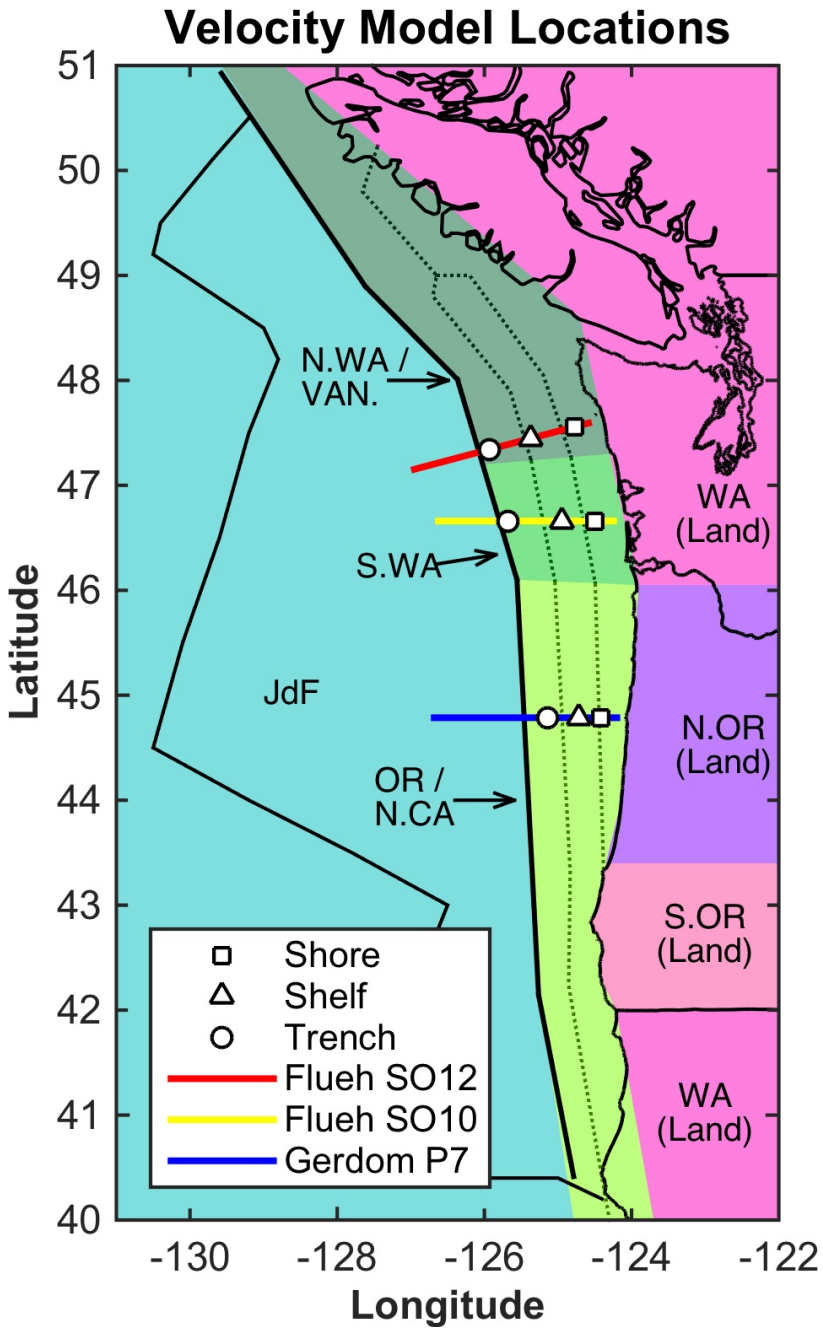

Figure 2.3. Mapped extent of Hypoinverse velocity models.
Approximate spatial extent of active source and PNSN velocity models used to locate events near and within the Cascadia subduction zone. White markers denote the location along the active-source lines where the 1D models were referenced. Dotted lines denote borders between respective shore, shelf, and trench models. In keeping with the PNSN's protocol, the same velocity model is employed for both landward western Washington and Northern California. Oregon and Northern California (OR/N.CA) correspond to profiles in Fig. 2.2a; southern Washington (S.WA) corresponds to Fig. 2.2b; Northern Washington and Vancouver (N.WA/VAN) correspond to Fig. 2.2c; and Land/JdF correspond to Fig. 2.2d.

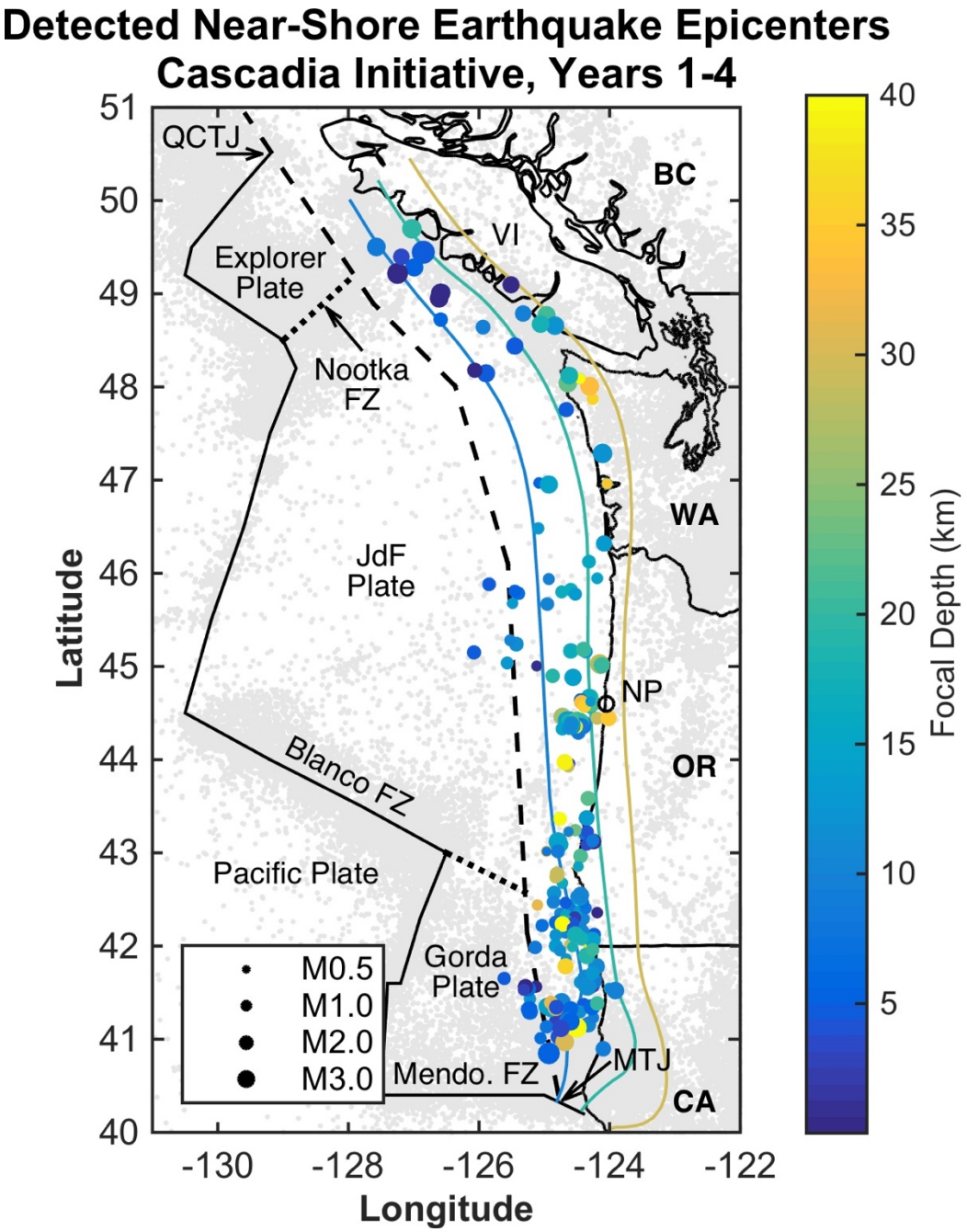

Figure 2.4. Locations of earthquakes detected in and adjacent to the Cascadia Subduction Zone
271 earthquakes were located with epicenters near the Cascadia Subduction Zone.
The locations shown were calculated in Hypoinverse. Epicenters are color-coded by depth; depth color scale saturates at 40km to allow comparison of events to plate contours. Contours show depth of the Juan de Fuca plate at 10, 20, and 30km (McCrory et al., 2012). Grey dots are historical epicenters recorded in land-based catalogs (PNSN, CNSN, NCSN), with the majority of historical event coming from the 1970-2015 time range. Also labeled on the map are the Queen Charlotte triple junction (QCTJ), the Mendocino triple junction (MTJ), Vancouver Island (VI), and Newport, Oregon (NP, hollow dot shows city location). FZ denotes fault/fracture zone.

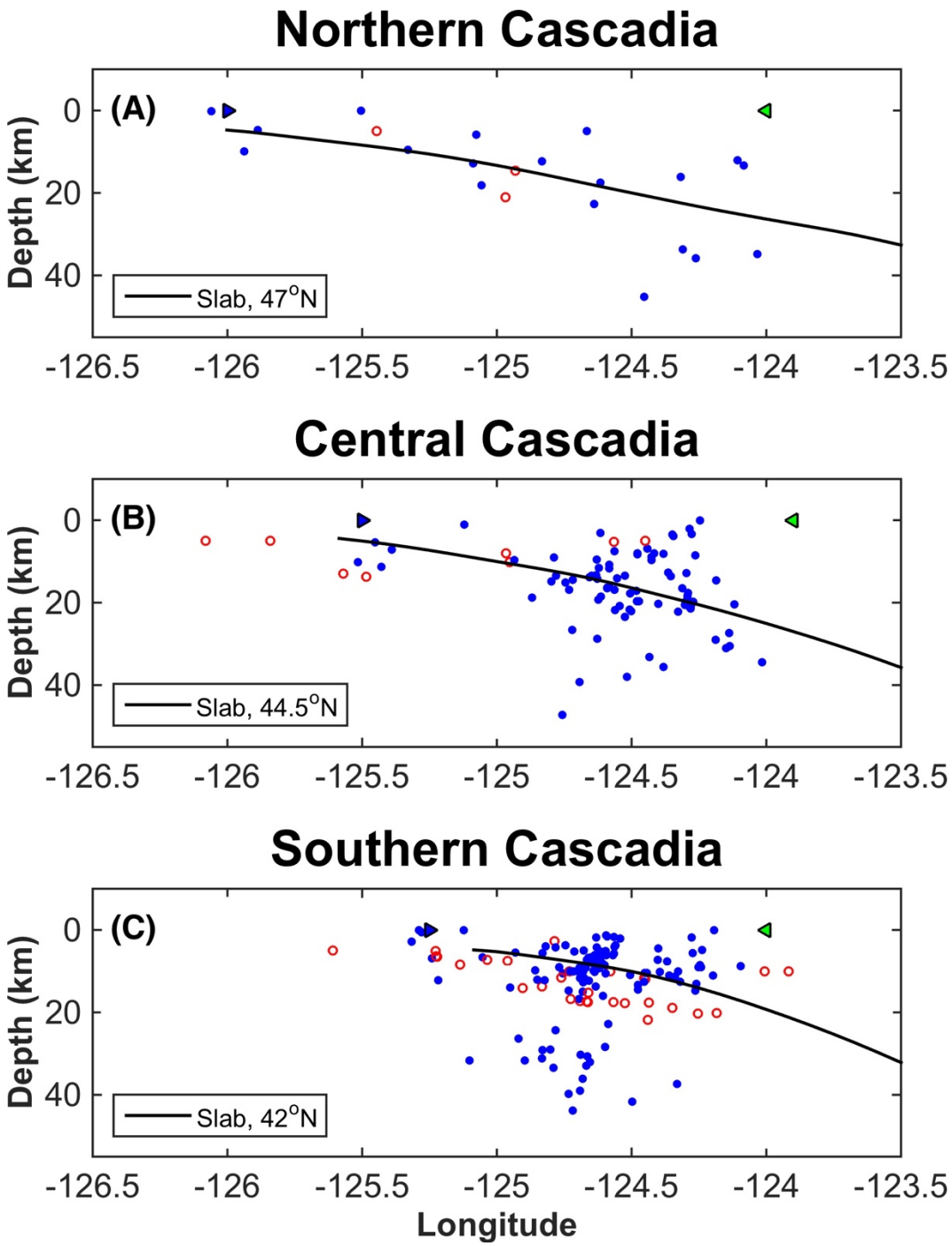

Figure 2.5. Depth distribution of detected earthquakes relative to the subducting slab. Depths of earthquakes in the north (**A**, north of 46°N), central (**B**, 43°-46°N), and south (**C**, south of 43°N) sections of the CSZ. Hollow markers denote events with standard error in depth greater than 10km, RMS greater than 1 second, or whose depths were fixed by Hypoinverse. Blue triangles denote the location of the deformation front, and the green triangles denote the location of the shoreline. Slab profiles are taken from McCrory et al. 2012. 11 events west of 126.5W (off northern Vancouver Island) are not shown.

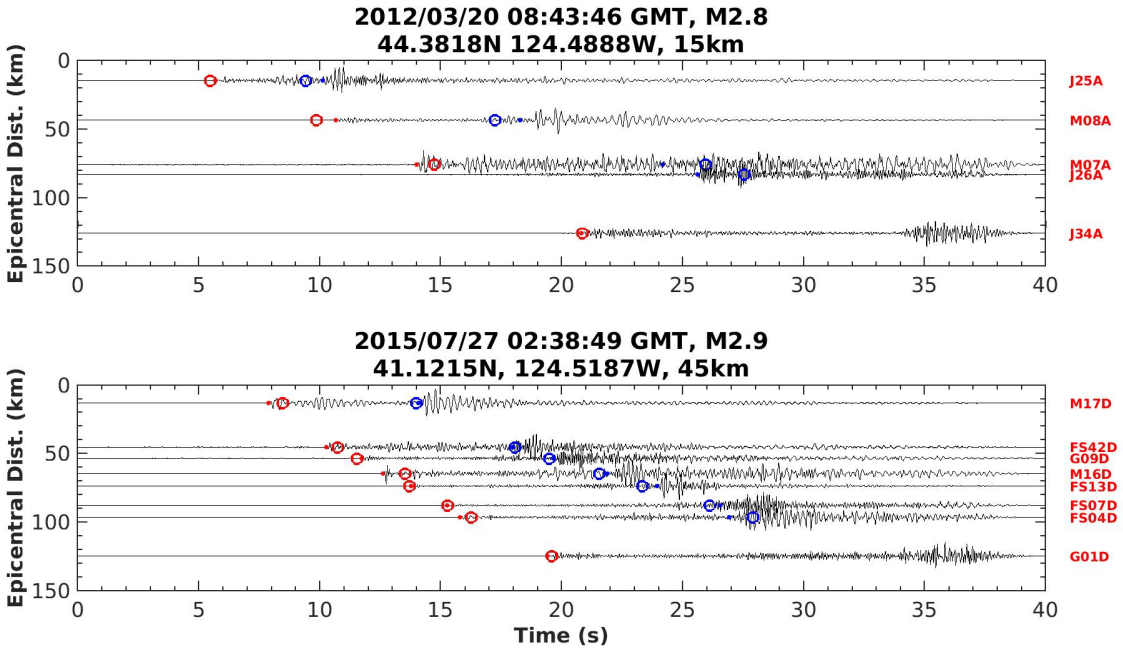

Figure 2.6. Example seismograms from 2 events detected in the CI data.
Traces shown are vertical channels, with associated CI stations listed to the right. X-axis starts at event origin time; red and blue dots show operator P- and S-phase "hand" picks, respectively; red and blue circles show P- and S-phase arrivals as predicted by Hypoinverse. Titles list event time, magnitude, latitude, longitude, and depth. Top: event detected during the first year of deployment off the coast of Newport, OR, corresponding to PNSN record 60403911. Bottom: event detected during the fourth year of deployment off the coast of Northern California, corresponding to NCSN record 72495196.

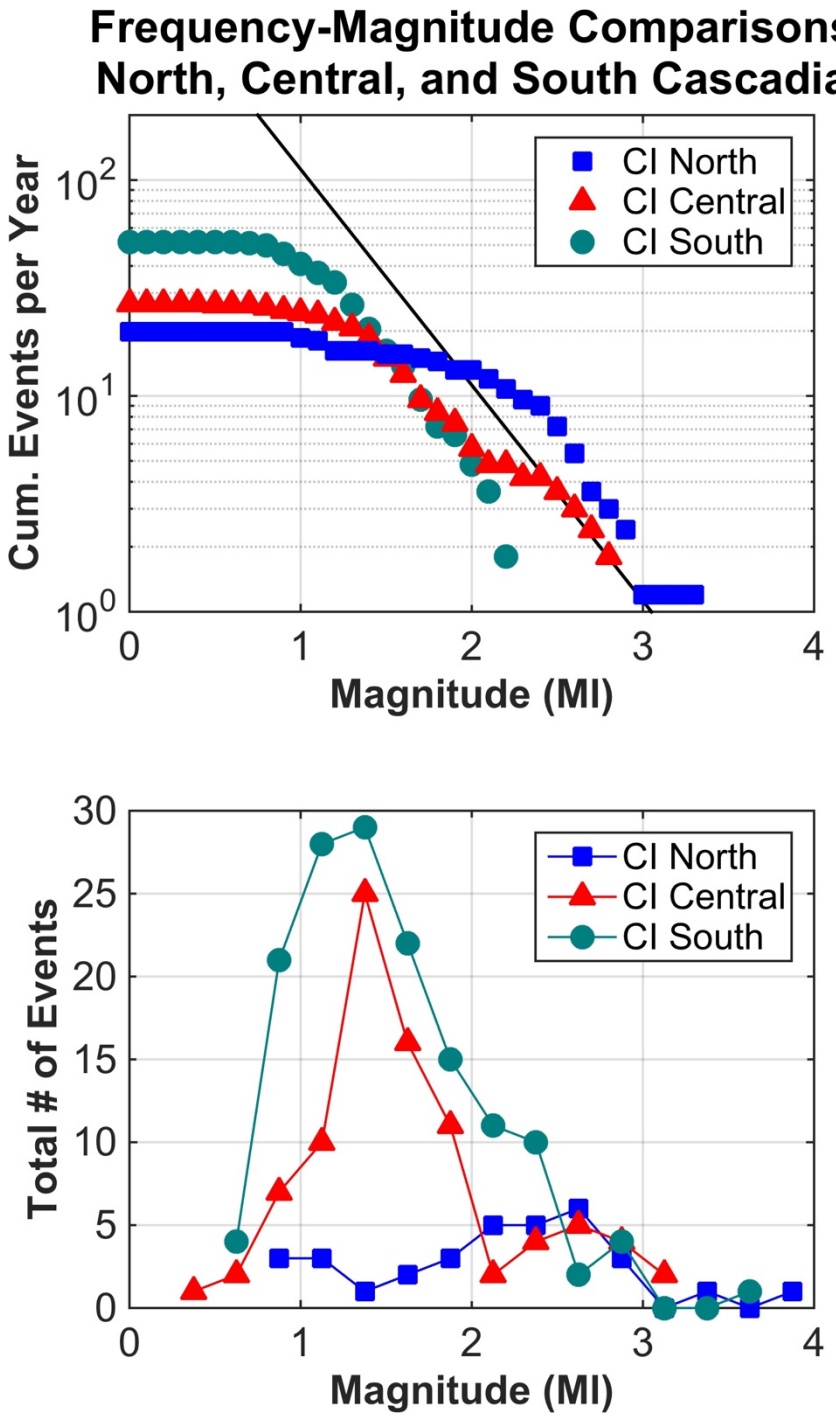

Figure 2.7. Frequency – Magnitude comparisons between the north, central, and south sections of the CSZ as recorded in the CI catalog.
Top: Cumulative events per year for each section. The black line has log-linear slope of 1.
Bottom: Overall number of events per magnitude per section (0.25 magnitude unit binning).

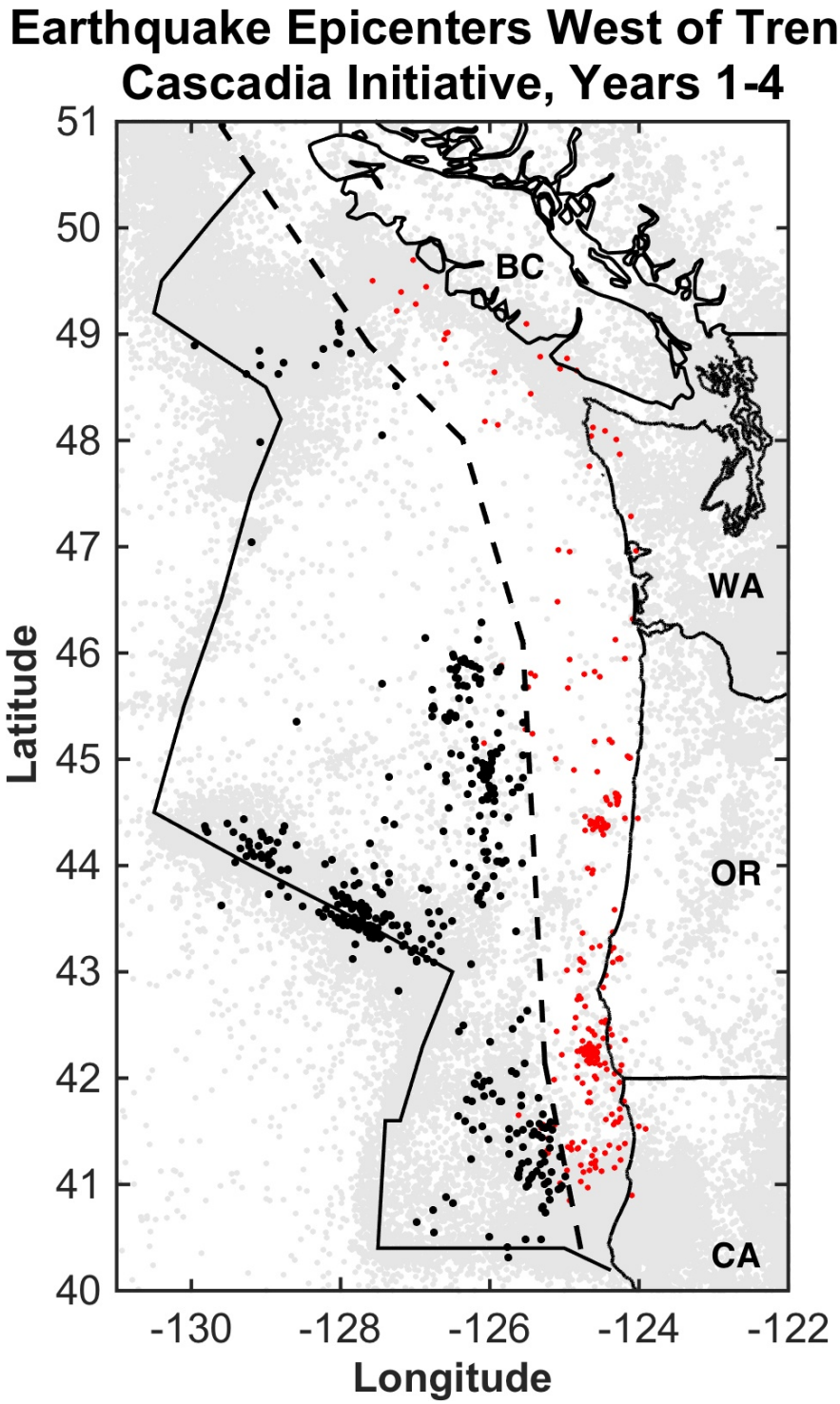

Figure 2.8. Earthquakes located on the Juan de Fuca plate.
440 Earthquakes detected to the west of the Cascadia deformation front (black dots) compared to the 271 detected near and adjacent to the megathrust (red dots) and historical land-catalog seismicity (same as in Fig. 2.4, grey dots). Events were located using a generalized IASP91 velocity model.

7. Tables

Table 2.1. Event detection parameters.
"STA/LTA" is the length in seconds of the short time and long time moving average windows; "Trigon/Trigoff" describe the ratio of STA/LTA needed to activate and then deactivate a trigger window; and "T_{min}" is the minimum trigger window duration.

Event Detection Parameters			
Deployment Year	**STA/LTA**	**Trigon/Trigoff**	**T_{min} (s)**
Year 1	1/8	3/2	10
Year 2	1/20	4/3	1
Year 3	2/25	4/3	1
Year 4	1/25	4/3	1

Table 2.2. Effects of underthrust sediment thickness and incoming plate deformation on near-plate-interface microseismicity in each of the regions along the Cascadia subduction zone.

	Underthrust Sediments	**Deformation of the Incoming JdF Plate**	**Resultant Degree of Hydration**	**Resultant Plate Interface Smoothness**	**Microseismicity Landward of the Deformation Front**
North Cascadia (north of 46°N)	Thin (≤600m)	Minimal bend-faulting deformation	Less hydrated	Smooth	Very low level of seismicity
Central Cascadia (43°N-46°N)	45°N - 46°N: Thin (≤500m)	Largely deformed with deep-cutting faults	More hydrated	45°N - 46°N: Rough	45°N - 46°N: Relatively high level of seismicity
	43°N - 45°N: Thick (1.4-1.7km)			43°N - 45°N: Localized asperities	43°N - 45°N: Earthquakes clustered around the inferred subducted seamounts
South Cascadia (south of 43°N)	Thin (250-600m)	Severely deformed with both bend-faulting and transform deformation	More hydrated	Rough	High level of seismicity

III. Simulated response of topography to ground motions from magnitude 7 earthquakes on the Seattle Fault

1. Introduction

Local site effects are one of the primary controls on the character of earthquake ground motions. Near surface geology, sedimentary basin structure, and topography all affect seismic wave propagation and can significantly increase the strength of earthquake shaking in certain scenarios. Among these, the contributions of topography are likely the least well understood. Though often coincidental, records of topographic effects on earthquake shaking do exist for a range of different topographic morphologies and earthquake magnitudes (e.g., Celebi, 1987; Davis and West 1973; Hartzell et al., 1994, 2014; Hough et al., 2010; Pedersen et al., 1994; Pischiutta et al., 2010; Spudich et al., 1996). In many of these cases, topographic effects were invoked to explain conspicuous, localized earthquake damage, typically occurring at the top of hills, ridges, and cliffs. Numerical simulations have helped augment the observational record (e.g., Bard, 1982; Boore, 1972; Bouchon et al., 1996; Sánchez-Sesma et al., 1982), providing a means to model the full wavefield response to topography, while analytic relations have allowed us to precisely constrain the factors governing some aspects of topographic response (e.g., Paolucci, 2002).

Together, these studies have demonstrated that topographic effects have a generally consistent set of characteristics:

- Topography has a much larger amplification effect on the horizontal components of ground motion than on the vertical components, which generally manifests as greater amplification in S- and surface-waves than in P-waves.

- Topographic highs (e.g., hilltops, ridges, and cliffs) tend to focus and trap seismic energy, resulting in an increase in ground shaking; conversely, topographic lows (e.g., the foot of hills and cliffs or valley bottoms) tend to diffract seismic waves, resulting in a decrease in shaking.
- The magnitude of amplification is both frequency and azimuthally dependent. Hills and ridges have the greatest amplification effect on waves with wavelengths approximately equal to their basal width (Boore, 1972). This amplification effect, often referred to as topographic resonance, reduces rapidly as the wavelength increases relative to the basal width; for shorter wavelengths, complex, alternating patterns of amplification and de-amplification may manifest along the slopes and near the base of the topography. If the topographic feature has a primary axis of elongation, amplification will be greatest for waves polarized perpendicular to this axis.
- A topographic feature's height will also influence the response, with amplification increasing with the ratio of height over basal width (Sánchez-Sesma, 1990).

Numerical simulations demonstrate that topography may also significantly scatter the seismic wavefield. Simulations of hills and ridges show that a portion of an amplified S-wave is converted to P- and Rayleigh waves, which emanate radially from the topographic feature (Bard, 1982; Bouchon et al., 1996). Similarly, Rayleigh waves interacting with cliff-like features experience increasing deflection when the ratio of cliff height over wavelength is greater than about 0.3 (Martel et al., 1977). Though there are some disagreements between experimentally observed and simulated amplification values, topography may more than double the strength of ground motion at its crest relative to its foot, with some observations noting amplification factors greater than 30 at certain frequencies (Geli et al., 1988).

Despite the influence topography may have on earthquake shaking, topographic effects are seldom considered in seismic hazard analyses, largely because of how difficult they are to accurately constrain. Because topographic effects depend on the azimuth of the incoming wavefield relative to the feature, their contributions to ground motions are highly dependent on the location of potential earthquake sources. Compounding this issue is that topography seldom assumes a simple, archetypal form. Many topographic features have complicated morphologies or are composed of a combination of features of varying scale, each of which has its own unique response. Shallow soil layers and geology, which influence topographic shape, respond in complex ways to ground motions as well. As a result, it may be difficult, if not impossible, to separate the unique contributions of topography to ground motion amplification (Geli et al., 1988).

In the context of ground motion simulation, scale presents a significant challenge to accurately modeling topographic amplification. Topographic features that can alter ground motions are often only tens-to-hundreds of meters in width and may only affect shaking at higher frequencies (>1Hz). Variability in this frequency range due to shallow velocity structure and source distribution is already high, complicating the prediction of topographic response. The computational requirements may also be prohibitively expensive to attempt direct simulations in these frequency ranges over large areas.

However, with the growing availability of high-performance computing, the development of codes capable of handling complex topographies, and more near-surface velocity data available at regional scales, it is becoming increasingly easier to directly model ground motion amplification due to topography. At present, few studies have attempted to simulate the effects of small-wavelength topographic features (<100 m) on ground motions at regional scales. Among

these, Lee et al., 2008, and Lee et al., 2009, simulated a M3.9 and a M5.0 earthquake, respectively, using point sources and meshes considering high-resolution topography in areas of Taiwan. Rodgers et al., 2010, simulated the effects of a nuclear explosion using an isotropic point source in a mountainous area of North Korea. Likewise, Imperatori & Mai, 2015, compared the contributions of topography and velocity structure to near-source scattering for a M5.0 earthquake in the Swiss Alps. Such simulations have been useful for constraining the fundamental ways in which topographic effects manifest in realistic earth models. However, extending these results to estimates of ground motion from higher magnitude earthquakes (>M5.5) is difficult, as slip can no longer be represented using a point source. The source dimensions for large magnitude earthquakes may extend into the hundreds of kilometers; the location of the hypocenter within that source area is largely impossible to predict, leading to ambiguity in how effects like directivity may manifest during a given earthquake. Further, slip on the fault surface is spatially heterogeneous, leading to a variable distribution of higher frequency shaking. Simulating the effects of these factors and the variability they introduce to estimated ground motions is a difficult task in and of itself, even without considering the contribution of topographic effects. However, attempts must be made to constrain the relationships between kinematic rupture parameters and topographic effects if topography is ever to be considered in seismic hazard analyses. In particular, as some seismic hazard characterization methods move towards incorporating direct ground motion simulation, it is critical to quantify the differences in the ground motions predicted by simulations with and without topography.

In this study, we explore the effects of topography on simulated ground shaking from large magnitude 7 (M7.0) earthquakes. Earthquakes are simulated using a kinematic source

model, providing a means to interrogate the sensitivity of topographic response to slip distribution and hypocenter location in finite fault rupture. A realistic, 3-D velocity model allows us to accurately represent wave propagation within our study region, while a model mesh with ~30 m surface spacing allows us to resolve ground shaking up to 3 Hz. Besides comparing the response between topography and non-topography simulations, we additionally compare the simulated peak ground motions with those predicted by the Ground Motion Models (GMMs) of the Pacific Earthquake Engineering Research Center (PEER) Next Generation Attenuation – West2 project (NGA-West2). By examining simulated ground motions from different locations on topographic features throughout the model region in both the time and frequency domain, we are able to broadly characterize simulated topographic response to finite fault rupture

2. Methods

SPECFEM3D Simulations and Model Mesh

For kinematic earthquake simulations we use SPECFEM3D, a spectral element method (SEM) code that adeptly handles complex topographic surfaces and performs well in large, parallel-computing applications (Komatitsch et al., 2004). SPECFEM3D discretizes the wavefield using a mesh of model elements, upon which a realistic velocity model and topographic surface may be imposed. A unique component of the SEM is the use Legendre polynomials as basis functions, as well as Gauss-Lobatto-Legendre (GLL) collocation points for interpolation within each element (Fichtner, 2011). A section of mesh used in this study is shown in Figure 3.1. To avoid oversampling at deeper depths with higher velocities, the element size was reduced closer to the surface. The average element size in our simulations was reduced from 300 m at depths greater than 1200 m, to 100 m from 300-1200 m depths, and ~30 m at depths less than 300 m. The ~30 m element size at the surface was selected to honor the dominant scale

of regional topography, since the majority of local features have base-to-crest heights of around 100 m and widths greater than 500 m. With 5 GLL points between each element vertex, average spacing of GLL points at the surface was ~7.5 m.

The region covered in our simulations encompasses the expected source area for a ~M7 Seattle Fault earthquake, as well as the city of Seattle and much of its metropolitan area (Figure 3.2). Topography in the Puget Sound region is largely characterized by glacial geomorphology, as the entire area was buried beneath the Puget lobe of the Cordilleran ice sheet during the last glacial maximum. The principal topographic feature in the model area, the ~250 m deep Puget Sound, is the largest of a series of north-south-trending channels excavated by ice and glacial outwash. Between these channels are drumlins reaching heights of up to ~150 m. Though fairly flat at their crests, the drumlins are flanked by steep slopes and cliffs that drop rapidly down into the channels. The regional topography is also strongly influenced by the Seattle Fault, a south-dipping reverse fault that bisects the model area along an east-west surface trace. Rigid sedimentary rocks and crystalline basement are brought to the surface just south of the fault, producing a line of geologically resistant hills; the tallest of these features is the 618 m tall Squak Mountain, which sits near the eastern edge of the model.

The topography used to develop the model mesh was primarily taken from a combined topography/bathymetry DEM for the Puget Sound, down-sampled to 30 m (Finlayson, 2005). Additional elevation data for the eastern portion of the model was taken from the U.S. Geological Survey 1/3rd arc-second DEM (USGS, 2017). To reduce mesh distortion and improve simulation stability, a smoothed version of the topography was used to define the refinement boundary at 300 m depth in the mesh. As is expanded upon in the discussion of the seismic

velocity model, at a few locations on the topographic free surface required smoothing to improve model stability. These locations are shown in Figure 3.3.

For each rupture scenario, a simulation was run on two different versions of the model mesh: one with topography and one without topography. (We will refer to these as "topography" and "flat" simulations throughout the text). Doing so allowed us to directly compare differences in the wavefield due to the topographic surface. Simulations were run on the Stampede2 supercomputer at the Texas Advanced Computing Center. A summary of simulation parameters is included in Table 3.1.

Seismic Velocity Model

The seismic velocity model employed in our simulations is the Cascadia Velocity Model (CVM) of Stephenson et al., 2017. This model reproduces the 3-D velocity structure of the region, explicitly incorporating the geometry of Quaternary and Tertiary basin sediments, as well as the Seattle Fault. Velocity values in the Puget Sound region are primarily from the active source P-wave tomography results of Ramachandran et al., 2006. For our simulations we augmented the velocity model with frequency-independent attenuation values, as well as a surficial (upper 50 m) low velocity layer, calculated following the methods outlined in Frankel et al., 2018. This surface layer varies velocity according to a randomized field with a standard deviation of 5% and with a characteristic length spanning several kilometers. Inclusion of such a layer improves ground motion estimates by mimicking the small-scale velocity variations that scatter surface waves and reduce focusing of seismic energy (Hartzell et al., 2010). Water was not included as a part of the velocity model. Earlier versions of this velocity model were found to accurately represent wave propagation from regional earthquake events (e.g., Frankel et al., 2009; Thompson et al., 2020), and have been employed in a variety of simulations (e.g., Allstadt

et al., 2013; Frankel et al., 2018; Wirth et al., 2018), as well as seismic hazard analyses (e.g., Frankel et al., 2007).

To accurately simulate wave propagation within topographic features, it is critical that the velocity structure respects the shape of the free surface. For both the topography and flat versions of the simulation, we up-sampled the upper 500 m of the velocity model from its initial XYZ spacing of 200X200X100 m to 100X100X50 m using a nearest-neighbors interpolation. The low velocity values at the surface were restricted to just the top layer of this updated model (i.e., the values were only applied in the uppermost 50 m). For the topography version of the velocity model, the velocity values at 100 m depth were stretched upward in areas with positive topography or were stretched downward in areas with negative topography. As such, the low velocity surface layer maintained a thickness of 50-100 m throughout the model. (A schematic illustrating this is shown in Figure 3.4).

Initial simulations using the topography version of the velocity model encountered some stability issues. Certain portions of the model region (generally, areas outside of the Seattle Basin) were underlain by rock assigned Vs > 1500 m/s at 100 m depth the CVM. These areas included the tall hills south of the Seattle Fault, as well as some of the more rugged topography near the east and west edges of the velocity model. Scattered elements in these regions were distorted such that their edge dimensions were somewhat smaller than the average ~30 m element size. Once these elements were assigned relatively high velocity values, the stability of the simulation degraded significantly. To restore stability to the simulations, topography was selectively smoothed by locally replacing the original topographic surface with one averaged over the surrounding points (~90 m in each direction). The influence of this smoothing was most significant in the direct vicinity of a problematic element (within ~100 m). This same smoothing

method was applied regionally to a 16.7 X 7.1 km portion of the surface in the upper northwest corner of the model area; the high near-surface velocity values and sharp topography widespread in this region made spot-smoothing ineffective.

In locations where smoothing did not improve model stability, we applied targeted velocity reduction. Velocity values directly adjacent to problematic elements were reduced by 30%, with a floor defined such that Vs was never set below 450 m/s. The areas affected by velocity and/or topography smoothing are shown in Figure 3.3. Overall, the smoothing did not impact a significant proportion of the surface and was largely near the edges of the model area, so we do not believe that it appreciably affected the results we present here. Nonetheless, we avoid these areas in the development of our discussion and conclusions.

Source Model

The source model used in this study was derived following the slip generator of Frankel et al., 2014. To ascribe slip to a fault surface, the method generates a random field of fractal distributions, for which the spectral amplitudes are flat up to a characteristic wavenumber (k), and decay as k^{-2} above that value. Correlation distances in the along-strike and down-dip directions, which define the inverse of the corner wavenumber in each dimension, were determined using the magnitude dependency relations of Mai & Beroza, 2002; a value of 7.9 km was used for the along-strike dimension, and a value of 5.9 km was used in the down-dip direction. We imposed the resulting slip distributions onto a 45°, south-dipping, planar representation of the Seattle Fault. This fault surface is in roughly the same position as the Seattle Fault's northernmost strand in Blakely et al., 2002, and is likewise aligned with the basement/basin velocity discontinuity in the CVM. Dimensions of the rupture zone were determined using the empirical scaling relationships of Somerville et al., 1999. For a M7.0

earthquake, along-strike and down-dip extents were set to 43.7 and 18.2 km, respectively. The upper edge of the fault was located at a depth of 3 km. The horizontal extent of the fault plane is shown in Figure 3.2.

The slip distribution was decomposed into individual sub-sources with a uniform spacing of 1 km. Rise time for each sub-source was determined by dividing the amount of slip by the slip velocity and then scaling by the S-wave velocity at the sub-source's location. The average slip velocity for all simulations was set to 1.0 m/s, a value consistent with the empirical relationships of Somerville et al., 1999, and which produces a constant dynamic stress drop; an additional random variation of +/-20% was applied to the slip velocity to reduce rupture coherence. A minimum rise time of 0.5 s was set for all sub-sources.

Rupture velocity across the fault surface was set to an average value of 80% of the local S-wave velocity. This value was scaled by the amount of slip at a given point, such that areas with greater than average slip had faster rupture velocities, and areas with lower than average slip had slower rupture velocities. An additional random variability (+/20%) was imposed on the value, though it was never allowed to exceed the local S-wave velocity. The subsequent rupture initiation times at each sub-source were randomly perturbed by a fraction of a second (<0.6 s) to mimic the small-scale variation expected in rupture during actual earthquakes.

Slip was prescribed to each sub-source using a moment tensor representative of reverse-faulting on the specified fault plane. Rake was randomly varied at each sub-source by +/-20%. The source-time function was represented using a Brune pulse (Brune, 1970). To avoid unrealistic jumps in slip at the edges of the fault, we applied a 3 km slip taper at each edge of the fault.

Variation of Rupture Parameters

To judge the sensitivity of topographic effects to variations in rupture parameters, we modeled nine different slip scenarios. These were defined using three different slip distributions and three hypocenter locations (east, central, and west). The slip distributions and hypocenter locations used in our simulations are shown in Figure 3.5. Each slip distribution was created by supplying a new random seed value to the slip generator. Henceforth, we will refer to individual slip distribution/hypocenter combinations according to the labels in Table 3.2.

Validation against a Real Earthquake Record

Before proceeding, we simulated a small local earthquake to ensure the accuracy of the model and method. The velocity model had previously been validated against the long period (>1 s) response from the 2001 M6.8 Nisqually earthquake (Frankel et al., 2009). Likewise, SPECFEM3D has been applied in earthquake simulation studies and reliably reproduces principal ground motion features (e.g., Magnoni et al., 2014). However, we wanted to ensure both the velocity model and method would perform well within the full range of modeled frequencies in the region of interest, particularly in the model applying the topographic surface.

We chose to model an M3.3 earthquake that occurred near the town of Bremerton, WA, at a depth of 24 km. This event was the largest well-recorded earthquake to occur within the model area in the last decade. The earthquake location and the location of recording stations are shown in Figure 3.6, along with a subset of recorded and simulated seismograms and the bias of the mean 5% damped spectral acceleration (SA). In this context, bias is computed as:

$$bias = \frac{1}{N}\sum_{n=1}^{N}(ln\, SA_{sim} - ln\, SA_{obs})$$

Eq. 3.1

Where N is the number of stations, and SA values represent the geometric average of the two horizontal components (Frankel, 2013). When calculating the bias, we exclude stations on artificial fill and thick, unconsolidated sediments. An acceptable bias value is defined as being less than +/-0.5 ln units, which corresponds to a factor of 1.7 relative to the recorded SA.

Body wave arrival times and peak ground velocities for the earthquake records were reasonably well reproduced in both the topography and non-topography simulations. The bias estimates are reasonable at shorter periods but begin to diverge at longer periods (>2 s); this misfit is likely due to the poor signal-to-noise ratio for longer period energy in this relatively small earthquake.

3. Results

We explore distinct aspects of the simulation results in the following four subsections. We start by comparing the topography and flat simulation results with the predictions of empirical ground motion models (GMMs); we then discuss the overall effects of topography on ground motions throughout the model region; we interrogate the response on individual, representative topographic features; and we end by exploring variability of response between the topography and flat simulations, with respect to location on the topography, and with respect to the kinematic fault rupture parameters.

Comparison with Empirical Ground Motion Models

In order to validate the simulated ground motions and provide an empirical point of reference, we compare the simulated results to the predictions from four of the Next Generation Attenuation West-2 (NGA-West2) Ground Motion Models (GMMs): Abrahamson et al., 2014; Boore et al., 2014; Campbell & Bozorgnia, 2014; Chiou & Youngs, 2014. Ground motions were evaluated for a grid of synthetic seismograms with a uniform, 2 km spacing across the entire

model region. For the GMMs, we designated a standard VS30 value of 600 m/s, which corresponds to the average CVM surface velocity within the model region; basin depth values were calculated using the 1000 m/s and 2500 m/s depth contour from the CVM.

Comparisons of the SA at four response periods (0.3, 1.0, 2.0, and 5.0 s) are shown in Figure 3.7. For each station in the uniform grid, we calculated the median rotated horizontal SA (rotD50) and then placed the results into 2km bins corresponding to distance from the fault surface (R). The mean SA curves represent the average SA within each bin for all nine earthquake simulations. Curves for the topography and flat versions of the simulation are separated into hanging-wall and foot-wall components. Also plotted are the within-bin +/-1σ ranges for the foot-wall component of the topography and flat simulation results. GMM values were estimated along a north-south line running perpendicular to the fault and roughly through the center of the model area. The GMM curve represents the average estimate of all four GMMs along that line, while the shading represents the average total standard deviation.

The topography and flat results tend to produce very similar mean values and standard deviations, with a few exceptions. Near-fault (<10 km) ground motions at 0.3 s are elevated in the topography simulations relative to the flat simulations. This is largely due to short-period resonance signals present in the response on some of the large hills along the periphery of the Seattle Basin and on either end of the Seattle Fault. These topographies are underlain by higher velocity (>1500 m/s) bedrock in the CVM. As a result, seismic waves reaching the surface in these areas were trapped within the ~50 m thick surficial low velocity layer, generating resonance patterns. The resulting short-period ground motions in the topography simulations in these areas are often more than twice that in the flat simulations. Similar high frequency resonance patterns in soft soils overlying high velocity bedrock have been observed in the region

during large earthquakes (e.g., Seward Park, as noted in Frankel et al., 2002). However, the regional thickness of these soil layers is not well constrained, so it is difficult to say whether the distribution and degree of soil resonance effects within the topography simulations are realistic. (As a point of comparison, look at the seismogram of station GMW in Figure 3.6B; GMW is sited on high velocity bedrock, and its simulated ground motions are significantly stronger than its observed ground motions.). We avoid these locations when exploring localized high frequency topographic response later in our analysis. Further from the fault, the topography is generally underlain by lower velocity basin materials, so the short-period response of the two models converges. Also apparent is a distinct difference in hanging-wall and foot-wall response with distance. At near-fault distances, ground motions on the hanging-wall is largely similar or slightly higher than on the foot-wall. However, at longer periods (≥1.0 s), ground motions remain high on the foot-wall out to large distances, while hanging-wall ground motions reduce towards the GMM predictions. This behavior is a result of basin effects within the Seattle Basin, which has been observed to significantly amplify long-period ground motions during local earthquakes (Frankel et al., 2002, 2009). Other studies modeling earthquake ground motions in the basin have found that simulated long-period results tend to produce much higher values than those estimated by GMMs (Allstadt et al., 2013; Wirth, Chang, et al., 2018).

In aggregate, both topography and flat results tend to estimate higher ground motions than the GMMs for all periods. The GMM standard deviations are large (ranging from around twice as large as the simulation variability at low periods to about the same size at longer periods) and encompass much of the mean simulated ground motions. However, there are some period and distance combinations wherein the simulated ground motions go well beyond the

GMM estimates. To directly quantify how much the simulated ground motions deviate from the GMM estimates, we calculate the epsilon value (ε):

$$\varepsilon = \frac{\mu_{Sim} - \mu_{GMM}}{\sigma_{GMM}}$$

Eq. 3.2

Where μ_{Sim} is the logarithmic mean SA for the simulated results, μ_{GMM} is the logarithmic mean of the GMM estimates, and σ_{GMM} is the logarithmic, mean standard deviation of the GMM estimates. For this calculation, we evaluated the GMMs at each point within the model region to match the format of the simulation results. We plot ε averaged for all stations versus off-fault distance in Figure 3.8, and ε mapped across the model region in Figure 3.9, for several different response periods. Short period (0.3 s) simulated ground motions are elevated with respect to the GMM estimates at near-fault distances, particularly in the topography model. Again, this is largely due to the effects of the near-surface low velocity layer, which overlies much higher velocity material near the ends of the fault, and which produces resonance signals in some simulations. Longer period ground motions tend to assume values in line with the GMM predictions at near-fault distances. However, beyond ~15 km, there is a distinct increase in the average ε value, particularly for periods ≥2.0 s. The distinct "bump" in the 2.0 and 5.0 s curves is partially caused by the lack of hanging-wall stations present at larger distances, which allows the foot-wall estimates to dominate the more-distant response. These foot-wall ground motions are heavily influenced by basin response at large distances and long-periods, which are much higher than the predicted GMM estimates. The GMM estimates may also struggle to account for the forward rupture directivity resulting from the deep hypocenter locations, which would preferentially project long period energy into the basin. Overall, the ground motions between the topography and flat simulations deviate from GMMs in similar ways. ε anomalies are in the

same general locations and are near the same values. However, it is clear that individual topographic features have some effect on the spatial distribution of ε. This is most apparent in the 5.0 s plot of Figure 3.9, where the a positive ε anomaly follows the ridgeline of a north-south trending peninsula near the center of the model region.

Overview of Topographic Effects on Simulated Ground Motions

To interrogate the overall effects of topography on simulation results throughout the model area, we directly compare the results between the topography and flat models. We compare snapshots of the vertical velocity field as measured at the surface during simulation S2E (Figure 3.10). At 5.4 s, shortly after seismic energy has reached the surface, there is little obvious difference in the flat and topography results. However, as time progresses and surface waves propagate northward from the fault, the wavefield is scattered by topographic features. This scattering manifests as a reduction in coherence of the surface wave front, as is apparent starting in the 11.9 s snapshot. By 25.8 s, the coherence of the main surface wave front has significantly degraded in the topography simulation relative to the flat simulation.

In Figure 3.11, we plot the percentage of Peak Ground Velocity (PGV) amplification in the topography model relative to the flat model (simulation S2E). This percentage is calculated by subtracting the vertical PGV at every point on the surface in the flat model from the PGV in the topography model, dividing the difference by the PGV in the flat model, and then multiplying by 100. PGV throughout the region is dominated by the S and surface wave components of the response, and thus should be sensitive to surface topography. Though there is significant spatial variability in amplification, some general trends are apparent. Topographic highs, like hill tops and cliffs, typically experience ground motion amplification, while topographic lows, like valley bottoms and channels, experience de-amplification. This trend

persists at a variety of scales, occurring both on smaller features (<500 m in width), as well as large features (several kilometers in width). These patterns may overlap with one another, resulting in a superposition of amplification patterns. As noted in the previous section, significant amplification manifests on the mountains on the east and west ends of the fault associated with high-frequency resonance in the low velocity surface layer. The dependence of peak ground motions on topography is reinforced by the bottom plot in Figure 3.11, which presents a cross-section of topography/flat horizontal PGV ratios extending from Bainbridge Island to the east bank of Lake Washington (profile A to A' in the upper plot). The PGV values used to generate this plot represent the average PGV at a period of 5 s between three simulations with different hypocenter locations (simulations S2W, S2C, and S2E). The amplitude of the PGV ratio roughly follows the trend of the large-scale topography; the most negative values are associated with the channels of the Puget Sound and Lake Washington, while the most positive values are associated with the isthmus of land between the two channels, as well as Bainbridge Island.

We quantify the generalized distribution of amplification in the topography simulation in Figure 3.12, where we plot the aggregate percentage of amplification versus period (A), as well as histograms showing the natural log of the PGV ratio at each period (B). To generate the plots in this figure, we used the PGVs from all nine simulations recorded on the uniform grid of stations, excluding stations situated in mountainous areas overlying bedrock (to avoid the combined effects of topography and soil resonance). For all periods of ground motion, a site in the topography simulation will on average record peak ground motions at or slightly above (≤5%) what would be predicted in the flat simulation (Figure 3.12A). However, larger amplifications and de-amplifications are common. For periods between 0.3 and 2.0 s, half of the

observations are amplified or de-amplified by more than 25-35%; 5% of sites see amplification greater than ~80%. For longer periods (5.0 and 7.5 s), the spread of amplifications is much smaller, with over 90% of sites seeing amplification less than 50%. The logarithm of the topography/flat PGV ratio indicates that amplifications due to topography assume a roughly lognormal distribution, the standard deviation of which is greater for periods ≤2 s (Figure 3.12B). Consequently, it is more common for ground motions to be amplified than de-amplified in the topography model.

Localized Effects of Topography

The influence of topography on ground shaking is highly dependent on a topographic feature's shape and orientation. To survey the effects of topography in our simulations, we placed synthetic seismogram arrays on fourteen topographic features throughout the model area, spanning a range of sizes, shapes, and orientations (Figure 3.13). While the results presented here reflect observations from all of these locations, we focus the bulk of our discussion on two representative features (Figure 3.14). The first is West Seattle, a north-south trending peninsula that tapers to a width of 400-600 m at its northern terminus, and which is bounded by 70-110 m tall cliffs. The second feature is Queen Anne, a 142 m tall, oblong drumlin with a width of ~2100 m perpendicular to its major east-south-east axis. West Seattle is representative of cliff response in the simulations, while Queen Anne is representative of hill response. Both of these features sit on the footwall within the Seattle Basin and should thus be free from the shallow soil effects seen at some locations outside of the basin.

Time Dependent Effects. Mapping the ratio of the root-mean-square horizontal PGV at the representative sites for simulation S2E demonstrates that ground shaking is typically amplified at the top of hills and cliffs and less- or de-amplified at topographic lows relative to the

flat model (Figure 3.15). We plot seismograms from the same simulation recorded at the top (WS12), on the slope (WS13), and at the bottom (WS14) of the cliff surrounding West Seattle in Figure 3.16. P-wave arrivals see little to no amplification in the topography results relative to the flat results, while S- and surface waves see significant amplification. Station WS12 at the top of the cliff experiences S- and surface wave amplification in all three components of its response, with a particularly strong amplification in its surface wave around 15 seconds, where the velocity in the northing direction is nearly doubled between the flat and topography simulations. By comparison, station WS14 at the foot of the cliff does experience some amplification, though less than either of the other stations. The effect of topography on the response at WS13 is more amplified than at WS14, but less amplified than at WS12. At all three stations, there is a small but systematic delay between the respective phase arrivals in the topography and flat simulations. We attribute this delay to the additional travel time between sea-level and the topographic surface.

Frequency Dependent Effects. Amplification due to topography is often linked to a characteristic frequency related to the physical dimensions of a topographic feature (Massa et al., 2014). At this "topographic resonance" frequency (f_r), ground motions at the top of a feature are significantly amplified relative to surrounding flat ground sites. To judge how much topographic resonance may contribute to the ground motion amplification observed in our simulations, we compare the response at different frequencies on West Seattle and Queen Anne.

Ashford & Sitar, 1997, used numerical simulations of S-waves interacting with cliffs to derive a relationship for the fundamental frequency of cliff-like features. Based on their observations, they found that ground motions are maximized when seismic waves have a frequency equal to Vs/5H, where Vs is the S-wave velocity and H is the height of the cliff. Near-

surface velocities in the vicinity of West Seattle are between 500-1000 m/s; cliff heights at the northern end of the peninsula are ~75 m tall. Therefore, we expect topographic resonance frequencies around 1.33-2.67 Hz.

Paolucci, 2002, derived an analytical relationship between the basal width of a triangular hill or mountain and the feature's resonance frequency. For features with an average S-wave velocity Vs and width L, the resonance frequency may be predicted using the equation $f_r = C*Vs/L$, where C is a constant around 0.7-1.0, depending on the height-to-width ratio of the hill and whether SV or SH waves are under investigation. For Queen Anne, near-surface velocities are also in the 500-1000 m/s range, and the basal width perpendicular to the principle axis is ~2.1 km. Using these values and Paolucci's relation for SH-waves, we calculate the fundamental frequency of Queen Anne to be around 0.18-0.36 Hz.

We decompose the ratio of the horizontal PGV on West Seattle and Queen Anne into different periods of ground motion (0.3, 0.5, 1.0, 2.0, 5.0, and 7.5 s, respectively) for simulation S2E in Figures 3.17 and 3.18. PGV values at each period were calculated by filtering the two horizontal velocity time series at each location on the surface at the period of interest (using a +/- 0.1 Hz buffer), calculating the root-mean-square of the two time series, and then finding the maximum value. With increasing period, the size of individual amplification and de-amplification patches increases, corresponding to the wavelengths of the waves most affected at that period. For the cliffs around West Seattle, we would expect the topography to affect ground motions most in the 0.3-1.0 s range. The greatest evidence for cliff-related amplification occurs in the 0.5 s (i.e., 2.0 Hz) plot (Figure 3.17B), where there is a semi-distinct band of amplification and de-amplification following the trend of the cliffs, particularly near the northwest end of the

peninsula. At the same time, there is little evidence for cliff-related amplification at 0.3 and 1.0 s (3.0 Hz and 1.0 Hz) (Figure 3.17A and 3.17C).

On Queen Anne, we would expect the hill to amplify ground motions most in the 2.0-5.0 s range. There is little evidence for systemic amplification due to topography for periods between 0.3 to 2.0 s (Figure 3.18A-D). However, distinct banding patterns are present at 1.0 and 2.0 s. We suggest these patterns reflect differences in the surface wave field between the topographic and flat simulations. Surface waves formed at the southern boundary of the Seattle Basin are scattered by topography as they propagate northward. The resulting changes in path affect the dispersion pattern of the waves and alter where they reach peak amplitude. Between 5.0 and 7.5 s (0.2 and 0.13 Hz) (Figure 3.18E and F), there is evidence for uphill PGV amplification Queen Anne, with the pattern being greatest near 5.0 s.

While useful for illustrating lateral patterns in amplification between the topography and flat simulations, the plots in Figure 3.17 and 3.18 do not directly quantify the strength of ground motion at the top of a feature relative to its bottom. When considering the mapped amplification patterns, it is difficult to separate the contribution of local topography from that associated with mid- and far-field scattering of the incoming wavefield. To isolate the amplification due to local topography, we use the targeted arrays of synthetic seismograms, taking the ratio of horizontal PGV between the top (and slope) seismograms over the PGV of the bottom seismogram. This calculation only considers the results of the topography simulation, so we can interrogate the effects of topography independent of the flat results. We plot the amplification at several different periods for simulation S2E at West Seattle in Figure 3.19. These plots show clear uphill amplification for periods between 0.3 to 1.0 s; there is little to no amplification at periods above 1.0 s. Note that the shorter period amplification pattern is not uniform for all locations (e.g., the

northeast set of stations at 0.5 s, Figure 3.19B). It is not uncommon to see mixed patterns of amplification at 0.3 and 0.5 s from one simulation to the next (we discuss this variability more in the next section); in contrast, the uphill amplification pattern at 1.0 s persists for all simulations. Based on these observations, we suggest that, within our model setup, the cliffs' topographic resonance lies somewhere between 1.0 and 2.0 Hz, and that there is consistent, predictable amplification near these frequencies. Longer periods of seismic wave are not affected by the cliffs, while shorter period waves experience complex scattering that varies the amplification pattern from one simulation to the next.

The stations on Queen Anne show little consistent amplification for periods between 0.3 and 2.0 s (Figure 3.20A-D). As on West Seattle, whether a station experiences amplification or de-amplification changes from one simulation to the next for these shorter periods. Uphill amplification only persists between 5.0 and 7.5 s.

Another characteristic behavior of topographic resonance is its azimuthal dependence. Amplification of ground shaking is typically greatest perpendicular to a topographic feature's primary axis of elongation. We explore how amplification changes with azimuth for simulation S2E in Figures 3.21 and 3.22. To develop these polarization plots, we rotate the horizontal components of the seismogram at five degree increments between 0 and 180 degrees, calculating the Fourier spectra at each increment. The spectra are smoothed using a Gaussian function to reduce variability in the response. We then take the ratio of the spectra at the top (and slope) of a feature over the spectra at the bottom of the feature. The resulting plots show the ratio of amplification at a range of frequencies and azimuths.

On West Seattle, there is a distinct dependence of the amplification patterns on the azimuth of the cliffs (Figure 3.21). The greatest amplifications (ratio values of ~3-4) are

generally at azimuths roughly perpendicular to the primary axis of elongation. However, there are typically multiple "peaks" in amplification along this azimuth, as opposed to a single strong peak at the expected resonance frequency. In reviewing the plots from other simulations, the highest amplification does often fall between 1.0-2.0 Hz, though there are occasionally larger peaks at higher frequencies. Some locations, like WS6 and WS7, will sometimes see their greatest amplifications at wholly different azimuths.

Queen Anne's non-uniform shape makes it difficult to define its primary axis of orientation; we assume a roughly east-south-east axis, corresponding to its longest basal dimension. The amplifications on Queen Anne are generally smaller (ratio values of ~2) and at lower frequencies than on West Seattle (Figure 3.22). Though, like West Seattle, the greatest amplifications often occur above the expected resonance frequency. The higher frequency amplifications (≥1 Hz) also tend to be quite variable from one simulation to the next, while the lower frequency amplifications are more persistent across simulations.

These results suggest that while topographic resonance contributes to ground shaking, there is a tendency for the response in any one scenario to stray from idealized behavior. It seems likely that modeled topographic amplification is also strongly influenced by other processes, like localized shape focusing, improvement of body wave incidence on the free surface, and scattering of incoming surface waves.

As the lack of clear azimuthal amplification on Queen Anne demonstrates, deviations from archetypal morphology will complicate topographic response. Throughout the model region, we observed that the more complex a topography's morphology, or the less distinct its shape, the harder it was to identify a distinct topographic response. Likewise, the more-gentle a feature's slope, the less significant its amplification between the topography and flat simulations.

A final critical observation is that comparing records between topography and flat simulations at a given location only provides a muddled picture of how the underlying topography affects ground motions. Adding topography to a simulation will produce an expected topographic response, but it will also affect the overall wavefield, and the response at any one site will reflect that. Figures 3.17 and 3.18, which only compared the topography response on each feature to the flat response, inherently mixed the effects of individual topographic features and mid-/far-field scattering, often obscuring the localized topographic resonance behavior. Therefore, the local response of topography is better quantified using our direct comparisons between the response at the top and bottom of a feature across several scenarios (Figures 3.19 and 3.20).

Variability of Topographic Effects

In this subsection, we examine the variability of simulated ground motions on account of topography from several different perspectives: the change in variability between the topography and flat simulations; changes in variability with respect to location on a topographic feature; and variability related to the kinematic rupture parameters.

Variability between Topography and Flat Simulations. To constrain the aggregate variability in response between the topography and flat simulations, we plot the percentage change in inter-event PGV standard deviation (σ, or STD) versus period in Figure 3.23. Similar to Figure 3.12, the percentage change in σ at a given site was calculated by subtracting the σ in the flat simulation from the σ in the topography simulation, dividing by the σ in the flat simulation, and then multiplying the result by 100. The σ values consider the horizontal PGV results from all nine simulations recorded on the uniform grid of stations, excluding stations situated in mountainous areas overlying bedrock.

Similar to the amplification behavior observed in Figure 3.12, the average change in σ is relatively low (<+/-5%); however, low and mid-range periods of ground motion (≤2.0 s) experience a larger distribution in σ change than longer period ground motions. The distribution of σ change is fairly uniform for these shorter periods, with around a quarter of sites assuming σ values 25-35% greater than in the flat simulation, and another quarter seeing values 30% lower. In contrast, at 7.5 s, over 90% of sites have σ within 30% of those predicted in the flat simulations.

We interrogate how these changes in inter-event σ relate to topography by looking at the targeted arrays on West Seattle and Queen Anne. On West Seattle, there is often significant variability from station to station at virtually all periods between the topography and flat simulations, though greater swings in σ are generally present at shorter periods (Figure 3.24). However, there is no obvious evidence for trends related to the cliffs (i.e., increasing/decreasing σ upslope). The same trends hold on Queen Anne (Figure 3.25) and persist throughout the model region as well. One notable exception to this trend is the longer period (≥5 s) σ at the regional scale. We plot the change in regional interevent σ at 5 s in Figure 3.26. Immediately apparent is the reduction in σ associated with channels, particularly the main channel of the Puget Sound. Regions of positive topography are associated with broadly increased σ.

Variability with Location on a Topographic Feature. We also explicitly compare the inter-event σ between the top and bottom of topographic features. In West Seattle, only 1.0 s ground motions demonstrate a uniform trend across the entire feature, with σ increasing upslope relative to the bottom at all locations (though the increase in σ is not necessarily uniform with

elevation or location) (Figure 3.27). Otherwise, the σ at lower periods (≤0.5 s) does not appear to uniformly follow a topography-related trend. Change in σ at higher periods (≥2.0 s) is negligible.

On Queen Anne, a trend of σ increasing upslope manifests at 5.0 and 7.5 s, with σ at the top of the hill typically being 35-40% greater than at the bottom (Figure 3.28). At lower periods, complex patterns of increased and decreased σ are present on the hill slopes.

Among all the targeted array sites, the variability in ground motions increases in a range that overlaps with the expected resonance frequency of the topographic feature. This behavior is more notable on features that also exhibited significant amplification near the topographic resonance frequency, as well as on larger-scale features (e.g., Queen Anne).

Sensitivity of Topographic Effects to Kinematic Fault Parameters. Ground motions in finite fault simulations exhibit a range of sensitivities to changes in kinematic fault parameters like hypocenter location and slip distribution (e.g., Moschetti et al., 2017; Wirth et al., 2017, 2018). Changing these parameters affects factors like the distance to high-slip subevents and ground motion directivity, which in turn affect the strength, predominant back-azimuth, and frequency content of the seismic energy recorded at a particular location. With respect to topographic amplification, it is well established that changing the location of a seismic source has significant effects on the severity of amplification (e.g., Imperatori & Mai, 2015; Rodgers et al., 2010). However, it is less clear how topographic effects may change when varying kinematic fault parameters; the location of the source is not changing, but the paths of the strongest seismic energy, as well as the frequency content and amplitude of shaking are. In this subsection, we explore how changing the hypocenter location and slip distribution affect simulated topographic effects.

In general, topographic amplification is highly variable from one earthquake scenario to the next. We plot polarization diagrams showing the spectral ratio between a top and bottom station in West Seattle for all nine simulations in Figure 3.29, along with an averaged polarization plot derived from all the simulations. The principal amplification patterns do roughly align perpendicular to the orientation of the cliff, and ground motions are consistently amplified in discrete frequency bands between 1 and 3 Hz, as is clear from the average polarization plot. However, for any one scenario, the amount of amplification, the exact frequency at which it peaks, and its orientation may vary significantly. For instance, the plots for S1W and S3W both share a common hypocenter location. However, the S1W plot reaches a peak amplification of ~5 near 1.9 Hz at 100°, whereas the S3W plot reaches a peak amplification of ~4 near 2.8 Hz at 70°. In comparing all the simulations, sharing a common hypocenter or slip distribution does not appear to result in strongly consistent amplification behavior; further, the topographic response does not appear to be more sensitive to one parameter over the other. It should be noted, though, that lower frequency response (<1 Hz) is more consistent across all simulations than higher frequency response.

While a topographic feature may assume a characteristic set of behaviors that roughly manifest from one earthquake to the next, significant differences in the wavefield result in differences in response. Specifically, the variations between individual polarization plots likely represent differences in the focusing and scattering of seismic energy within or adjacent to the topographic feature, since the polarization plots only measure variations in response between a feature's top and bottom. This is supported by the insensitivity of lower frequency ground motions to changes in slip parameters, because (as has been made clear in prior subsections) the lower frequency seismic waves are less likely to be affected by smaller-scale topography.

4. Discussion and Conclusions

In this study, we explored the effects of finite fault rupture on topography through direct simulation of earthquake ground motions. Our primary goal was to judge how adding topography may cause predicted ground motions to differ from those in typical flat finite fault simulations. We focused our analysis on near-fault (<40 km) ground motions from M7.0 earthquake scenarios on the Seattle Fault in Washington. Wave propagation was simulated using a spectral element method code (SPECFEM3D) and a model mesh considering a topographic surface with ~30 m spacing, allowing us to accurately model ground motions up to 3 Hz. We employed a 3-D earth model considering local fault discontinuities, basin geometry, and near-surface low velocity layers to ensure more realistic wave propagation. To address the sensitivity of topographic effects to finite fault rupture, we explored different combinations of kinematic rupture parameters, spanning three slip distributions and three hypocenter locations, for a total of nine different rupture scenarios.

Our primary means of interrogating the effects of topography was through comparing the results between simulations with and without topography, as well as between different elevations on topographic features. With respect to empirical GMMs, both the topography and flat simulations produced ground motions near or slightly higher than NGA West2 GMM predictions. Variability in both the topography and flat models was typically near or smaller than the total variability of the GMMs. The greatest deviations from GMM-predicted values occurred at short periods in mountainous areas where the low velocity surface layer overlaid high-velocity bedrock, and at long periods within the Seattle Basin, where basin effects and forward directivity strongly influenced both the topography and flat model results.

On average, ground motions (PGV) at a given site in the topography model were near that predicted by the flat model, though significant amplifications (>80%) were present at some sites, particularly at shorter periods of ground motion. PGV was typically amplified at the crest of hills and cliffs and de-amplified at topographic lows.

The components of the wavefield most affected by topography were the S- and surface waves, which saw amplification at the top of features relative to the bottom; P-waves saw little change in amplitude between the topography and flat simulations. Comparisons of PGV between crest and base stations at different periods demonstrated that amplification typically occurs near the analytically predicted topographic resonance frequency for cliffs and hills. Analysis to interrogate the directional dependence of results revealed that ground motions are typically most amplified perpendicular to a feature's primary axis of elongation. This effect diminishes on features with more amorphous shape and gentler slopes. Further, the exact direction (and frequency) at which maximum amplification occurs may vary somewhat from one earthquake scenario to the next.

Throughout the model region, the average inter-event standard deviation (σ) in the topography simulations was similar to that in the flat simulations. Though for shorter periods of ground motion ($\leq$2 s), around a quarter of sites saw an increase in σ greater than 25%, and another quarter saw a decrease greater than 30%. Changes in σ at longer periods were much less significant. In comparing the response at the top of a feature relative to its base, a systematic increase in σ was observed moving upslope, specifically at periods near the predicted topographic resonance frequency; topography-related trends were not directly apparent at other periods. The upslope increase in σ was typically most significant for larger-scale features. The reduced range of σ at longer periods relative to shorter periods mirrors the dependence of ground

motion variability on shallow velocity structure. Which is to say, longer periods of ground motion are less sensitive overall to topography than shorter periods of ground motion, much in the same way longer periods of ground motion show less sensitivity to small-scale velocity heterogeneities (Moschetti et al., 2017). However, this effect may be a factor of the topography present in this model region, and areas with a different topographic roughness (i.e., large mountains rather than mid-sized hills) might favor greater variability at long periods.

Results demonstrated a strong sensitivity with respect to slip distribution and hypocenter location. Amplification observations averaged across all simulations suggest topographic resonance does typically influence the results of a given simulation, chiefly through amplification near the resonance frequency at a predictable azimuth; however, significant variability between different rupture scenarios suggest other factors, like localized shape focusing, improvement of wave incidence on the free surface, and scattering of incoming waves, also play a significant role in the topographic response. We did not note a greater sensitivity of topographic response to one rupture parameter over another. In general, this sensitivity is greater for higher frequencies of ground motion (>1 Hz) than for lower frequencies.

The topographic effects in this study followed the same general patterns observed in studies of real-world ground motions, with some caveats. Topographic amplification during actual earthquakes has produced ground motions many times higher than in adjacent, flat-ground locations, as well as very strong directionality and adherence to a particular frequency range. In contrast, our results show a more muddled picture of topographic amplification, one in which topography certainly influences ground motions, but in ways that are generally subtle and only broadly predictable. Other studies have found that waveform simulations do tend to underestimate observed topographic effects, which has been attributed to simplifications in the

morphology and geology of the topography (e.g., Lovati et al., 2011). While some simplifications were necessarily made in our study to accommodate the scale of the overall simulation, we did attempt to respect both the morphology and shallow geology in our model.

Instead, we suggest the lack of significant response may be a factor of the topography within the model region. There is a gradation of response within our results which shows that features with steeper slopes do tend to have a higher amplitude topographic response, an observation that mirrors results from analytic solutions (Sánchez-Sesma, 1990; Sánchez-Sesma, 1985). However, with respect to much of the topography surveyed in the literature (e.g., Massa et al., 2014; Stolte et al., 2017), even the steepest features within our model area are relatively smooth; for instance, the cliffs around West Seattle, which produced some of the more distinct topographic effects in our simulations, have a maximum slope around 30°. When considered along with strong, near-field source variability and 3-D velocity structure, the individual topographic response of any one feature may be very complicated. Given that many high seismic hazard regions present similar complexities, we believe the results are reasonably representative of topographic response during finite fault rupture, particularly in non-mountainous areas. Given the degree of topographic amplification observed in this study, work should continue towards considering topography in seismic hazard studies, either through direct modeling of wave propagation or through some other novel metric.

As waveform simulations pursue ground motions at higher direct frequencies and over larger regions, we suggest a few improvements on the modeling method employed in this study. Introduction of more realistic near-surface soil structure would likely improve the accuracy of simulations. A significant challenge for future simulations will be accurately representing ground motions in areas where soils overlie high-velocity rock, which produced large resonance patterns

in our simulations. Emphasis should either be placed on high-resolution mapping of soil thicknesses in high-hazard regions, or on the development of a statistical method to realistically represent soil thicknesses within velocity models. Extending the model area to much larger regions (say, greater than 100 km X 100 km) would make it easier to explore the contributions of directivity to topographic response during very large earthquakes. The extent of the model area in this study made it difficult to comprehensively explore the contribution of directivity (which is often greatest in a relatively narrow azimuth range off either end of the fault), as well as topographic effects at more intermediate ranges. Additional simulations with a greater variety of slip distributions and hypocenter locations would provide a stronger basis for generalizing behavior on any particular feature within the model region. Further, it would be interesting to see similar finite fault tests run in regions with different geomorphologies. Other studies have found that the roughness of the topography in a model area has a significant control on scattering of the wavefield, which affects the spectral makeup of the wavefield at larger distances (Imperatori & Mai, 2015; Rodgers et al., 2010).

5. Figures

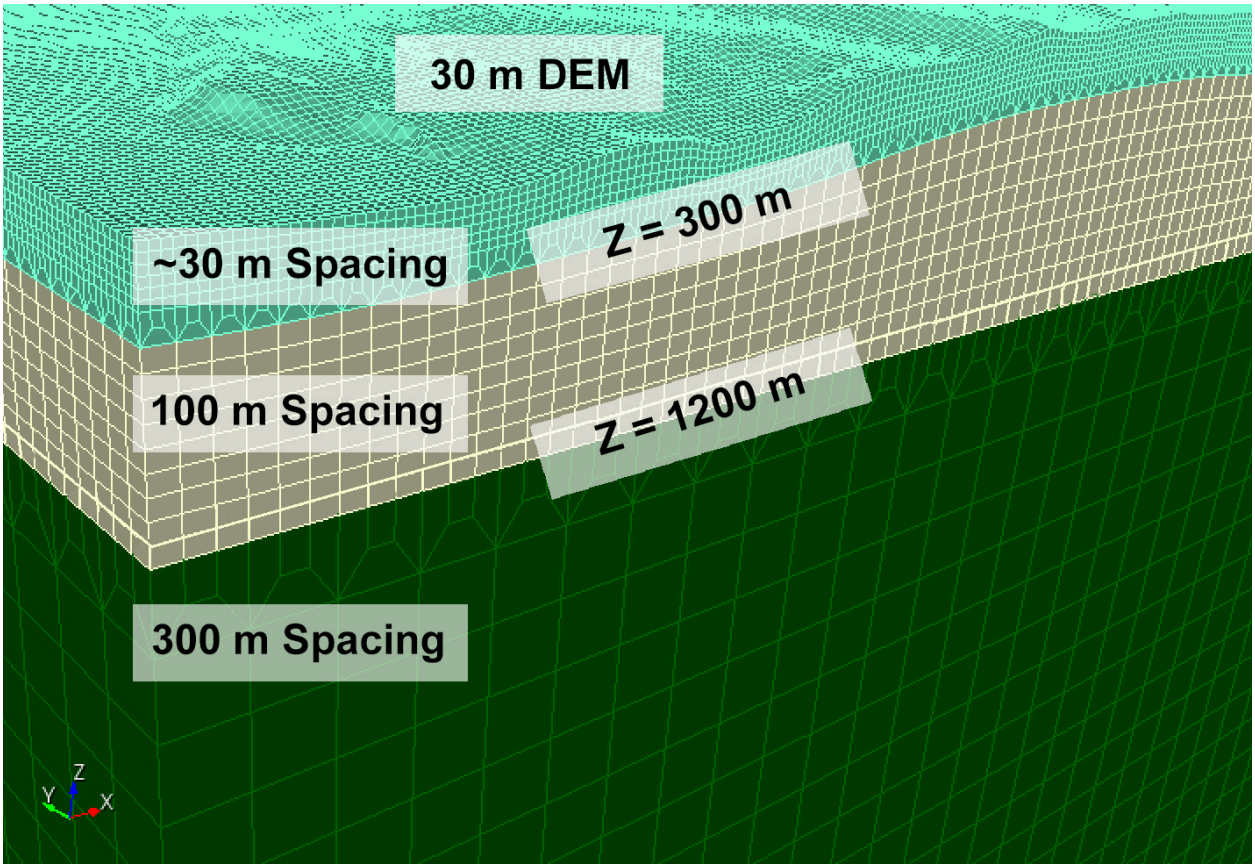

Figure 3.1. An example of the model mesh used in the spectral element method simulations. The top surface of the mesh is constrained with a 30 m topography DEM; the full extent of this topographic surface is shown in Figure 3.2. Spacing of the mesh increases from ~30 m near the surface to 300 m at depths below 1200 m.

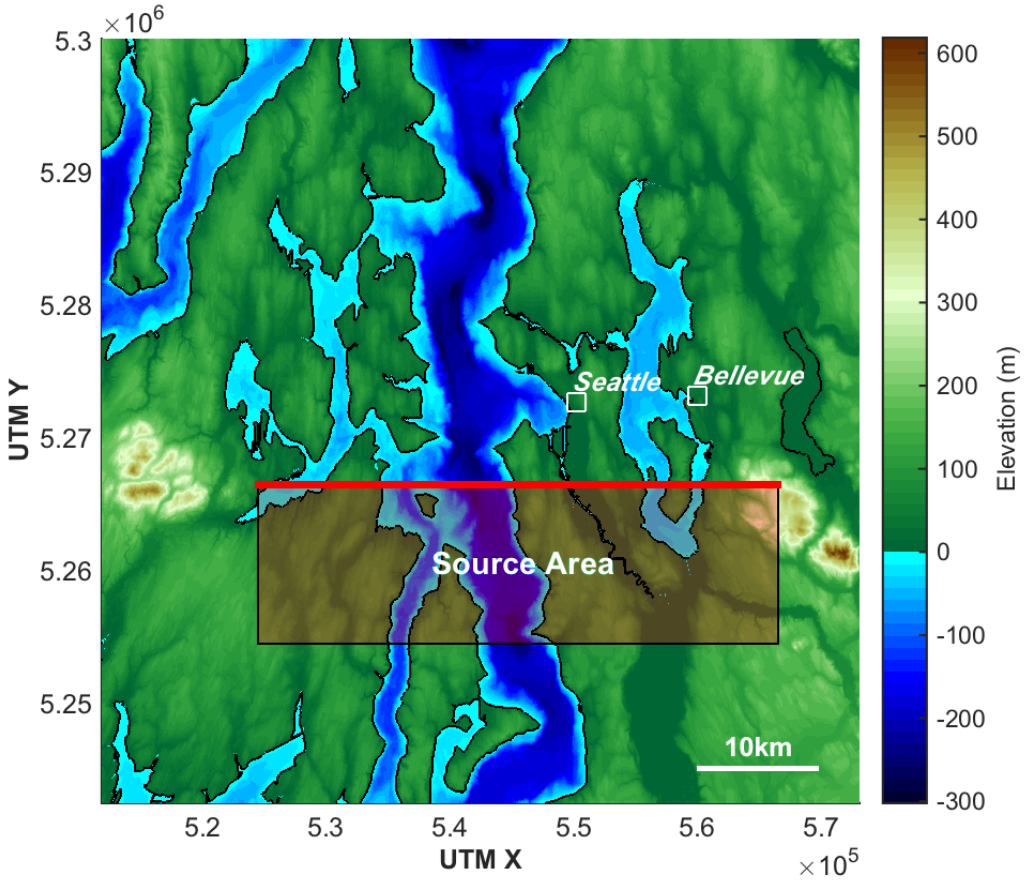

Figure 3.2. Map of model extent with 30 m sampled topography and bathymetry. Shaded area denotes the surface projection of the earthquake source, with the solid red line demarcating the up-dip edge of the rupture plane.

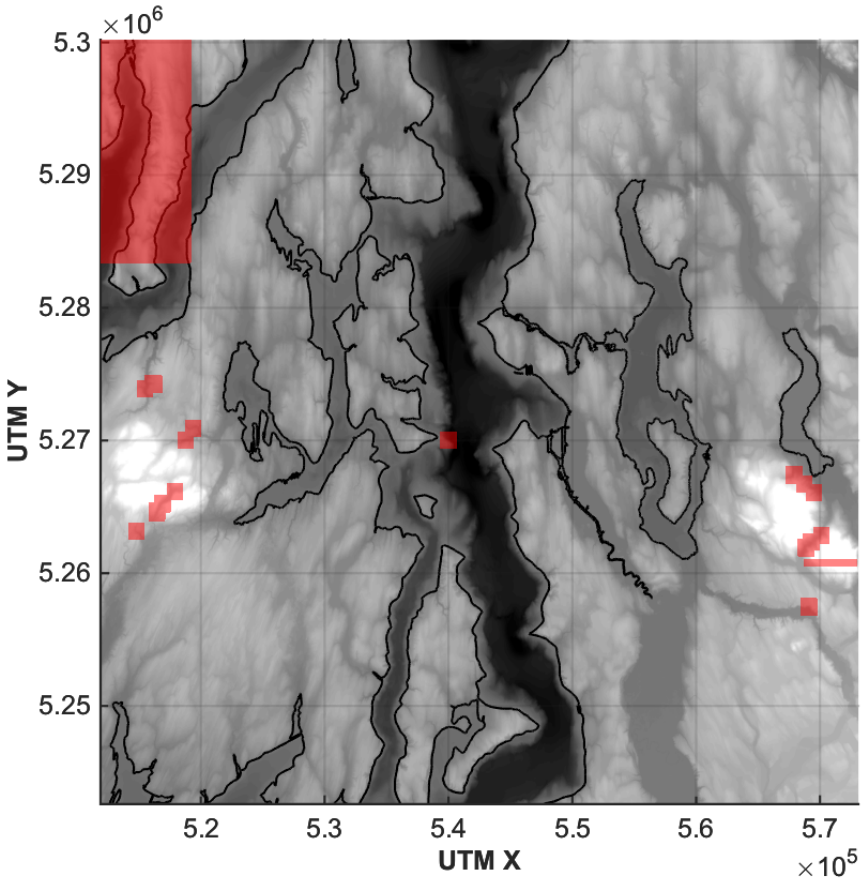

Figure 3.3. Localized smoothing was applied to the topographic surface in areas with red shading.

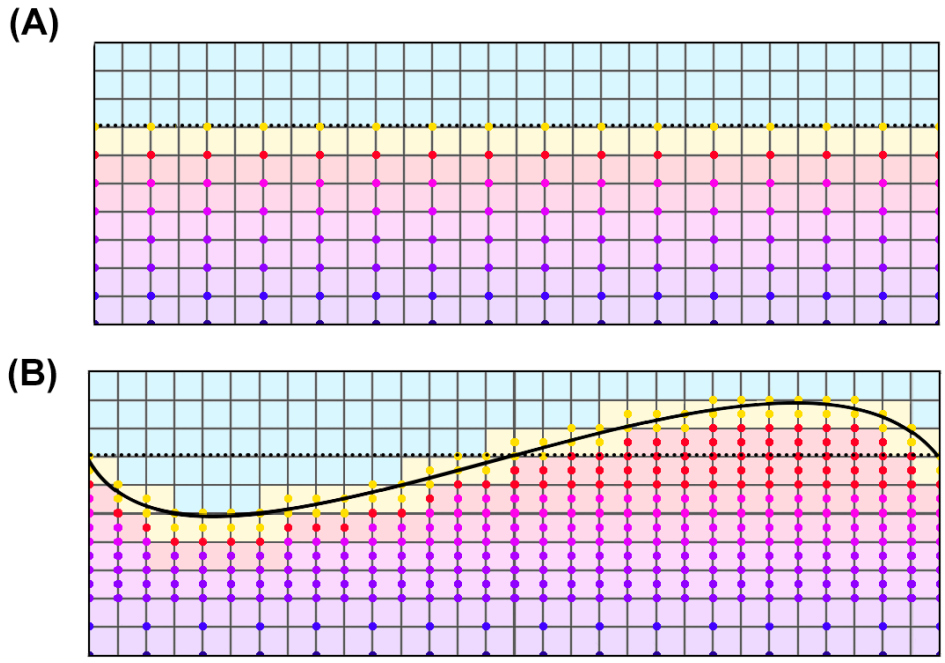

Figure 3.4. Illustration demonstrating how the velocity model was altered to accommodate topography.
The black base-grid has a uniform spacing of 100 m, while sea-level (0 m depth) is represented by a dotted black line. (A), the velocity model before adding topography. Velocity values (colored dots) were spaced every 200 m horizontally and 100 m vertically. The low velocity layer at 0 m depth is represented by yellow dots, while the velocity at 100 m depth is represented by red dots. No velocity values exist for depths above sea level. (B), the velocity model after adding the topographic surface (solid curved line). Spacing was decreased to 100 m horizontally and 50 m vertically. The velocity values at 100 m depth were either stretched upward to meet topographic highs or downward to accommodate topographic lows. The low velocity surface layer was kept at a near-uniform thickness of around 50 m across the model. The velocity model below 500 m depth was left unaltered.

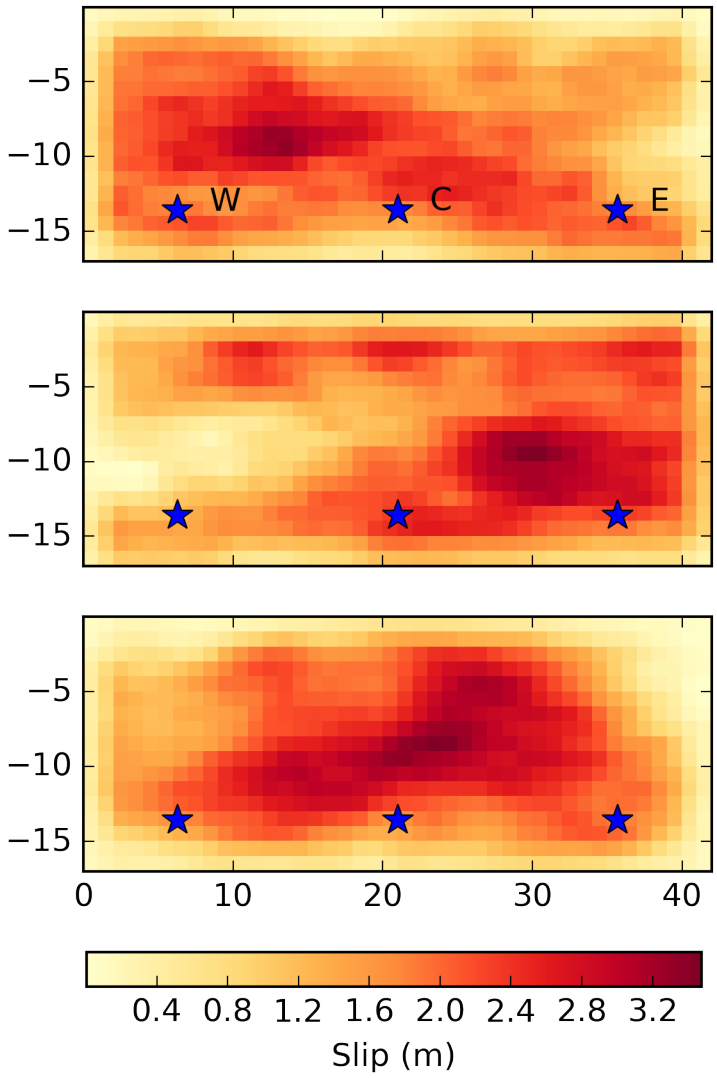

Figure 3.5. Slip fields used to define the three different source distributions.
Stars denote the three different hypocenter locations. With respect to the scenarios listed in Table 3.2, slip distributions 1, 2, and 3 correspond to the top, middle, and bottom plots, respectively.

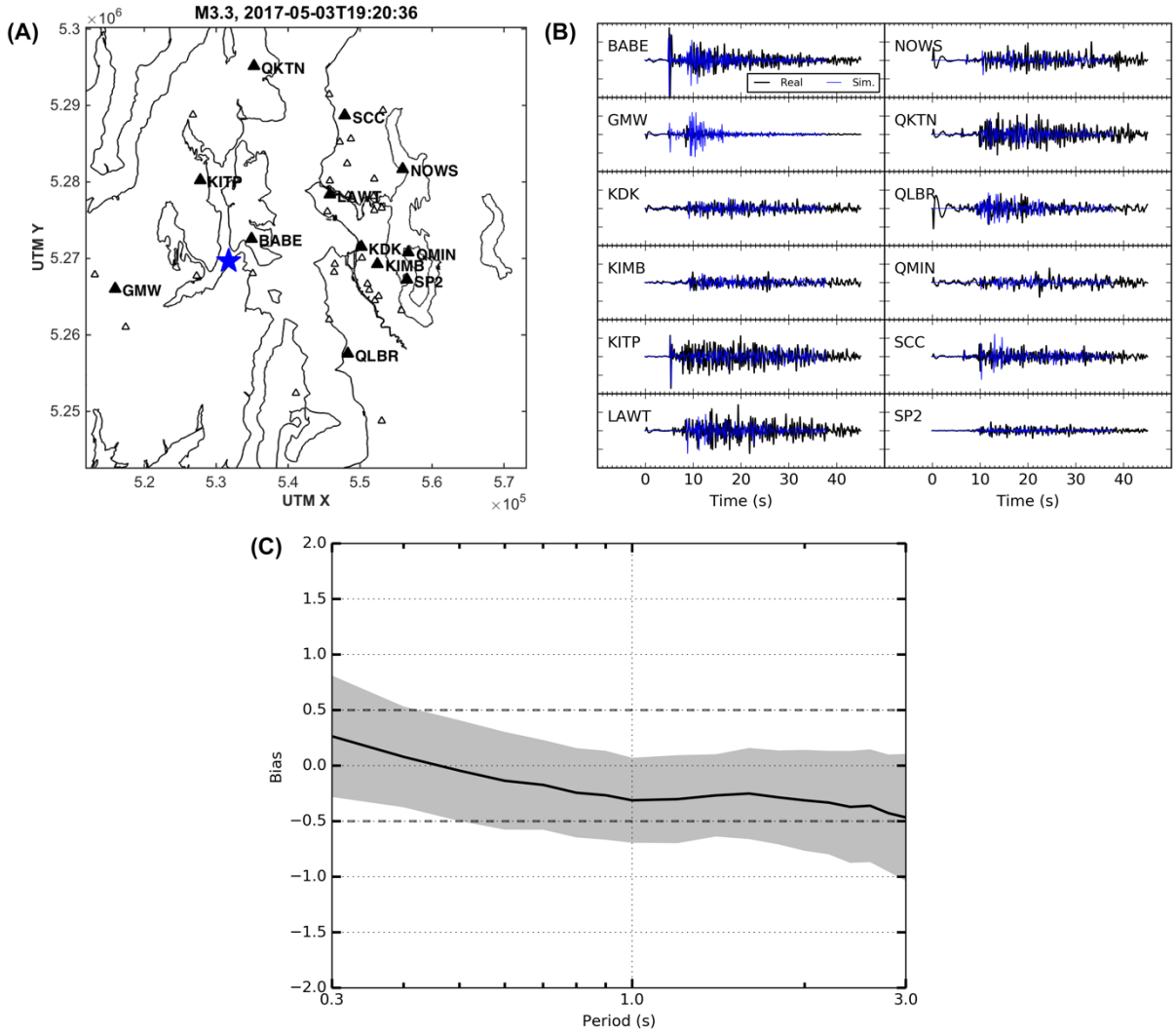

Figure 3.6. Location, timeseries, and bias results of a M3.3 simulated test earthquake. (A) Map showing location of the M3.3 test earthquake (star) and modeled stations (triangles). (B) A selection of seismograms showing the vertical component of the earthquake record (black), along with simulated seismograms from the topography model (blue). (C) Bias (solid black line) and standard deviation (shaded region) of spectral accelerations between the modeled and real earthquake data. Dashed grey lines represent +/-0.5 bias.

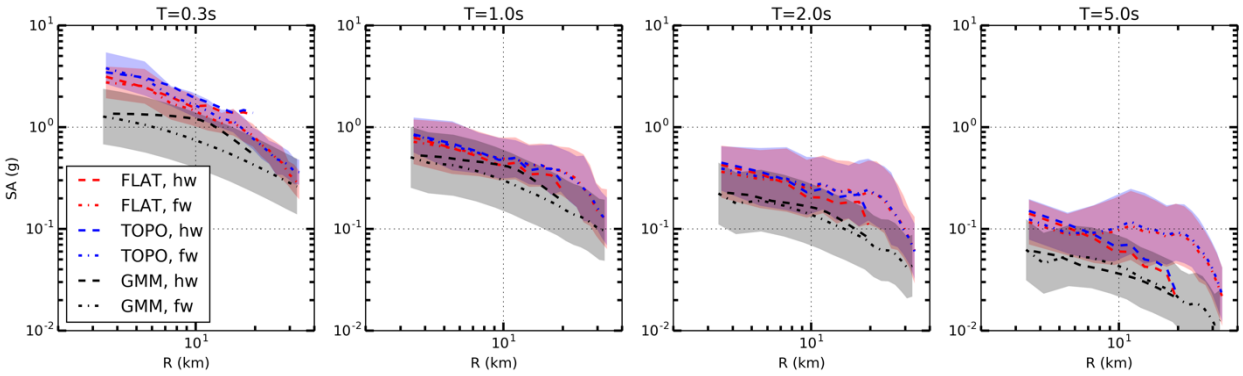

Figure 3.7. Spectral accelerations versus closest distance to rupture (R) at different periods of ground motion, separated into hanging wall (hw) and foot wall (fw) curves.
Black curves represent the average ground motion from four NGA West2 GMMs. Shaded areas represent the +/-σ range for the predicted and simulated ground motions (foot-wall only).

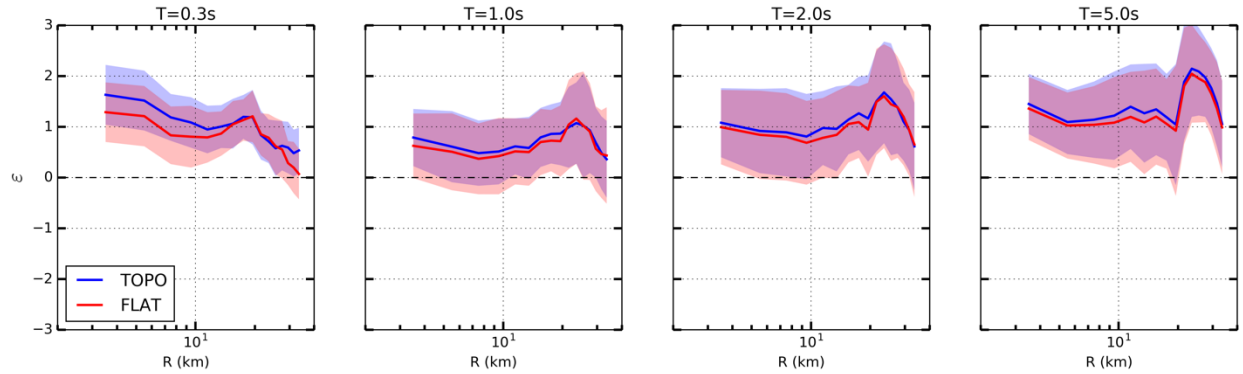

Figure 3.8. Epsilon (ε) values versus closest distance to rupture (R) at different periods of ground motion. Shaded areas represent the +/-σ range for the simulated ground motions.

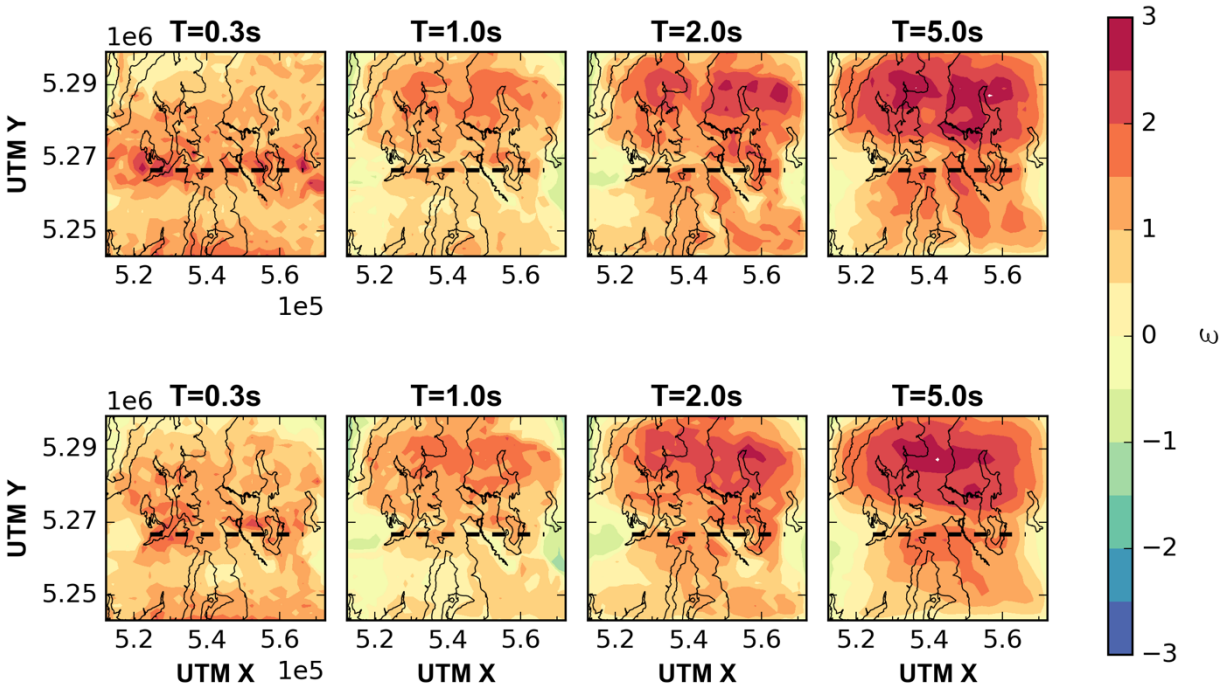

Figure 3.9. Epsilon (ε) values mapped across the model region at different periods of ground motion. Top row describes topography simulations, while bottom row describes flat simulations.

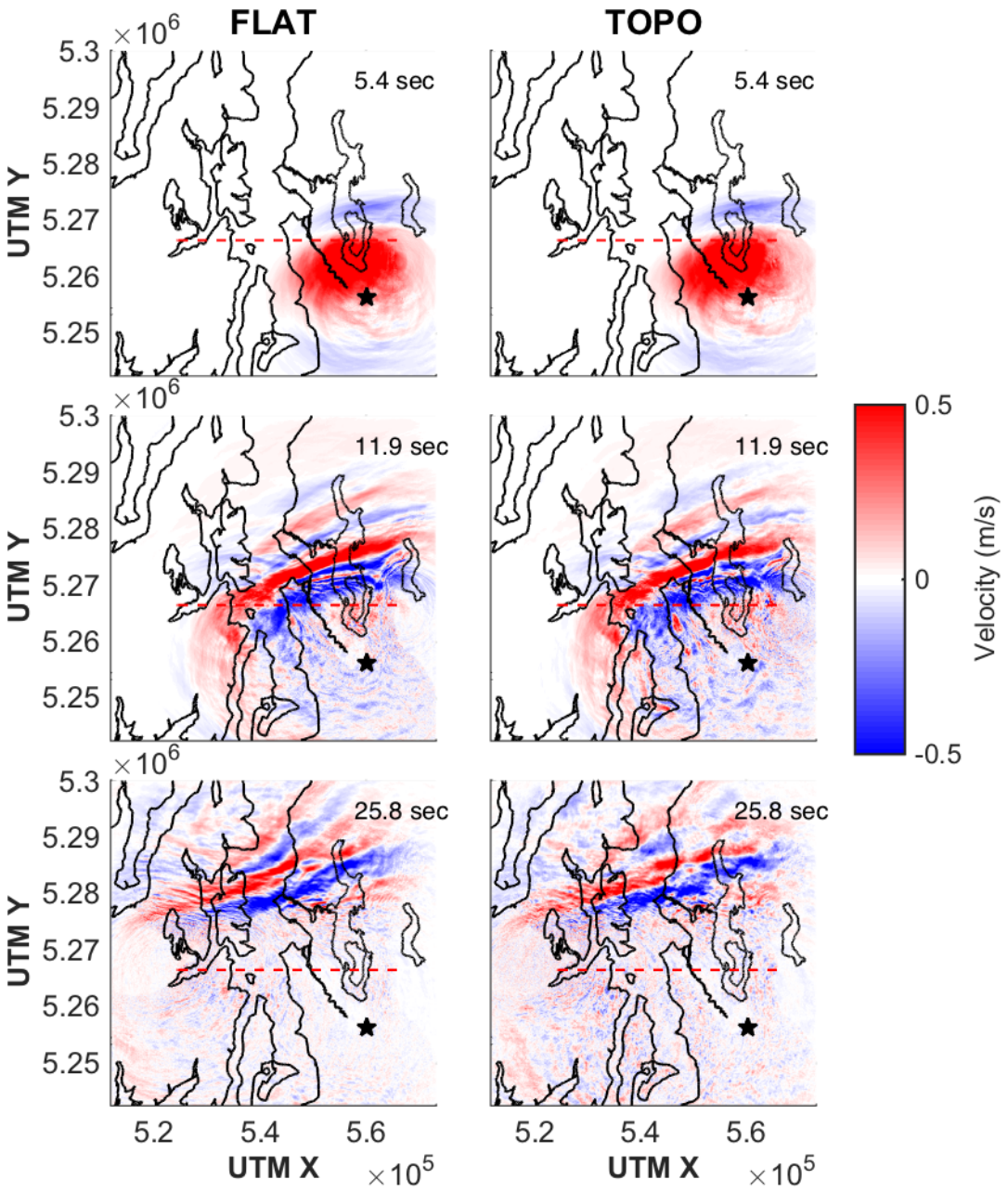

Figure 3.10. Snapshots of the vertical velocity wavefield at different times.
The flat simulation is in the left column, and the topography simulation is in the right column (Simulation S2E). Warm colors represent upward velocity, while cool colors represent downward velocity. The hypocenter location for this scenario is represented by a star.

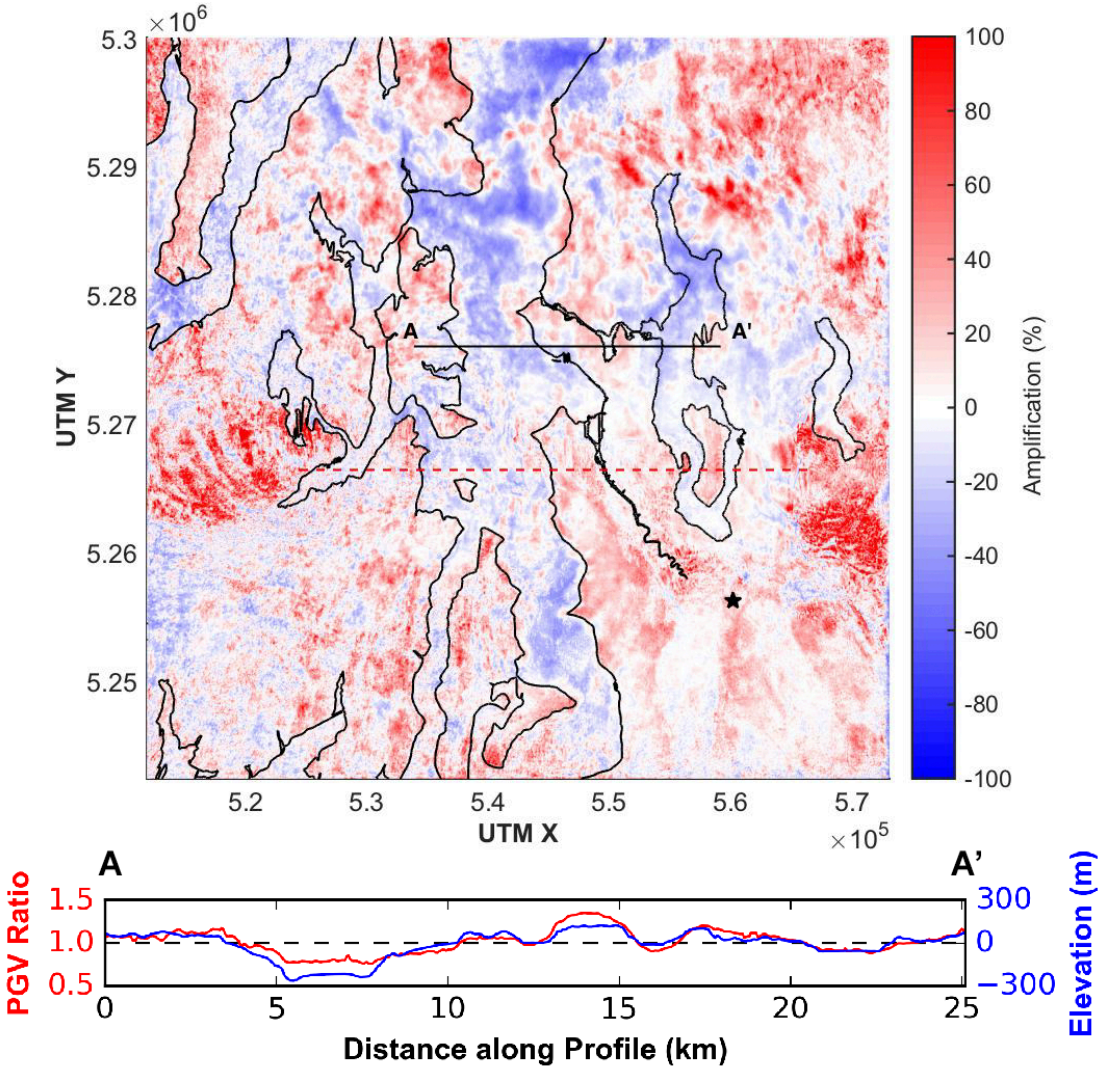

Figure 3.11. Amplification of the PGV in the topography simulation relative to the flat simulation (Simulation S2E).
(Top) Percentage amplification map over the full model extent. Amplification at a particular point on the map is calculated by subtracting the vertical PGV in the flat model from the PGV in the topography model, dividing by the PGV from the flat model, and then multiplying by 100 to get an amplification percentage. The hypocenter location for this scenario is represented by a star. (Bottom) Horizontal PGV ratio over the profile A-A' for ground motions at a period of 5 s. The ratio curve (red) represents the average ratio of the root-mean-square horizontal ground motions from three different simulations (simulations S2W, S2C, and S2E). Also plotted is the elevation along the profile (blue).

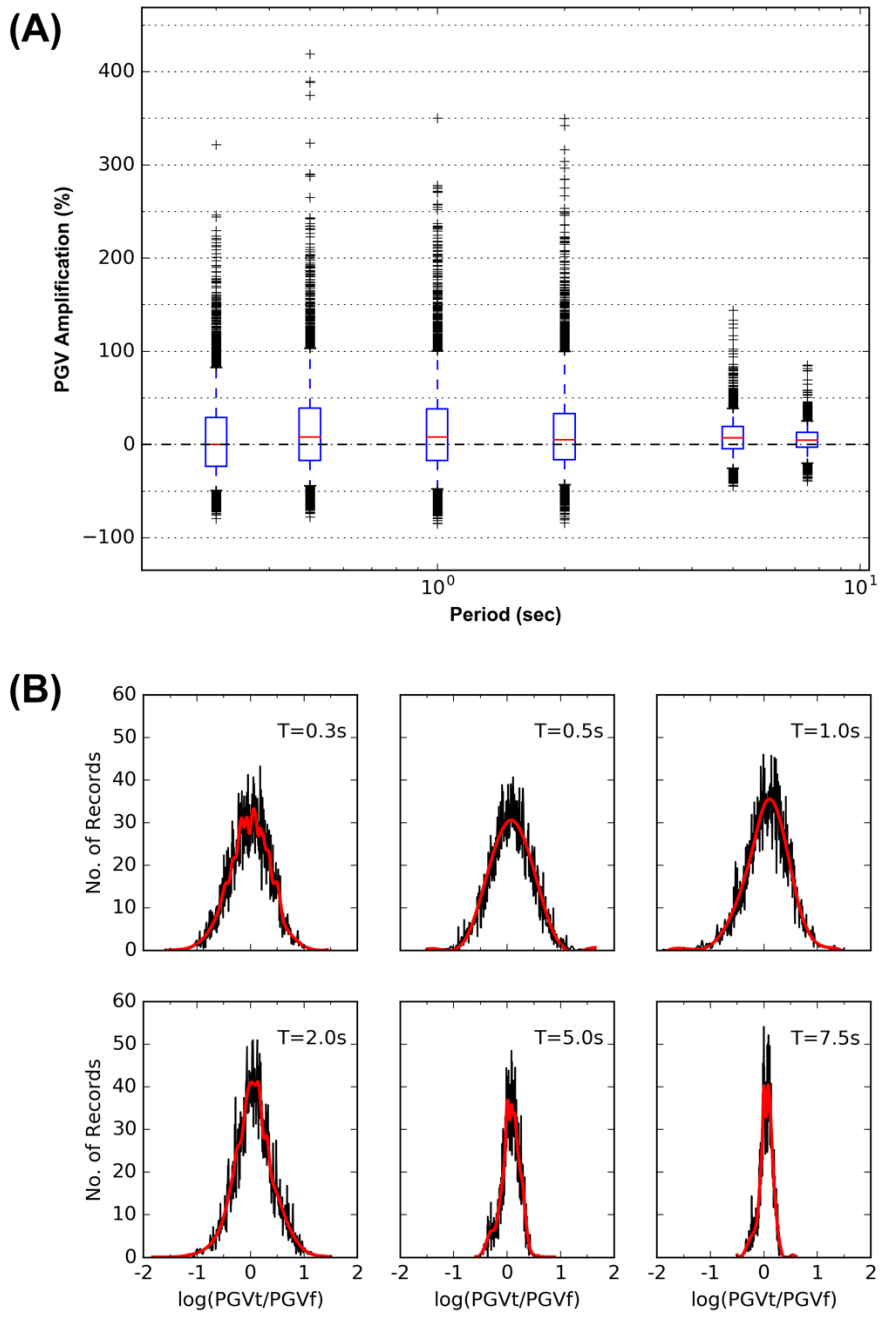

Figure 3.12. Distributions describing the amplification between the flat and topography simulations across stations in the uniform grid (excluding stations over bedrock).
(A) Percentage of amplification, where location along the x-axis represents the period of ground motion. Each box bounds 50% of observations, with the red line representing the mean value of the distribution. Whiskers bound 90% of observations. Positive values represent an amplification in ground motion in the topography simulation relative to the flat simulation, while negative values represent de-amplification. (B) Natural log of the topography/flat PGV ratio. Each plot shows a histogram of ratio values at each period. The black curve is the raw histogram, which is split into ~640 bins. The red curve is the histogram averaged across 10 bins.

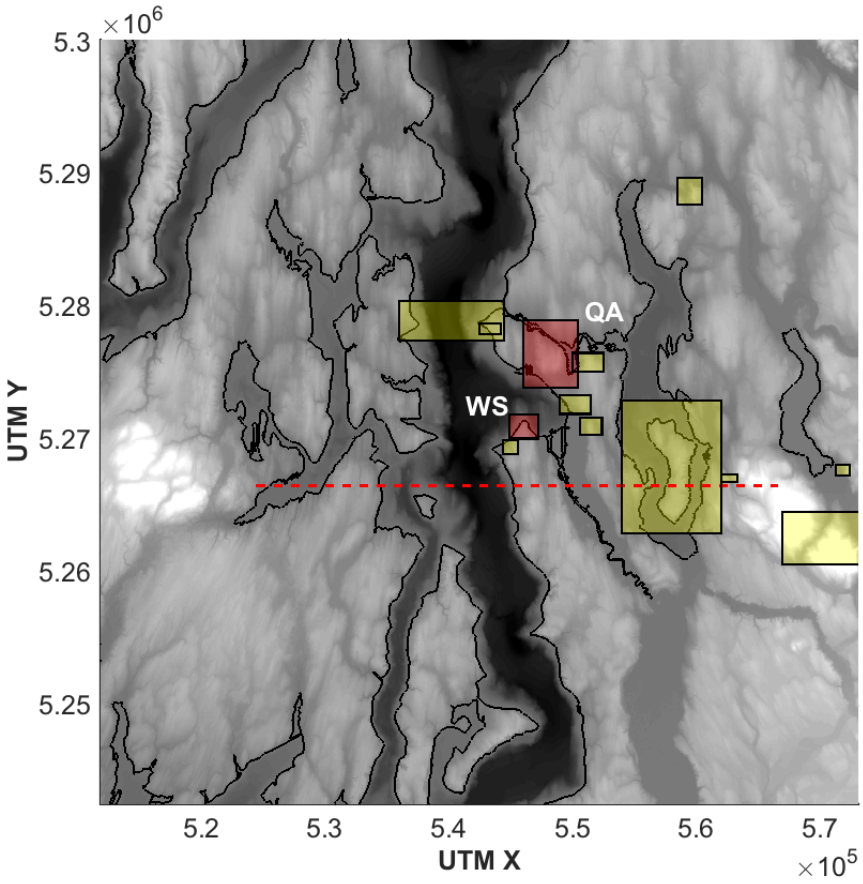

Figure 3.13. Topographies investigated using local, targeted synthetic seismogram arrays. Colored boxes cover the extent of each targeted array. Red boxes correspond to West Seattle (WS) and Queen Anne (QA).

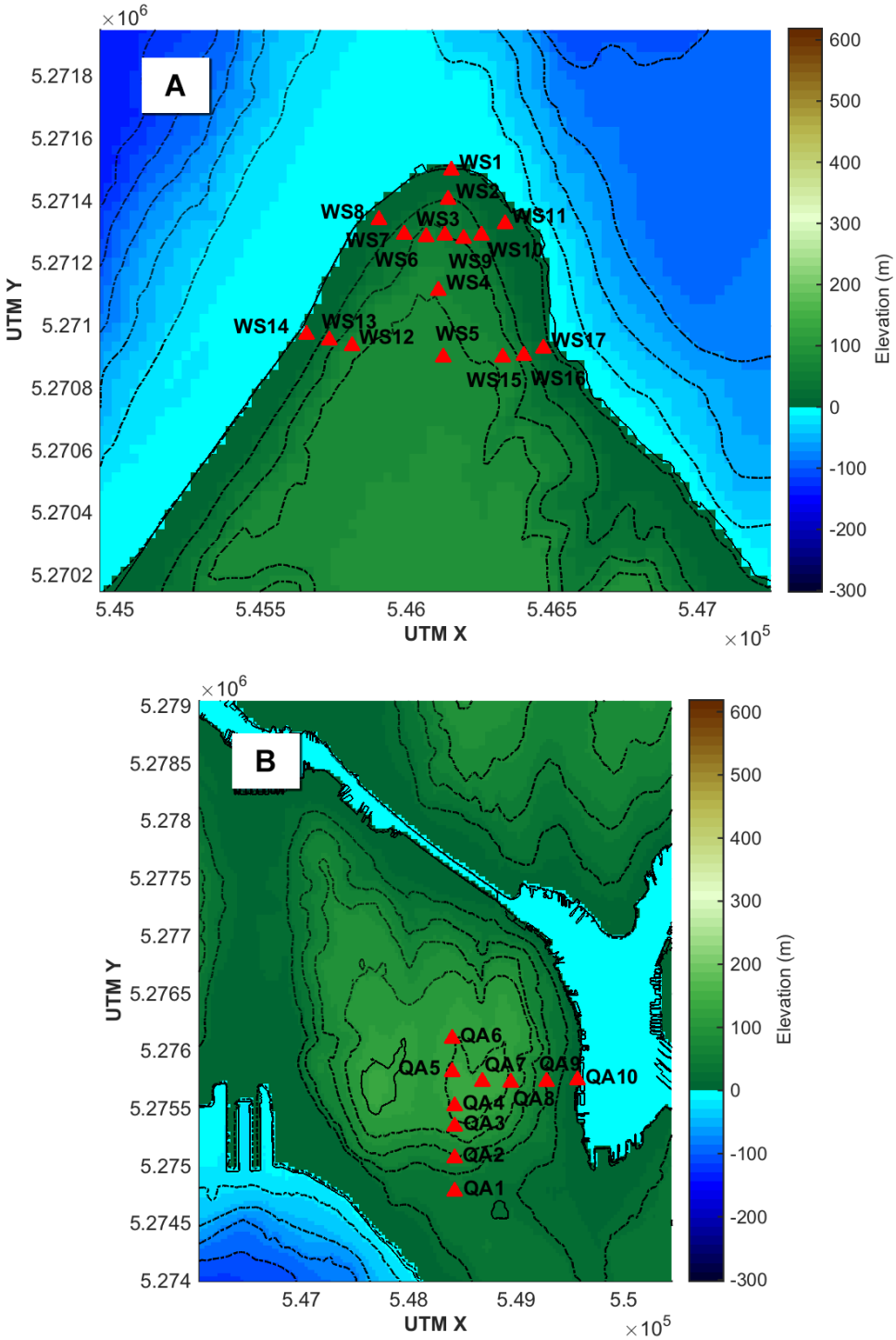

Figure 3.14. Topography and location of synthetic seismometers on (A) West Seattle and (B) Queen Anne.
Contour interval is 25 m.

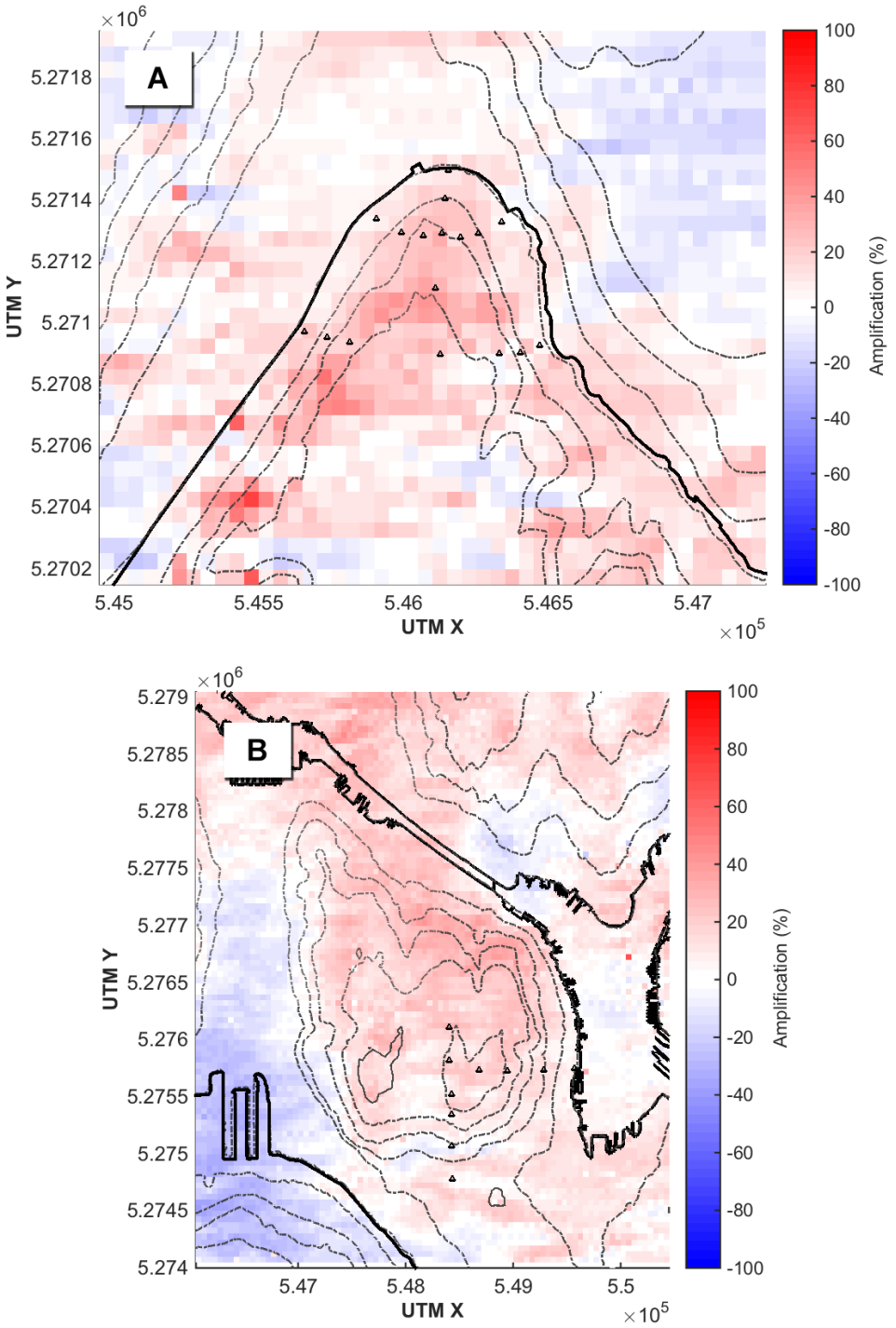

Figure 3.15. Horizontal PGV amplification on West Seattle and Queen Anne for simulation S2E.

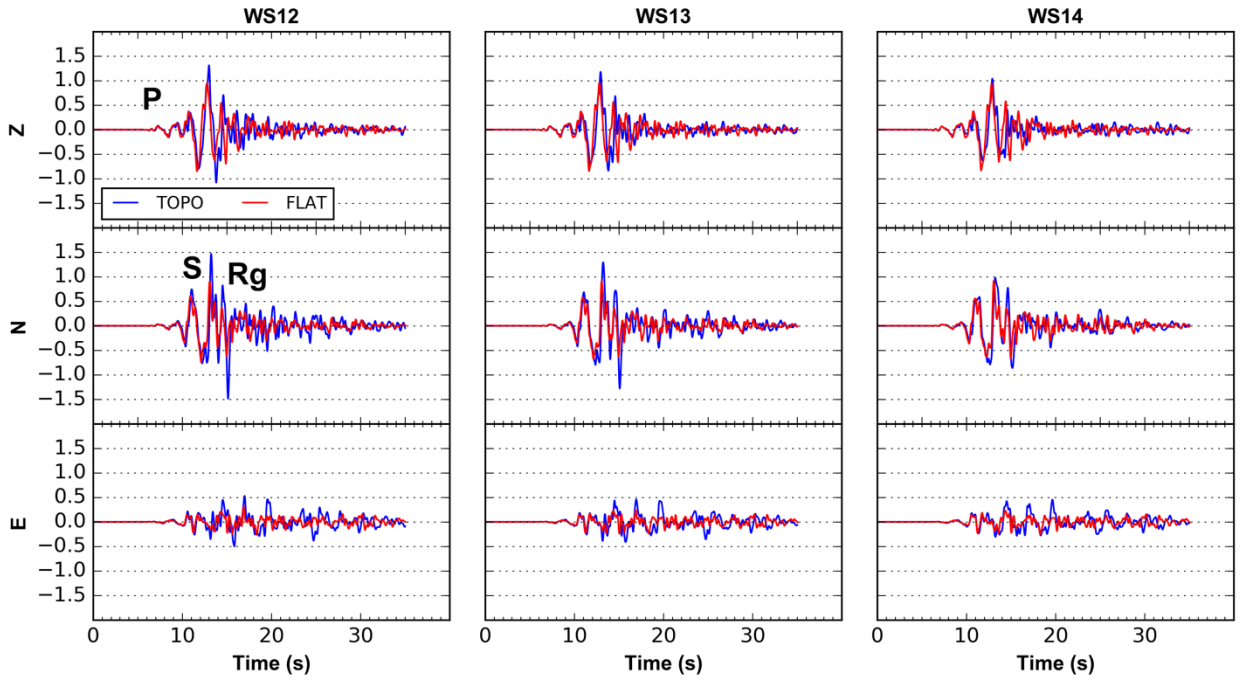

Figure 3.16. Three-component velocity seismograms recorded on the top (WS12), slope (WS13), and bottom (WS14) of a cliff at West Seattle (simulation S2E). The P, S, and surface (Rg) waves are labelled for station WS12.

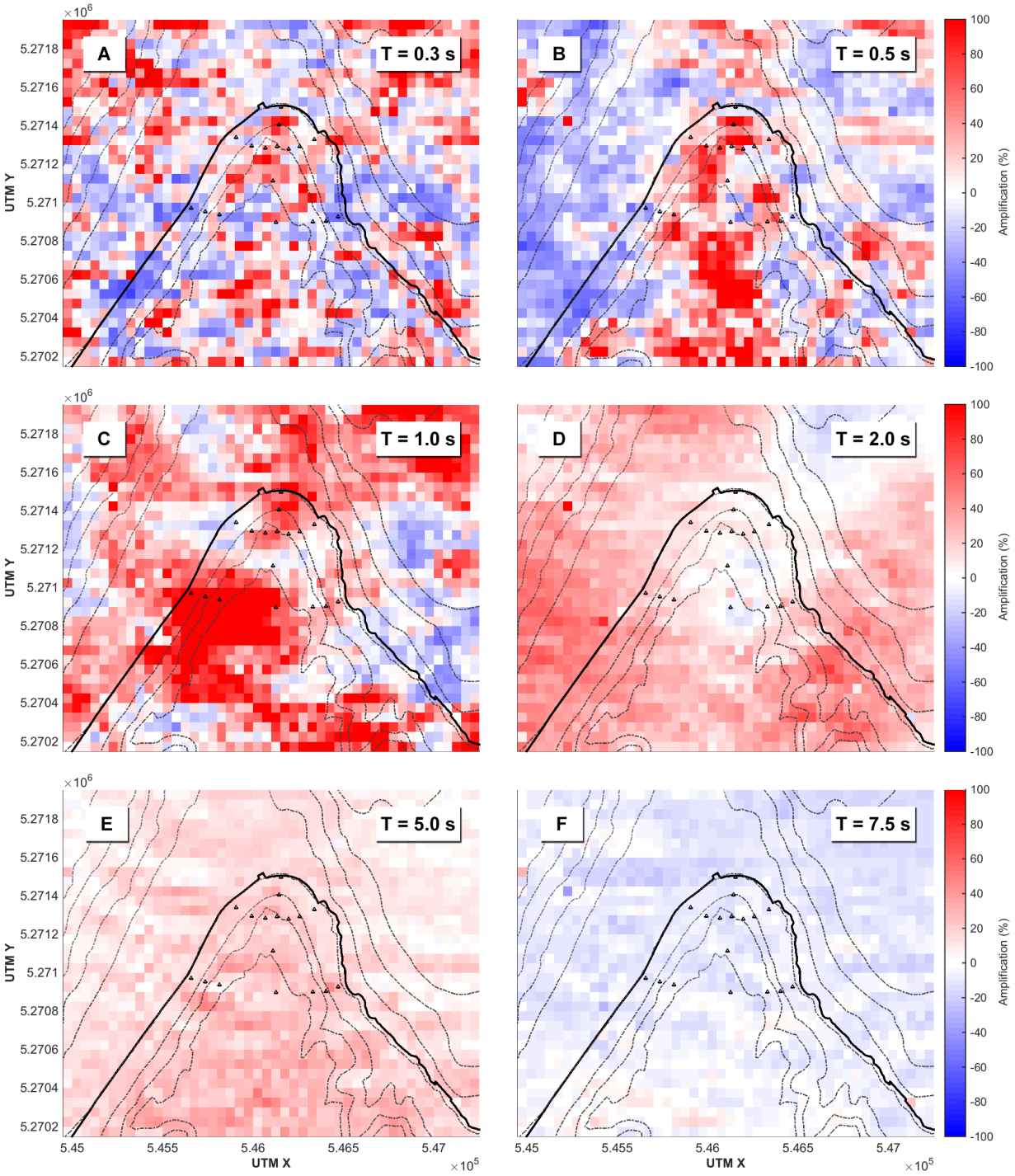

Figure 3.17. Horizontal PGV amplification on West Seattle for simulation S2E at periods of (A) 0.3 s, (B) 0.5 s, (C) 1.0 s, (D) 2.0 s, (E) 5.0 s, and (F) 7.5 s.

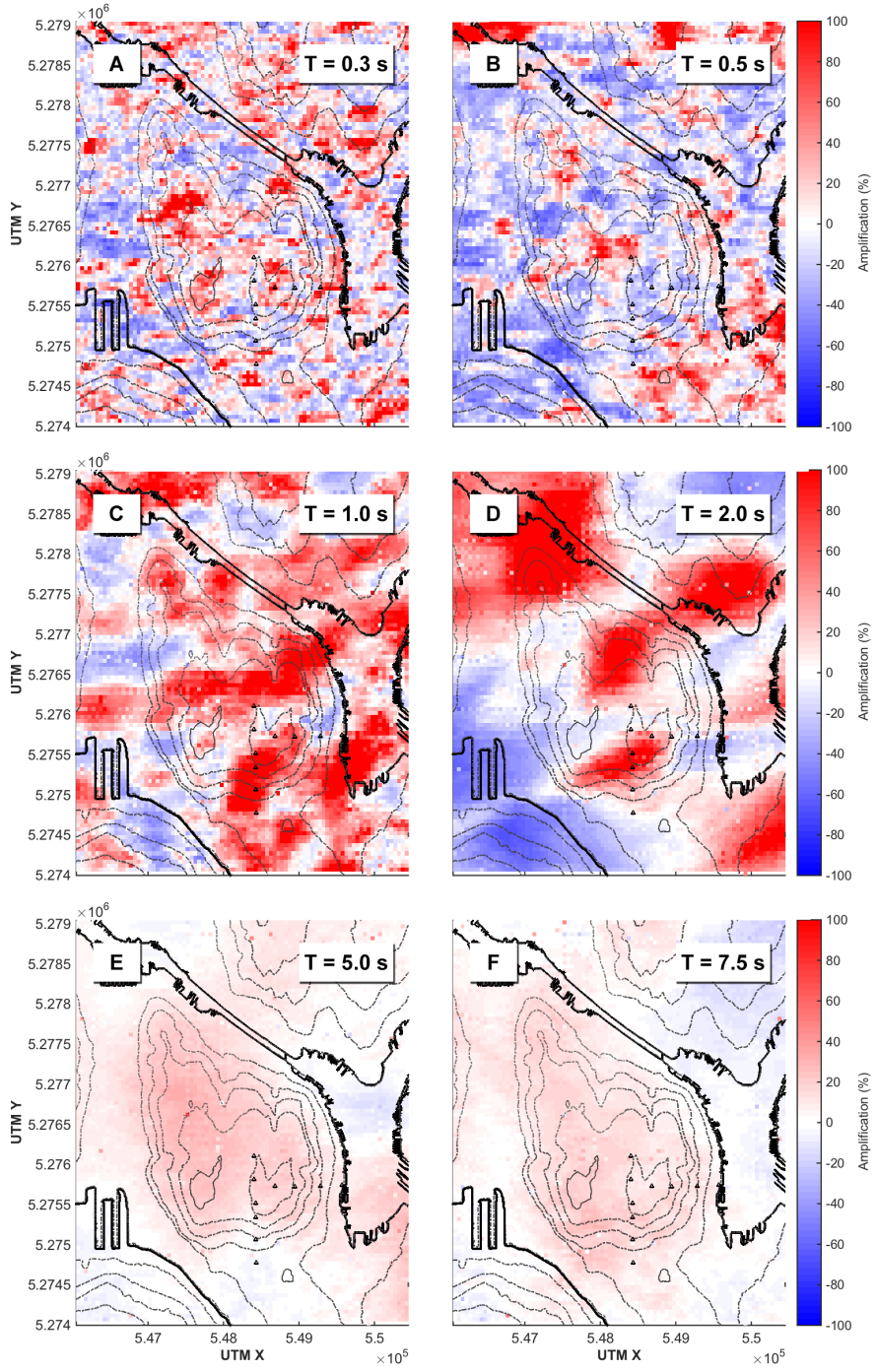

Figure 3.18. Horizontal PGV amplification on Queen Anne for simulation S2E at periods of (A) 0.3 s, (B) 0.5 s, (C) 1.0 s, (D) 2.0 s, (E) 5.0 s, and (F) 7.5 s.

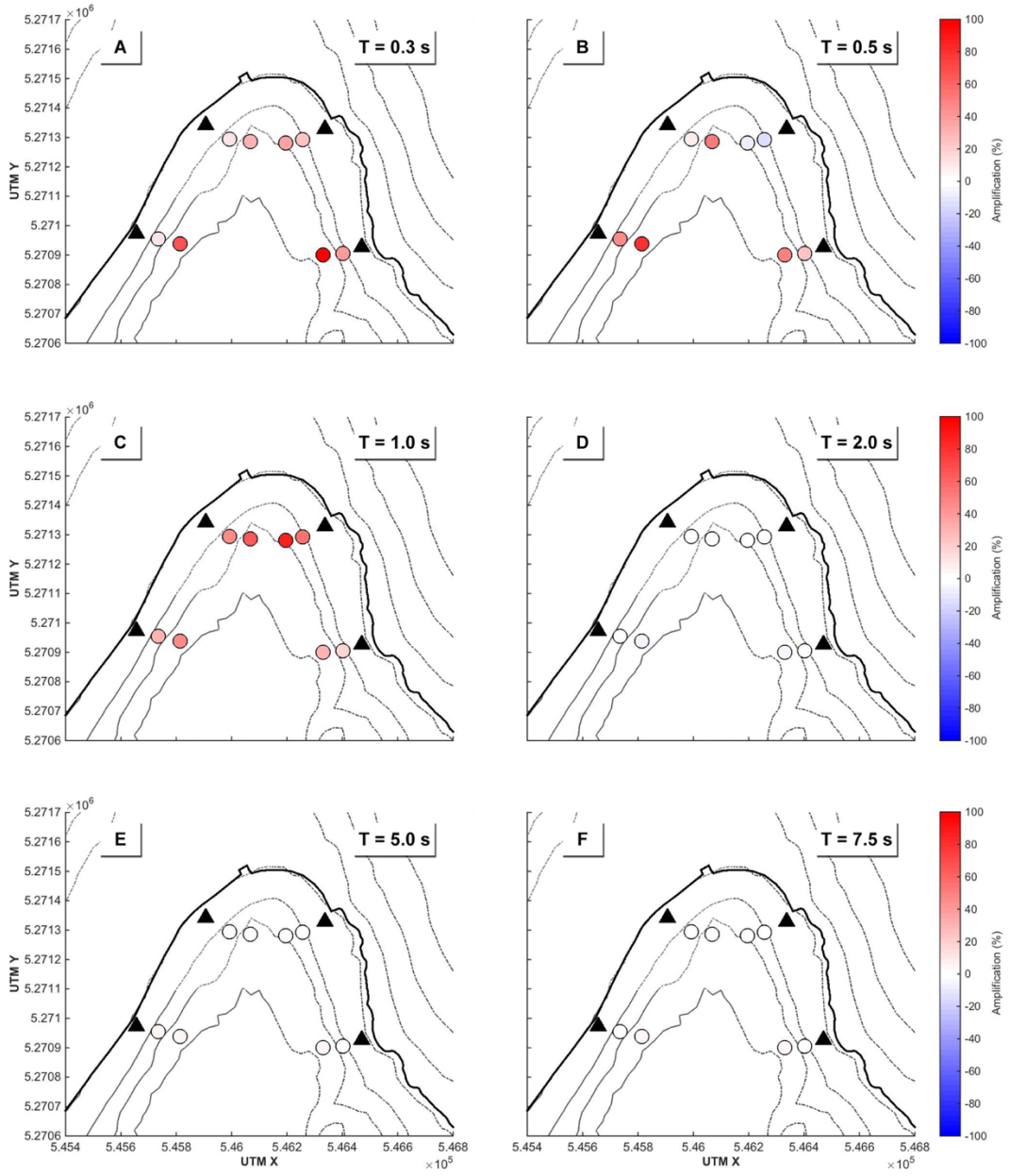

Figure 3.19. Top-over-bottom horizontal PGV amplification at targeted array stations on West Seattle for simulation S2E.
Periods of ground motion considered are (A) 0.3 s, (B) 0.5 s, (C) 1.0 s, (D) 2.0 s, (E) 5.0 s, and (F) 7.5 s. Top and slope stations are represented by colored circles, while the bottom stations are represented by black triangles. The amplification values represent the PGV amplification at the top and slope stations relative to the bottom stations.

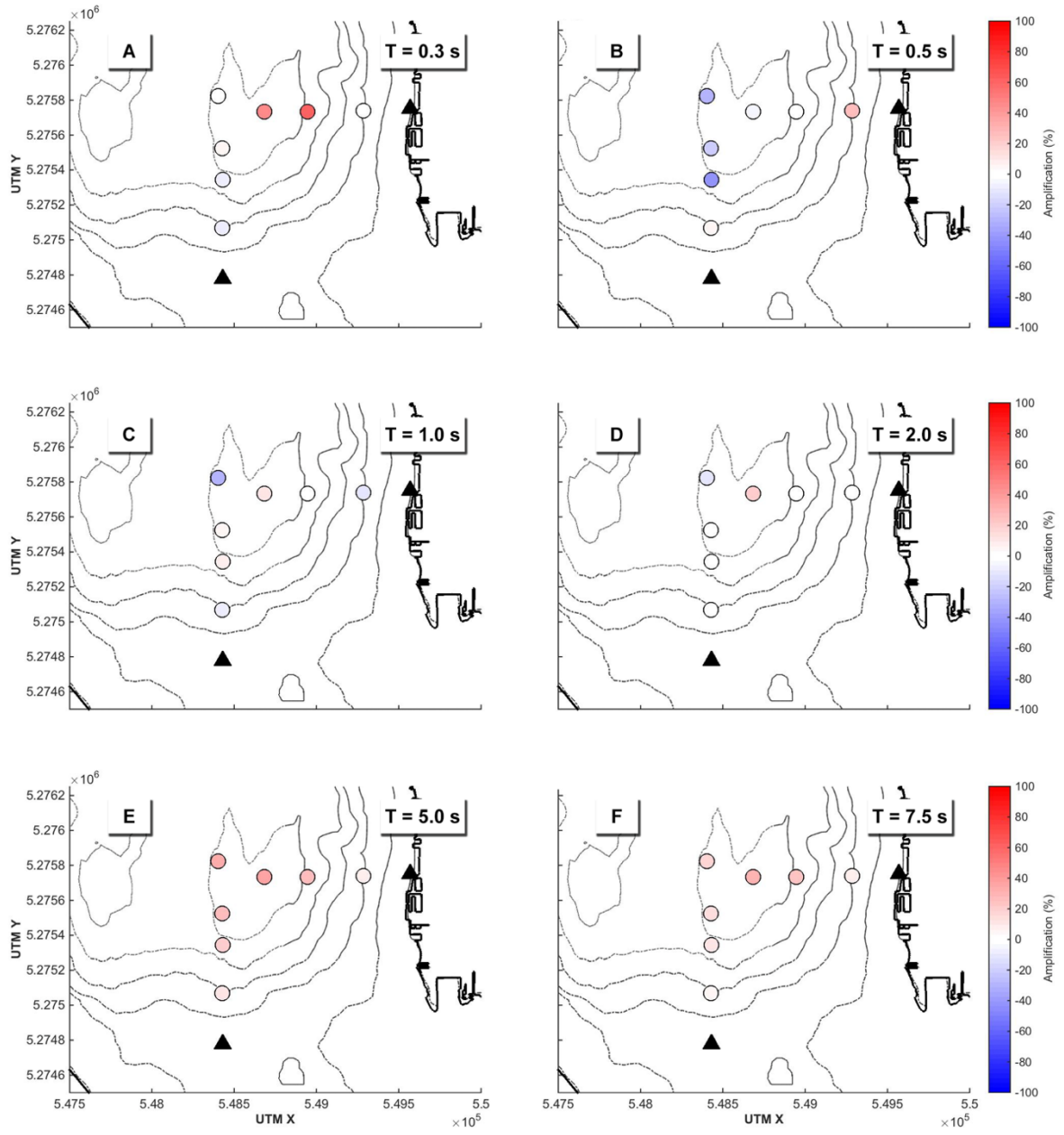

Figure 3.20. Top-over-bottom horizontal PGV amplification at targeted array stations on Queen Anne for simulation S2E.
Periods of ground motion considered are (A) 0.3 s, (B) 0.5 s, (C) 1.0 s, (D) 2.0 s, (E) 5.0 s, and (F) 7.5 s. Top and slope stations are represented by colored circles, while the bottom stations are represented by black triangles. The amplification values represent the PGV amplification at the top and slope stations relative to the bottom stations. For Queen Anne, QA1 was used as the base station for QA2, QA3, QA4, and QA5, while QA10 was used as the base station for QA7, QA8, and QA9.

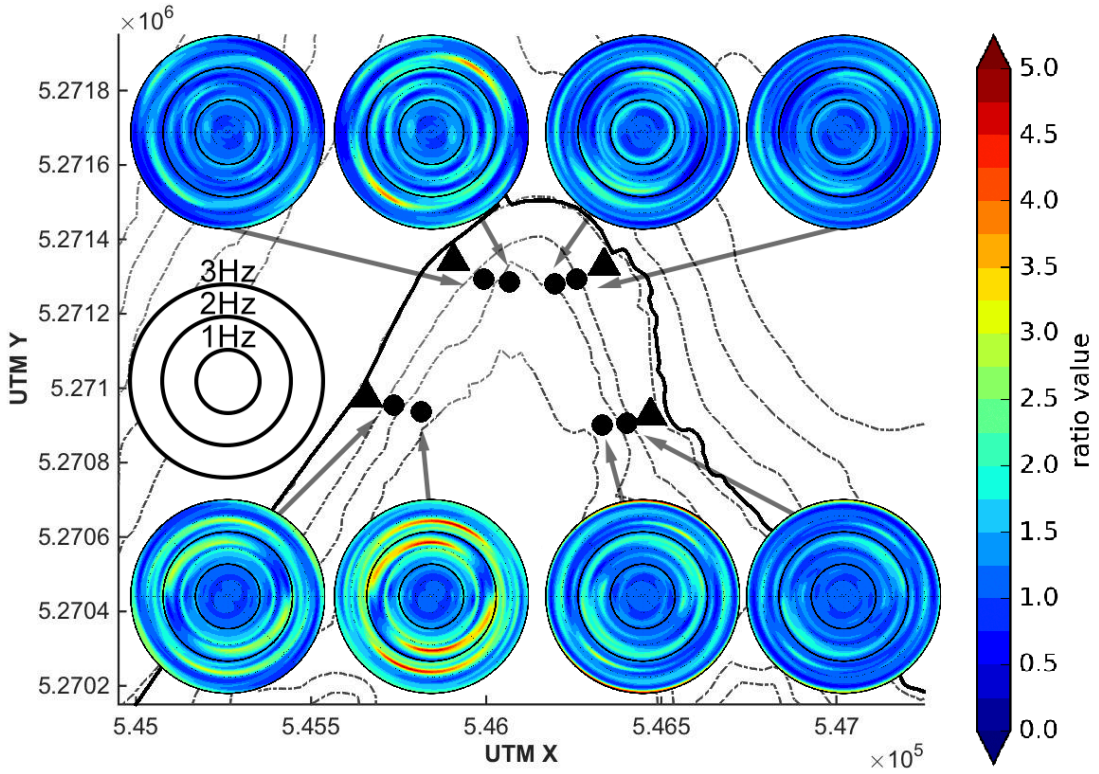

Figure 3.21. Polarization of horizontal spectral ratios on West Seattle (simulation S2E). Ratios are calculated by dividing the rotated spectral response from stations at the top and slope of the cliff (black circles) by the spectral response at the bottom of the cliff (black triangles). Frequency increases outward from the center of the plot, while azimuths correspond to compass directions. Concentric rings mark 1 Hz intervals, with the innermost ring representing 1 Hz, and the outermost ring representing 3 Hz. Colors correspond to the value of the spectral ratio at a particular frequency and azimuth. Ratio values greater than one represent amplification relative to the bottom station, while values less than one represent de-amplification.

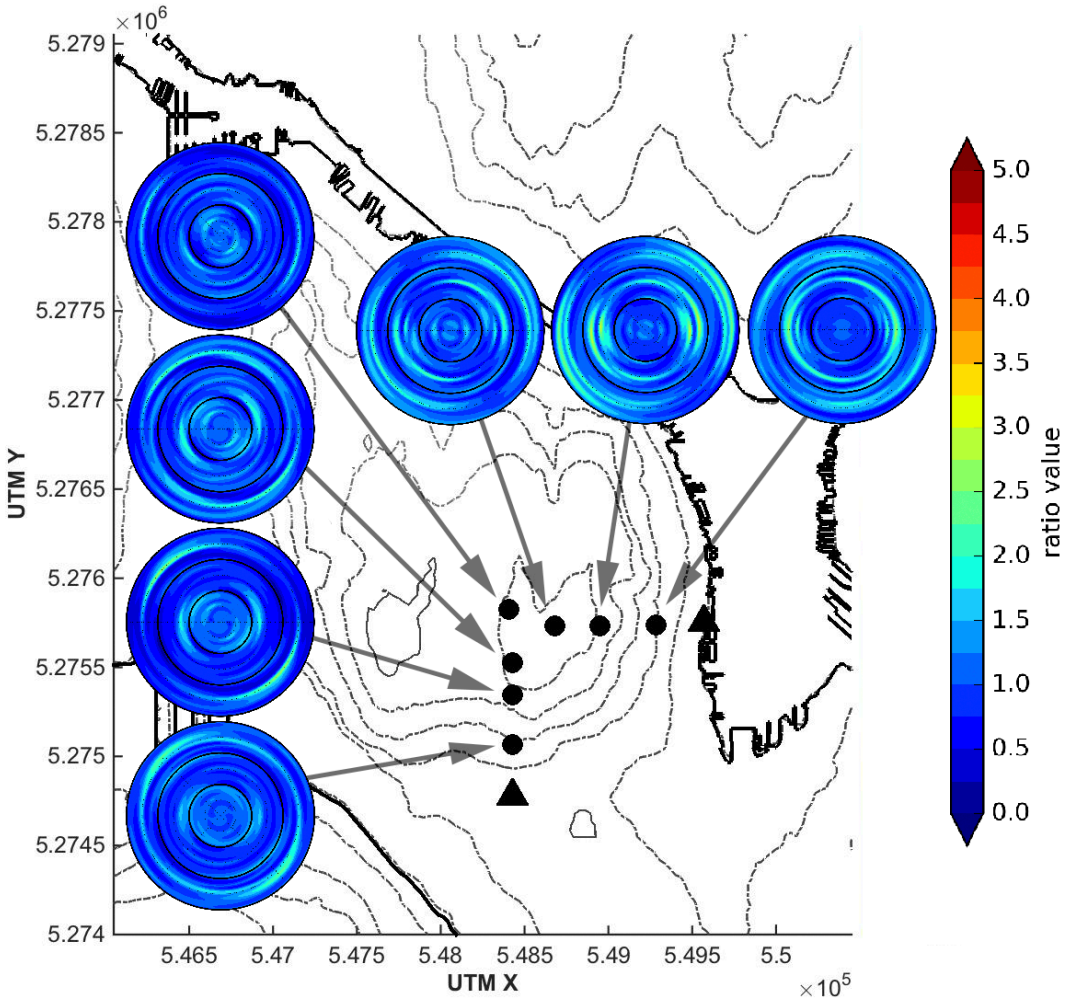

Figure 3.22. Polarization of horizontal spectral ratios on Queen Anne (simulation S2E). Ratios are calculated by dividing the rotated spectral response from stations at the top and slope of the cliff (black circles) by the spectral response at the bottom of the cliff (black triangles). Frequency increases outward from the center of the plot, while azimuths correspond to compass directions. Concentric rings mark 1 Hz intervals, with the innermost ring representing 1 Hz, and the outermost ring representing 3 Hz. Colors correspond to the value of the spectral ratio at a particular frequency and azimuth. Ratio values greater than one represent amplification relative to the bottom station, while values less than one represent de-amplification.

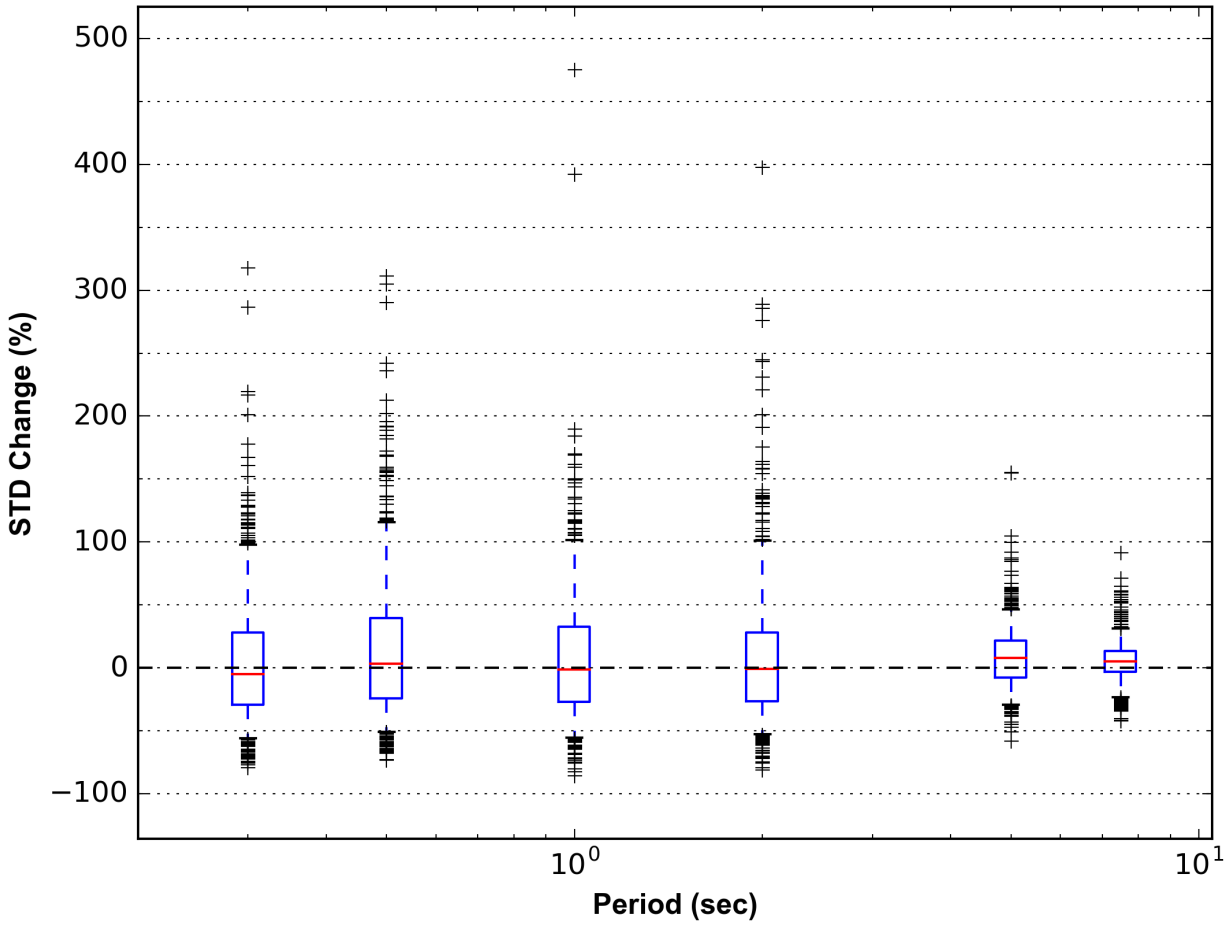

Figure 3.23. Distribution describing the change in standard deviation (STD) between the flat and topography simulations across all stations in the uniform grid.
Location along the x-axis represents the period of ground motion. Each box bounds 50% of observations, with the red line representing the mean value of the distribution. Whiskers bound 90% of observations. Positive values represent an increase in standard deviation in the topography simulation relative to the flat simulation, while negative values represent a decrease in standard deviation.

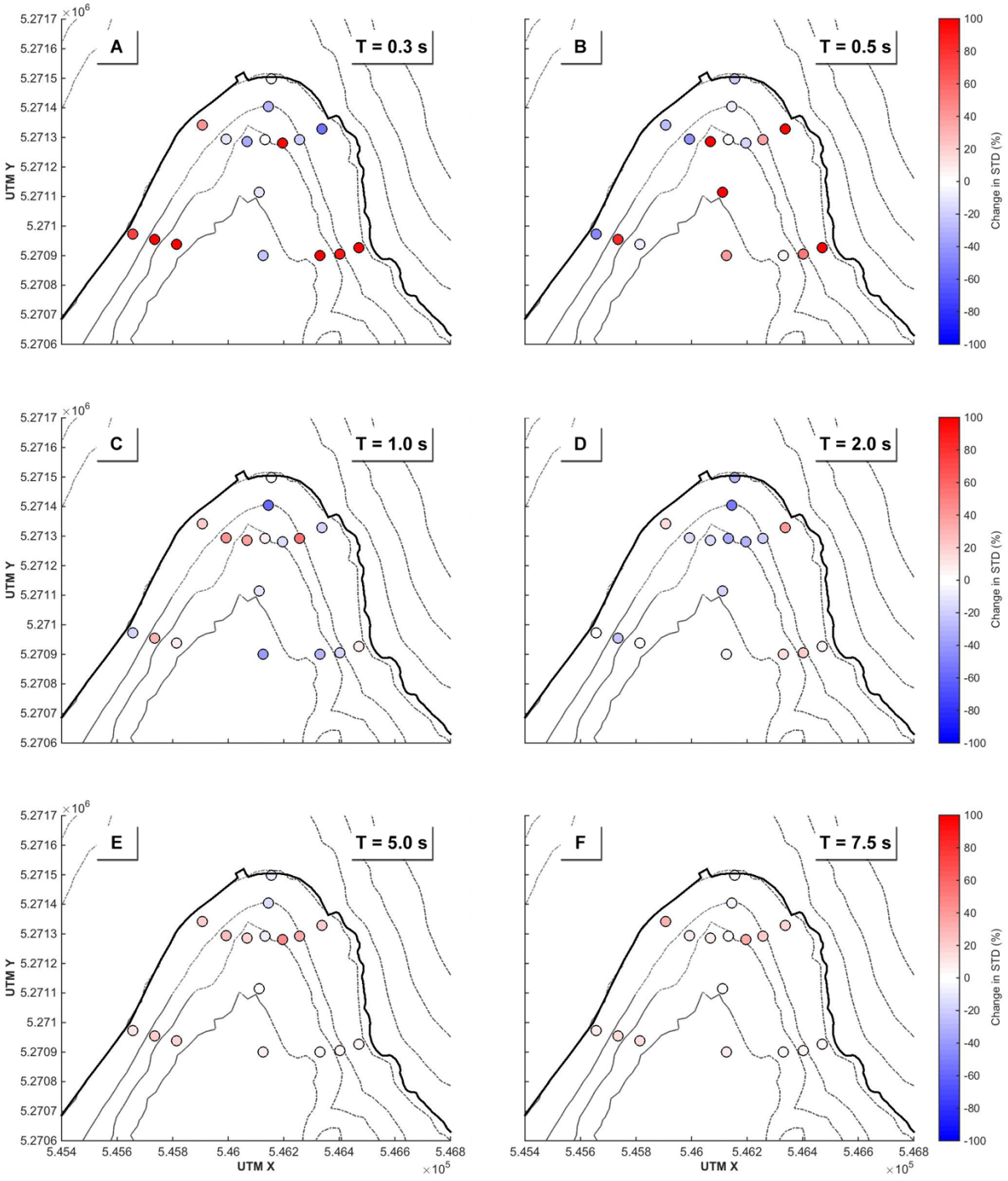

Figure 3.24. Change in inter-event standard deviation (STD) between the topography and flat simulations on West Seattle.

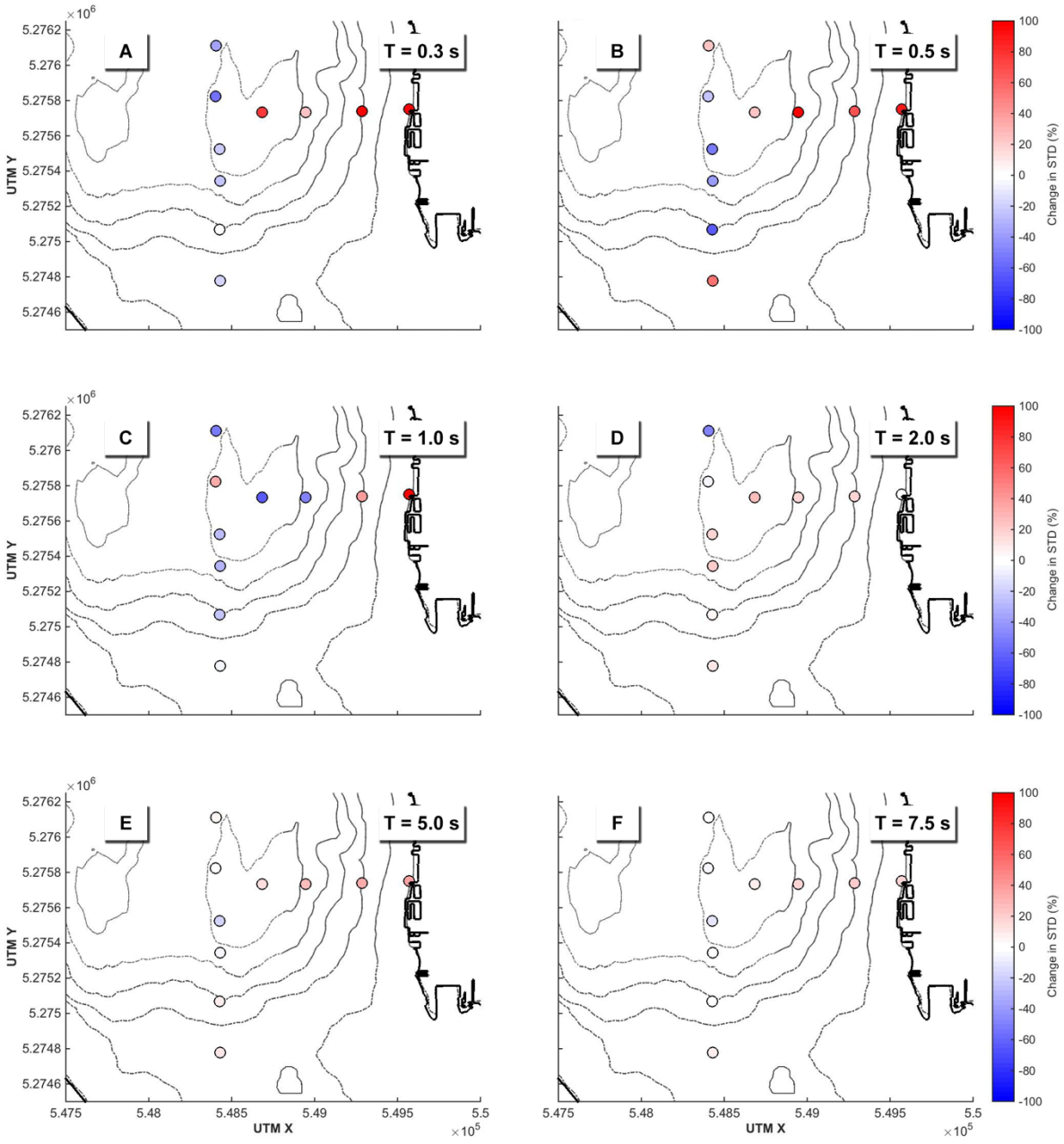

Figure 3.25. Change in inter-event standard deviation (STD) between the topography and flat simulations on Queen Anne.

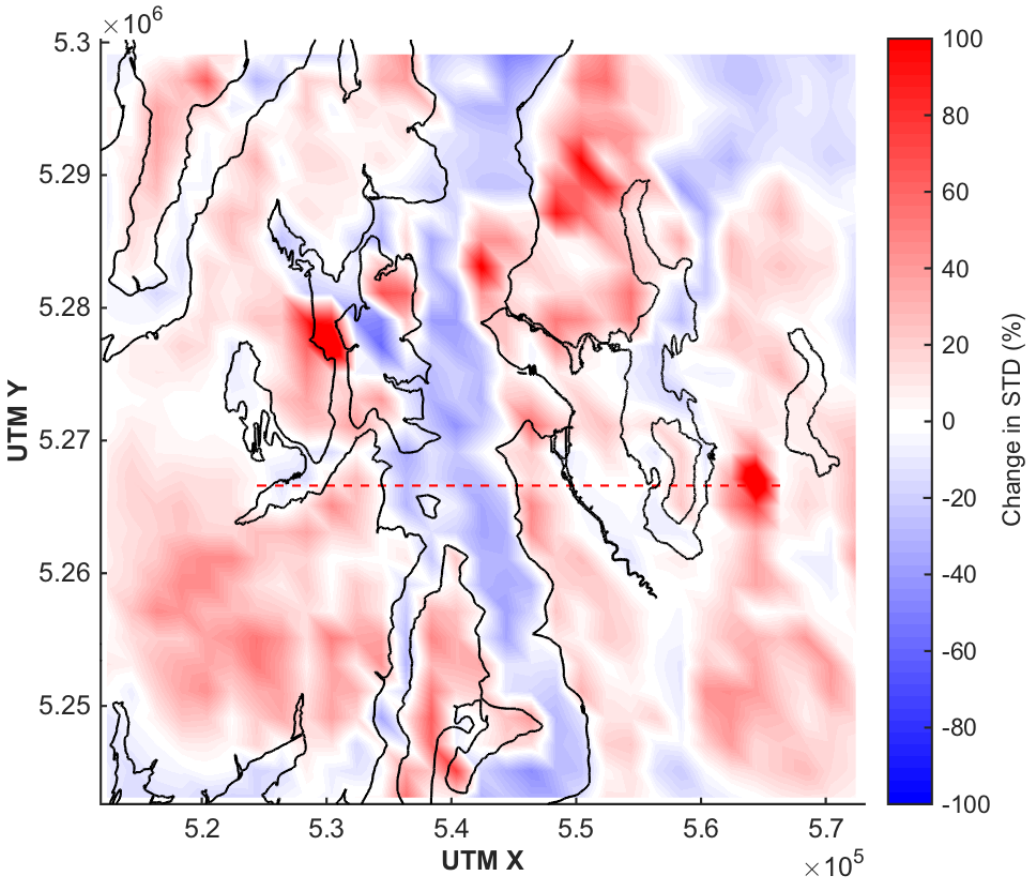

Figure 3.26. Change in inter-event standard deviation (STD) between topography and flat simulations across all grid stations at a period of T=5.0 s.
Warm colors indicate an increase in standard deviation in the topography simulation relative to the flat simulation, while cool colors indicate a decrease.

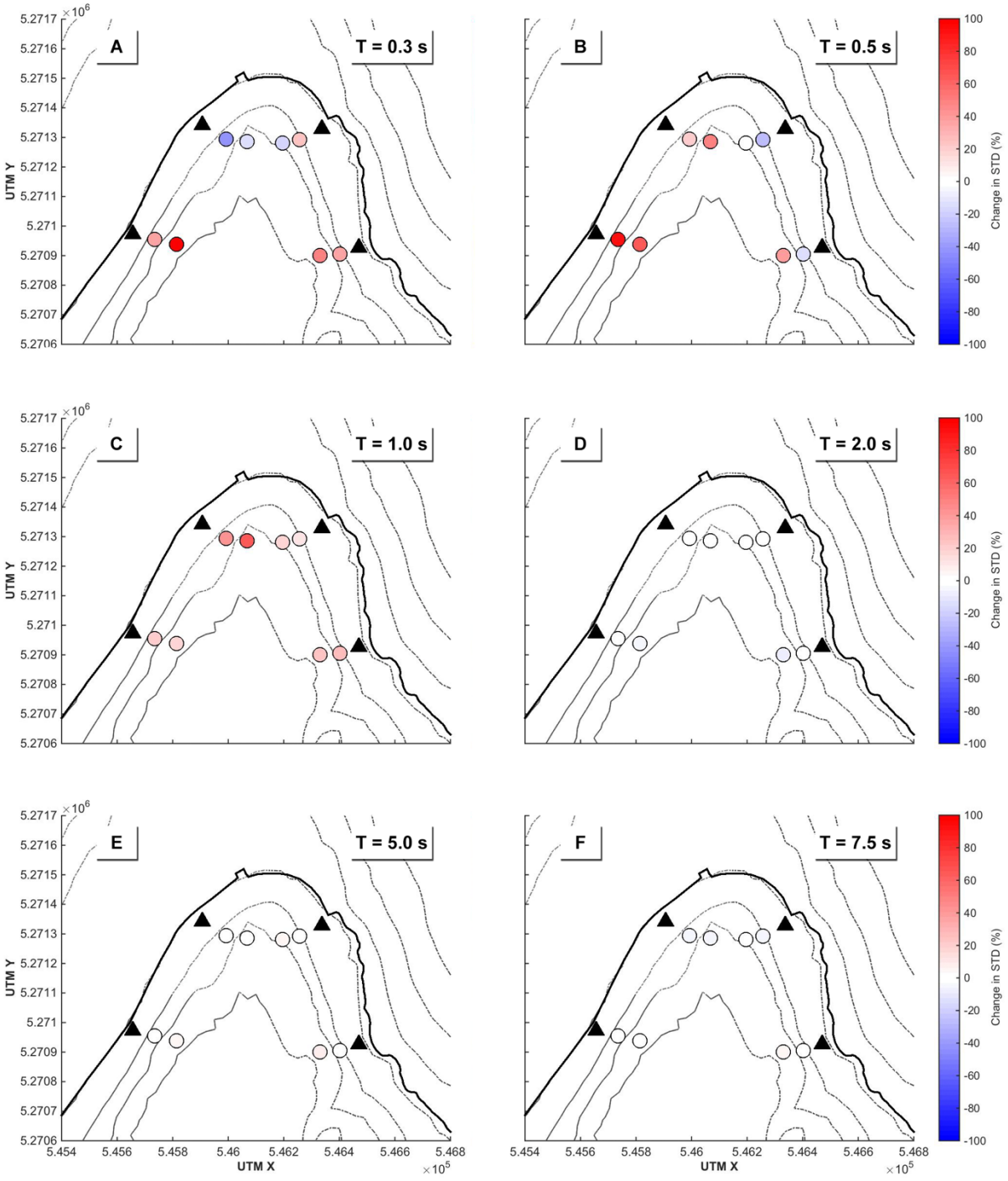

Figure 3.27. Change in inter-event standard deviation (STD) between the top and bottom stations on West Seattle.
Top and slope stations are represented by colored circles, while the bottom stations are represented by black triangles.

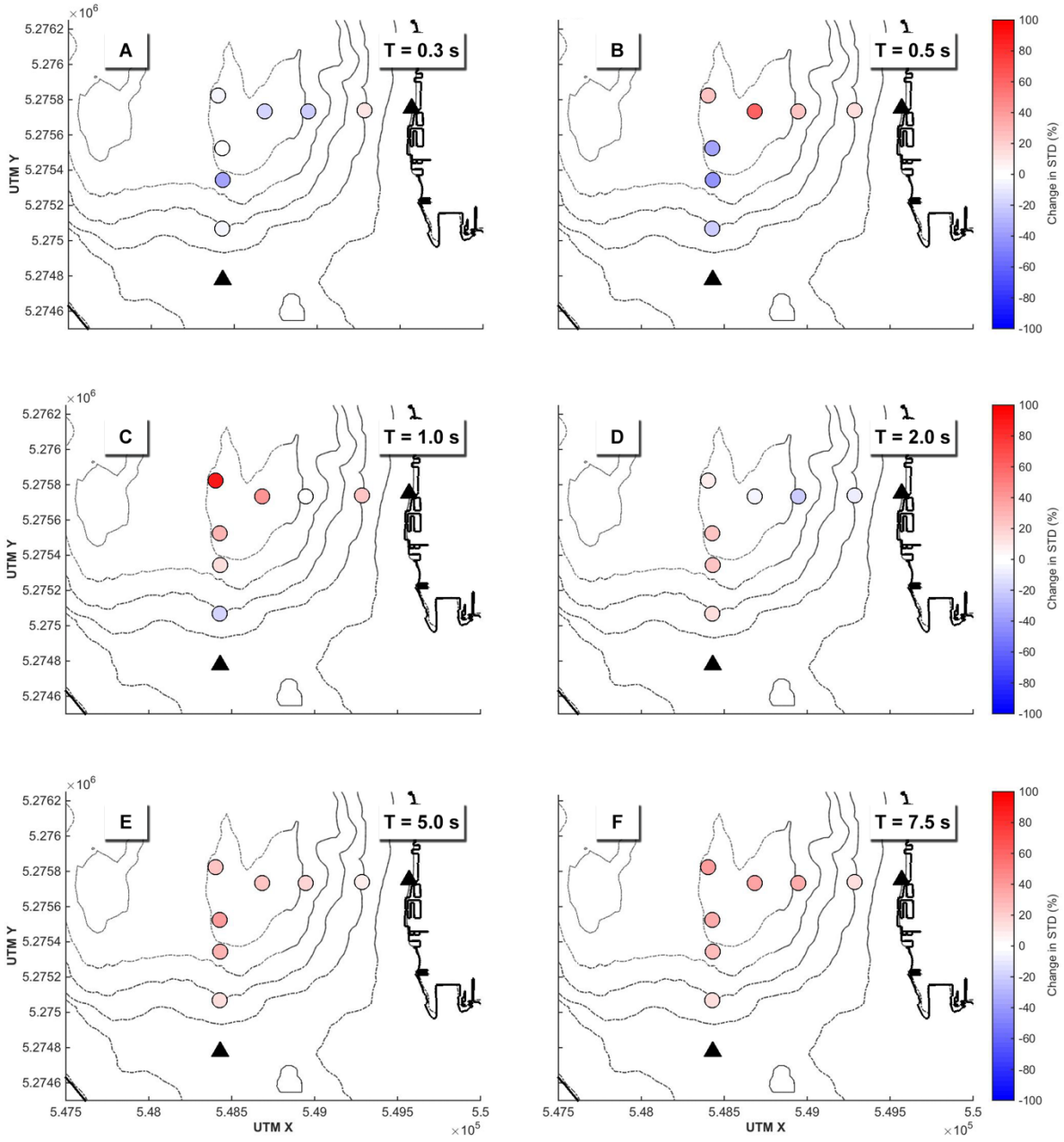

Figure 3.28. Change in inter-event standard deviation (STD) between the top and bottom stations on Queen Anne.
Top and slope stations are represented by colored circles, while the bottom stations are represented by black triangles.

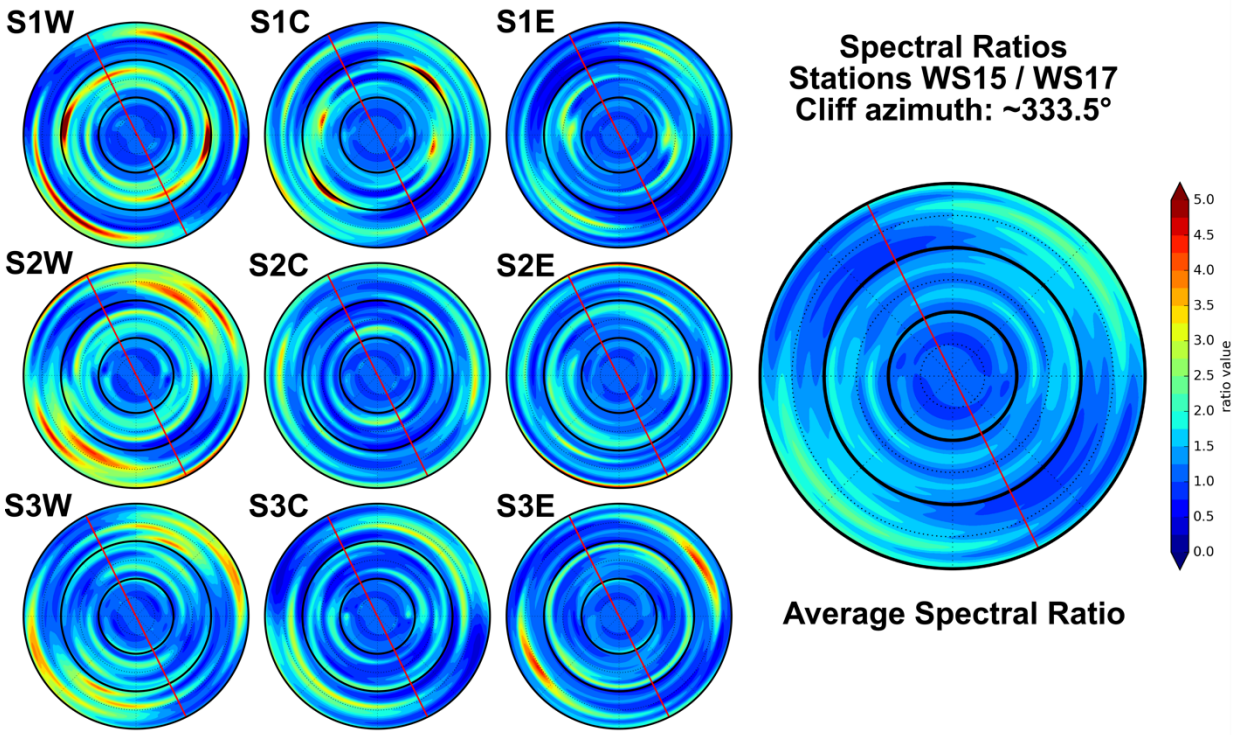

Figure 3.29. Polarization of horizontal spectral ratios between stations WS15 (top of cliff) and WS17 (bottom of cliff) on West Seattle.
The 3X3 grid represents the spectral ratio between the stations for all nine simulations; columns correspond to hypocenter location (from left to right: west, central, and east hypocenter); rows correspond to slip distribution (from top to bottom: slip distribution 1, 2, and 3). The large polar plot on the right corresponds to the geometrically averaged response of all the rose plots in the grid. The red line corresponds to the cliff's orientation. The ratio value color scale is the same across all plots.

6. Tables

Table 3.1. Summary of topography and flat simulation parameters.

Minimum S-wave velocity (m/s):	450
Maximum frequency modeled (Hz):	3.0
Model dimensions (km):	61.2 X 57.6 X 28.8
Elements:	29,048,832
Processors required:	2048
Node hours per run (topo. / flat):	1,344 / 889
Wall-clock hours per run (topo. / flat):	42 / 28
Simulation duration (s):	35
Δt (s) (topo. / flat):	4.0E-4 / 5.5 E-4
Total timesteps (topo. / flat):	87,500 / 63,700

Table 3.2. Labelling scheme for simulation scenarios.

	Slip Distribution #1	Slip Distribution #2	Slip Distribution # 3
West Hypocenter	S1W	S2W	S3W
Central Hypocenter	S1C	S2C	S3C
East Hypocenter	S1E	S2E	S3E

IV. Structure and Qp-Qs relations in the Seattle and Tualatin basins from converted seismic phases

This chapter is submitted for publication in *Bulletin of the Seismological Society of America*.

1. Introduction

Sedimentary basins affect earthquake ground motion in a variety of ways and can significantly contribute to seismic hazard in a given area. The large impedance contrasts between the basin materials and underlying bedrock may directly amplify seismic waves, while a basin's geometry can focus and trap seismic energy. With many large metropolitan areas located in basins adjacent to active fault zones, these effects have been directly observed on many occasions and are often invoked to help explain conspicuous, localized damage during earthquakes (Asimaki et al. 2017; Hartzell et al. 1997; Kawase 1996; Stephenson et al. 2006). As such, it is critical for seismologists to have a strong understanding of sedimentary basin structure. Besides providing insight into the tectonic processes that formed a basin and how seismic waves may behave within that basin, a good structural model allows for accurate and explicit simulation of seismic wave propagation. The addition of basin structure to seismic hazard models has significantly improved estimates of ground motion and expanded the understanding of phenomena like basin-generated surface waves and edge effects (Frankel and Stephenson 2000; Frankel, Stephenson, and Carver 2009; Stephenson et al. 2006).

In regions without extensive geologic characterization, the task of building a basin model can be difficult, particularly where there are few resources for active-source seismic experiments. In many cases, passively gathered seismic data may provide the only means to image the subsurface. Receiver function methods commonly compare the differential travel times of P and P-to-S (or S and S-to-P) phases from passively-recorded teleseismic earthquakes to estimate the

depth to the Moho or a subducted slab beneath a seismometer (e.g., Audet et al. 2010). Similarly, local earthquake recordings may be used to constrain shallow crustal structure by directly exploiting these converted seismic phases.

We use converted seismic wave arrivals from crustal earthquakes to characterize the structure of sedimentary basins the Pacific Northwest. Specifically, we focus on the Seattle Basin in Washington and the Tualatin Basin in Oregon. These features represent two end-members for characterization; the structure of the Seattle Basin has been well studied using a variety of active source (Brocher et al. 2001; Li et al. 2006 ; Pratt et al. 1997; Snelson et al. 2007; Van Wagoner et al. 2002) and passive source (Pratt and Brocher 2006; Ramachandran, Hyndman, and Brocher 2006) seismic methods. As such, the Seattle Basin provides a strong basis for evaluating the accuracy of the methods applied in this study. In contrast, the Tualatin Basin has had no comprehensive seismic surveying, and its structure is relatively under-characterized. In both of these basins, the strong impedance contrast between the underlying basement and overriding basin materials – as well as between layers within the basin – generates clear, high-amplitude P-to-S and S-to-P converted phases. By comparing the arrival times of these phases to their associated parent P- and S-wave arrivals and assuming a 1-D velocity model, we calculate the depth-to-basement under multiple seismic stations. Our analysis also reveals the presence of a spatially-extensive volcanics layer embedded within the Tualatin Basin beneath the Columbia River Basalts Group (CRBG). Using our calculated depths, we then estimate the average relationship between Qp and Qs beneath each station using a spectral ratio method. We show that our analyses produce results that are consistent with commonly applied active and passive tomography methods, providing an additional means for basin structural characterization in areas without extensive seismic surveying.

Geologic and Tectonic Setting

The Seattle Basin is located in the Puget Sound region of Washington (Figure 4.1A). North-south, arc-parallel shortening of western Washington through the Cenozoic era has led to the creation of three east-west trending, thrust-fault-bound basins, the largest of which is the Seattle Basin (Johnson, Potter, and Armentrout 1994; Wells, Weaver, and Blakely 1998). The basin is bound to the south by the Seattle Fault, and on the northeast by the Southern Whidbey Island Fault (Johnson, Potter, and Armentrout 1994); the basin terminates to the east and west against the Cascade and Olympic Mountains, respectively. Magnetic and tomographic inversions suggest the basin reaches its deepest depth of ~9 km near the center of its southern boundary against the Seattle Fault, before gradually tapering in depth to the north, east, and west (Brocher et al. 2001). The northern portions of the basin are underlain by the Kingston Arch, a broad, east-west-trending antiform that tilts basin materials up by 30° (Pratt et al. 1997). Basin fill is largely consolidated, Tertiary-age, marine and nonmarine sediments, though unconsolidated gravels from Quaternary glacial advances compose the upper ~1 km. Underlying the basin are the regionally-extensive, marine and nonmarine basalts of the Crescent Formation (Johnson, Potter, and Armentrout 1994; Johnson et al. 1999). The basin is notable from a seismic hazard standpoint in that it amplifies earthquake ground motion in a variety of ways. Besides the amplification associated with the large bedrock-to-basin velocity contrast, the basin also produces high-amplitude, basin-edge-generated surface waves and focuses seismic energy at locations along its southern border adjacent to the Seattle Fault (Frankel, Carver, and Williams 2002; Frankel, Stephenson, and Carver 2009; Stephenson et al. 2006).

A similarly deep sedimentary basin, the Tualatin Basin, is located in northwestern Oregon (Figure 4.1B). Basin growth initiated in the early Cenozoic era, accommodating relative

extension between the dextrally-shearing Gales Creek and Portland Hills Fault Zones, which bound the basin to the southwest and northeast, respectively (Blakely et al. 2000; McPhee et al. 2014). Subsequent north-south compression (Werner, Graven, and Berkman 1991) has folded the basin fill and led to the creation of the Beaverton Fault Zone, an east-west thrust-fault that bisects the basin near its center (Yeats et al., 1996). Gravity inversions suggest the basin reaches depths of ~6.5 km near the middle of its western margin, adjacent to where the Beaverton and Gales Creek Fault Zones intersect. Around 1 km of north-verging vertical offset on the Beaverton Fault is resolvable from the gravity inversions (McPhee et al., 2014). Within the basin, thick sequences of marine sediments are interbedded with deposits from regional volcanism, including ash, pumice beds, and lava flows (Yeats et al., 1996). The basin is capped by lava flows from the Columbia River Basalt Group (CRBG), which reach thicknesses up to 300 m in some locations (Newton 1969). These deposits are overlain in places by a relatively thin layer of fluvial sediments. The regional basement is a combination of materials from the Siletz River, Tillamook, and Waverly Heights volcanic groups (McPhee et al., 2014; Yeats et al., 1996).

2. Method & Results

Data Selection and Phase Picking

All earthquake locations and origin times used in this study were taken from the catalog of the Pacific Northwest Seismic Network (PNSN), which is the primary authority for regional seismicity. For the Seattle Basin, only earthquakes with origin depths between 20 and 40 km were selected. The 20 km cutoff was chosen to avoid shallower events that would have more horizontal ray-paths; the 40 km cutoff was chosen to avoid events originating within the subducting Juan de Fuca slab, whose records may have additional converted phases from the

slab-mantle interface and overriding plate Moho. A magnitude threshold of M_{local} >= 2.5 was determined to be a reasonable lower-bound for ensuring recognition of converted phases on most stations. All of the stations used in our analysis of the Seattle Basin were equipped with three-component, strong motion sensors.

Extra care was taken to only use earthquakes within a certain horizontal radius of each station. Because both the depth and attenuation estimates are based on vertical travel time calculations, it is important to only consider events with near-vertical ray-paths within the basin. Using Snell's law, we estimated that earthquakes within 30 epicentral kilometers of a station should arrive with an incidence angle less than ~20°. In reviewing the PNSN catalog between 2010 and the present, approximately 70 earthquakes in the Puget Sound area satisfied the above criteria, but many were part of localized swarms or were redundant with other earthquakes at a similar location. Therefore, we elected to focus on a subset of 17 well-recorded earthquakes, which represent a diverse distribution of depths and event-to-basin back-azimuths.

Within the Seattle Basin, the most prominent converted phase is the S-to-P (Sp) phase, which manifests as a relatively high amplitude, high frequency arrival between the P- and S-wave arrivals on the seismogram's vertical component (Figure 4.2). The arrival time of the Sp-phase at a given station is nearly constant with respect to the S-wave arrival time from one earthquake to another. Based on the 1-to-3 second delay between the Sp- and S-arrivals, we assume that the Sp phase represents a conversion from the interface between the igneous rock of Crescent Formation and the sedimentary rock of the basin fill. Notably, the phase is not present on stations sited on Crescent Formation rock outside of the Seattle Basin. For every earthquake record at a given station, we picked the P- and Sp-arrivals on the vertical component and the S-arrival on the radial component. Because of the relatively high amount of environmental noise in

the region, we chose to only work with a subset of sixteen stations that recorded strong Sp-arrivals from at least two of these events. The Seattle Basin stations and their associated differential travel times ($T_{S\text{-}Sp}$) are listed in Table 4.1.

In the Tualatin Basin, there were significantly fewer useable earthquakes and stations. As such, we relaxed the selection criteria so that only one record was required per station. (However, we note that the majority of stations had more than one measurement). Unlike the Seattle Basin, the Tualatin Basin also generates a strong P-to-S (Ps) phase, which manifests on the radial component between the P- and S-wave arrivals. The differential travel time between the P- and Ps-phase ($T_{Ps\text{-}P}$) within the Tualatin Basin is shorter than the differential travel time between the S- and Sp-phase, which implies that the converted phases are likely generated at different interfaces. This is supported by observations of secondary Sp-phase arrivals in some records (e.g., the arrival at 6 seconds on KEEL's vertical channel in Figure 4.2), for which the $T_{S\text{-}Sp}$ matches the $T_{Ps\text{-}P}$. Ultimately, we found that eight earthquakes were well recorded at six stations since the year 2000, and we were able to pick both the Ps- and Sp-phases along with the parent P- and S-wave arrivals for our analysis (Table 4.2). As in the Seattle Basin, all Tualatin Basin stations consisted of three-component, strong-motion sensors.

Basin Depth Estimation

The differential travel time between the S- and Sp-phases (or the P- and Ps-phases) may be expressed as a relationship between the basin depth (h) and the average P and S wave velocity in the basin (Vp and Vs):

$$T_{S-Sp} = h * \left(\frac{1}{v_s} - \frac{1}{v_p}\right)$$

Eq. 4.1

If Vp and Vs are known, this equation may be rearranged to solve for the basin depth using observed T_{S-Sp} values. For this study, we adopted an iterative approach to solving this equation, estimating the average velocity over a range of possible basin depths in order to minimize the residual between the calculated and observed T_{S-Sp} values.

Within the Seattle Basin, we utilized information from the USGS' 3-D Cascadia Velocity Model (CVM), which combined the results of several structural and tomographic studies to create a regional model (Stephenson et al., 2017). To calculate the average Vp and Vs beneath each station, we first extracted the velocity structure and thickness of the upper-most layer of Quaternary sediments. The thickness of this layer has been well-constrained throughout the basin using well data and seismic surveys (Johnson et al. 1999; Jones 1996), so it is kept constant throughout our analysis. For the underlying Tertiarty sediments layer, we investigated a range of possible layer thicknesses in an attempt to find the basin depth that best fits the observed T_{S-Sp} values. We set the Vp at the top and bottom of this layer to 2500 m/s and 4300 m/s, respectively. These values correspond to the maximum and minimum Vp in CVM's Tertiary sediments; we also adopted the same Vp/Vs=2 relationship. We then iteratively increased the thickness of the Tertiary layer by 250 m, linearly interpolating the velocity values between the top and bottom of the layer. We combined the Quaternary and Tertiary components and averaged over the resulting profile to obtain each station's underlying Vp and Vs values. We then used these values with the corresponding depth estimate to calculate a predicted T_{S-Sp} value.

The observed T_{S-Sp} value used in the calculations is a weighted average of the recorded travel times at a given station. To put greater emphasis on arrivals with near-vertical ray-paths, records from earthquakes with epicenters less than 15 km from a station were assigned weights

of 1; records at 15-25 km were assigned weights of 0.5; and records at 25-30 km were assigned weights of 0.25.

There has been little work to constrain the velocity structure of the Tualatin Basin below its upper few hundred meters. Though there are no sonic logs that pass through the full sequence of basin materials, there are regional logs that pass through different portions of the geology. We synthesized these regional logs to produce a generalized, 1-D velocity profile for the Tualatin Basin. The wells used and their associated velocity information are included in the supplement at the end of this chapter.

When building the velocity profiles for the Tualatin Basin, we used a step spacing of 100m. A finer spacing was chosen than in the Seattle Basin since the standard deviation of the Tualatin Basin's $T_{Ps\text{-}P}$ values were relatively low. The thickness of the fluvial sediments layer under each station was estimated from water-well and shallow seismic observations (Yeats et al., 1996). P-wave velocities in this layer were assigned using a gradient similar to that applied in the CVM's Quaternary sediments; values were set to 1000, 1620, and 1670 m/s at 100, 200, and 300 m depth, respectively. The thickness of the CRBG for each profile was held constant at 300m. For the materials beneath the CRBG, we adopted the same iterative scheme as was used for Tertiary basin sediments in the Seattle Basin. The minimum and maximum Vp were set to 2500 m/s and 3600 m/s, respectively, and the thickness of the layer was increased in each iteration of the calculation. Similar to the CVM, we set the Vp/Vs relationship to 2.2 in the fluvial sediments, and to 2 in the rest of the basin fill. The Vp/Vs ratio in volcanic materials was set to 1.8, which is similar to that observed in other flood basalt deposits (Planke and Cambray 1998).

The depth calculation in Eq. 4.1 relies on several simplifying assumptions. The first is that the ray paths taken by the parent and converted phases are essentially vertical. Any

significant deviation from verticality due to large epicentral distances or sloping on the basin bottom would increase the differential travel time and result in an overestimation of depth. However, in restricting observations to earthquakes occurring within 30 km and applying a distance weighting scheme when calculating differential travel times, we have attempted to minimize such errors. Estimates could also be complicated by horizontal variability in deep basin geology or the complex geometry of the basin edge, like near the Seattle Fault Zone. Further, the generally low magnitude of the earthquakes and large amounts of noise due to the urban environment mean some error may be introduced in picking arrivals. To constrain the degree to which these factors could affect depth estimates, we recalculated depths assuming a +/- 0.1 second change in $T_{S\text{-}Sp}$, which is the approximate average standard deviation for Seattle Basin stations. Estimated depths changed from their original values by +/- 250 to 500 m. Assumptions that underpin the CVM could also introduce error into the depth calculation, namely the Vp/Vs ratio. Adjusting the Vp/Vs ratio by +/- 5% results in changes in depth of +/- 250 to 750 m.

Attenuation Estimation

To calculate the average attenuation under each station, we applied the method outlined in Clouser & Langston, 1991. As S- and Sp-waves (or P- and Ps-waves) propagate through a basin, they attenuate according to their travel time, as well as the scattering and anelastic attenuation behavior of the basin material. The relationship between the in-basin attenuation and the measured amplitude spectra for S- and Sp-waves may be expressed as:

$$S(f) = A_s(f) T_{Ss} e^{-\pi f t_S / Q_S},$$

Eq. 4.2

$$S_p(f) = A_s(f) T_{Sp} e^{-\pi f t_{Sp} / Q_P}$$

Eq. 4.3

Where f is the frequency in Hz; $A_s(f)$ is the amplitude spectrum of the S-wave incident from below the basin; T_{Ss} and T_{Sp} are the transmission coefficients for the upgoing S- and Sp-waves; t_S and t_{Sp} are the S- and Sp-travel-times in the basin; and Q_S and Q_P are the frequency-independent attenuation factors for S- and P-waves in the basin.

Taking the natural logarithm of the ratio of the Sp-spectrum over the S-spectrum, we get:

$$ln\left[\frac{S_p(f)}{S(f)}\right] = ln\left[\frac{T_{Sp}}{T_{Ss}}\right] + \pi f\left[\frac{t_S}{Q_S} - \frac{t_{Sp}}{Q_p}\right]$$

Eq. 4.4

As such, the log-spectral-ratio in log-amplitude-frequency space will define a line with the slope:

$$m = \pi\left[\frac{t_S}{Q_S} - \frac{t_{Sp}}{Q_P}\right]$$

Eq. 4.5

Rearranging this equation, we can define the relationship between Qs and Qp as:

$$Q_S = t_S\left[\frac{m}{\pi} + \frac{t_{Sp}}{Q_P}\right]^{-1}$$

Eq. 4.6

For both the Seattle and Tualatin Basins, event records were first high-pass filtered at 1 Hz to remove any long-period noise. Then, the parent and converted phase arrivals at each station were windowed with 0.3 s preceding and following the arrival time, and a 0.1-second Hann taper applied. The window length was chosen to adequately capture the arrival while avoiding P- and S-wave coda noise. Each arrival was converted to the frequency domain, and the resulting spectra were smoothed using a Gaussian filter. The Sp/S spectral ratio was then calculated by dividing the smoothed spectra. Since each station recorded multiple earthquakes, a

mean ratio curve was determined by averaging all of the event ratios at a particular station. A least-squares regression was used to fit a line to the mean ratio curve between 2 and 25 Hz for all stations, providing a slope value for Eq. 4.6. We chose the 25 Hz as an upper-bound because the earthquake signal was generally overwhelmed by noise above this frequency, as determined by taking the Fourier transform of the record directly preceding the P-wave arrival. Finally, we calculated P- and S-wave travel times under each station using the 1-D velocity model associated with the best-fit depth from our depth-to-basement calculations. The travel times and slope values were combined in Eq. 4.6 to provide a function for the Qp and Qs relationship within each basin.

Since depths from the first portion of the analysis are used to calculate the attenuation relationships, any assumption that introduces error into a station's depth estimate will introduce error into its attenuation estimate. Because the values we present were derived from a mean of all stations in the basin, however, the depth error at any one station should not contribute significantly to the error in the basin attenuation estimate. To test the impact of systematic errors in the depth calculation on the overall attenuation estimates, we calculate a mean attenuation curve assuming a +/- 5% change in the Vp/Vs ratio and using Qp/Qs=1.2 (explained in following sections). We find that this causes mean Qp and Qs to vary by <1%, demonstrating that the attenuation results are relatively insensitive to systematic errors.

We also note that some event records used in the depth calculation at a given station were not used in the attenuation calculation. The spectral ratios for these events typically demonstrated either unrealistic slope values or were otherwise poorly constrained.

3. Discussion

Seattle Basin Depth Estimates

Basin depth estimates for the 16 stations in the Seattle Basin are shown in Figure 4.3A and are listed in Table 4.1. The basin gradually increases in depth from approximately 3000 m at its north, east, and west margins to a maximum depth of 7500 m beneath station KIMB along the Seattle Fault Zone at the basin's southern boundary. In general, these depths are compatible with observations from regional tomographic and gravity data inversions, though there are some notable differences.

Residuals between the CVM-predicted depths and those calculated in this study are plotted in Figure 4.4. At the southern end of the basin, we estimate the depth under station KIMB as 1200 m deeper than estimated by the CVM. Near the northern end of the basin, our depths under stations LEOT and SCC are 750-850 m shallower than in the CVM. Most other sites have estimated basin depths within 550 m of the CVM value. We note that the CVM has a vertical resolution constrained by its constitutive tomographic inversions, which is around 1000 m (Brocher et al. 2001); thus, disagreements of <1000 m are within the model's uncertainty. However, uniform differences across many adjacent stations may be indicative of systematic errors in the CVM. In particular, near the southern end of the basin, a variety of structural models have been proposed to describe the fault zone (Blakely et al. 2002; ten Brink et al. 2002; Brocher, Blakely, and Wells 2004; Johnson, Potter, and Armentrout 1994; Liberty and Pratt 2008; Pratt et al. 2015), though most assume high-velocity bedrock material overthrusts tilted and fractured low-velocity basin material along one or several ~45°, south-dipping fault surfaces. Such a discontinuity would be difficult to capture with a relatively low-resolution tomographic inversion, and locally deeper depths near the fault could be smeared near the discontinuities,

accounting for the deeper estimates of the results presented here. Conversely, extreme changes in the shape of the basin bottom near the fault zone could consistently produce arrivals at a station from more-distant, dipping portions of the interface, increasing the calculated depth. By a similar mechanism, the depth underestimates in the northern portion of the basin may be due to a tilted basement contact on the flanks of the Kingston Arch. Localized extreme gradients may impact recordings throughout the basin, which could explain the somewhat high inter-event standard deviations (>0.05s) seen at many stations. (Although, we generally attribute these high standard deviations to noisy seismograms due to the urban environment).

Tualatin Basin Depth Estimates

Depth to basement estimates for the 6 stations in the Tualatin Basin derived using S- and Sp-arrivals are shown in Figure 4.3B and listed in Table 4.2. We see a trend of increasing depth moving towards the center of the basin, with station QJBC seeing the shallowest depth of 2400 m, and stations QAMI and SAIL sharing the deepest depth of 4200 m. The Texaco Cooper Mountain #1 exploration well, located 7km southwest from station QJBC (denoted as "Well" on Figure 4.3B), shows that the Siletz Formation is encountered at 2635 m, which corresponds well with the estimated depth-to-basement under station QJBC (DOGAMI, 2020). The only other study that has attempted to generate a 3-D model of depth-to-basement in the Tualatin Basin is McPhee et al., 2014, which inverted for depth using a dense network of gravimeter measurements. All but one of the depths estimated in this study are within 500 m of the depths estimated in that study. Station QNZO displays the largest discrepancy, for which we estimate a depth that is ~800 m deeper than that predicted by McPhee et al., 2014. QNZO is located near the northern edge of the Beaverton Fault Zone, across which the basement is estimated to experience more than 1000 m of offset (McPhee et al., 2014). As in the Seattle Basin, the

complex basement geometry adjacent to the fault zone may have led to smearing of the gravity inversions, resulting in an underestimate of depth-to-basement. In general, the standard deviations of the differential travel times are elevated, with most values at or near 0.05 s, but lower on average than those in the Seattle Basin. Despite having a lower degree of environmental noise, the Tualatin Basin Sp-arrivals are typically more emergent than those in the Seattle Basin. This difference may be partially attributable to scattering from high-impedance-contrast layers imbedded within the basin (e.g., the CRBG), or to a less sharp basement interface. It is important to note that the standard deviations for the $T_{Ps\text{-}P}$ values are all below 0.05 s, implying that waves from earthquakes with different depths and back-azimuths are following essentially the same ray-paths within the Tualatin Basin, affirming that the ray-paths are near-vertical.

Because $T_{Ps\text{-}P}$ is consistently smaller than $T_{S\text{-}Sp}$ at all of the Tualatin Basin stations, we assume that the Ps-phase is generated at a material interface within the basin. Considering the Ps-phase travel time, the layer is likely located between the bottom of the CRBG and the basement contact. We calculate the depth to this unknown interface using a similar method as that used in the depth-to-basement calculation. However, rather than generating a new velocity model, we iterate through the velocity model corresponding to the best-fit basement depth at each station, minimizing the residual between the predicted and observed $T_{Ps\text{-}P}$ value. These depths are shown in Figure 4.5 and listed in Table 4.2. At all stations, the conversion is generated from an interface around 1500-2000 m shallower than the basement contact and follows a similar trend of increasing in depth towards the center of the basin. In reviewing the lithology log from the Texaco Cooper Mountain #1 well near QJBC, we note a 300 m-thick sequence of high-velocity volcanic materials encountered at 976 m depth (DOGAMI, 2020). This layer corresponds well to our calculated conversion depth at station QJBC. Therefore, we suggest that the Ps conversion is

generated off of this layer of volcanic materials, which must have a large lateral extent within the basin. Based on the stratigraphic location of this interface, it is possible the materials represent a member of the Eocene Goble Volcanics, which flowed down from the Cascades and are present in thick (up to 1000 m) deposits in the Nehalem Basin to the north (Wells et al., 2020). Other possibilities include flows from the Eocene Tillamook Volcanics, or intrusive basalt sills that manifest on the east flank of the Coast Range (Ray Wells, personal comm., 2020).

Seattle Basin Attenuation Estimates

The Qp-Qs relationship for stations in the Seattle Basin are shown in Figure 4.6A. Table 4.3 describes the slope of the spectral ratio curve for each station, its correlation coefficient, its standard deviation, and the number of records used to calculate the relationship. Compared to other studies that have applied the same method (Chen, Chiu, and Yang 1994; Clouser and Langston 1991), standard deviations for the spectral slope values in the Seattle Basin stations are comparable or slightly higher. Stations with the highest standard deviations (>0.015) are located either at the basin's eastern (ALCT) or southern margin (ALKI, KDK, SP2), where stations are adjacent to the basement interface and the bounding fault zone. In these areas, slight variations in raypath may cause a wave to sample significantly more of the near-fault fracture zone or Quaternary sediments, and the amount of attenuation may vary from one record to the next. The south basin stations are also some of the noisiest of the group, sitting adjacent to Seattle's industrial district.

Li et al. 2006 derived 1- and 2-dimensional Qp-Qs models for the Seattle Basin by inverting active source seismic refraction data. They found the Qp/Qs ratio ranges from 1.0 to 1.6 for seismic waves with frequencies between 1 and 10 Hz. We plot this range and their average calculated Qp/Qs value of 1.2 as a line in Figure 4.6. If we assume their relation extends

to waves with frequencies up to 25 Hz, then we estimate an average Qp of 73, with most Qp values ranging from 60-88; the average Qs is 60, with most Qs values ranging from 49-72. Pratt and Brocher 2006 calculated simple spectral ratios (SSRs) of small earthquakes recorded within and outside of the Seattle Basin; by looking at the spectral slope of their ratios, they were able to derive average values for frequency-independent Qs throughout the basin. The Qs beneath the majority of their analyzed stations fell between 40 and 80, which agrees well with the range of Qs values estimated by our analysis, assuming the same average Qp/Qs relationship as in Li et al. 2006.

Tualatin Basin Attenuation Estimates

The Qp-Qs relationship generated using the Sp- and S-arrivals at the Tualatin Basin stations are shown in Figure 4.6B, and the corresponding spectral slopes are in Table 4.3. On average, the standard deviation of the Tualatin Basin's Sp-S spectral slopes are higher than those in the Seattle Basin. Again, this is likely related to the weaker, more emergent Sp-arrivals, which are more difficult to precisely pick.

In comparing the Qp-Qs curves between the two basins, it is evident that the Tualatin Basin is generally more attenuating than the Seattle Basin. This difference may arise from a variety of factors related to the quality and composition of basin materials. One possible explanation could be differences in the amount of pore fluid saturation. Winkler & Nur, 1982, note that the degree of pore fluid saturation has a significant effect on observed Qp/Qs values. In a comparison of sandstones at varying degrees of fluid saturation, they observe that Qs is approximately equal to Qp for dry stone, Qs > Qp for stone at 90% fluid saturation, and Qs < Qp for fully saturated stone. If we assume the Tualatin Basin's curve reflects a Qp/Qs value that is greater than the Seattle Basin's, it may imply that the materials within Tualatin Basin are closer

to full saturation. However, it is not uncommon to see significant variations in Qp and Qs from one basin to another. Using the same method applied in this paper, Clouser and Langston, 1991, interrogate average attenuation values beneath seismometers in a 1.4 km-deep sedimentary basin in the Gazli region of Uzbekistan. They found that for frequencies between 2-25 Hz, average Qp ranges between 50 and 70, while Qs ranges between 20 and 50. A similar study for seismometers near the New Madrid Fault Zone in the Mississippi Embayment found average Qp ranging from 25 to 60 and Qs ranging from 25 to 30 in sediments sequences 0.46 to 0.72 km-thick (Chen, Chiu, and Yang 1994). Therefore, the difference between the average attenuation relationships in the Seattle and Tualatin Basins is not unprecedented. Despite forming in the same forearc region, the processes that controlled the creation of each basin and the sources of the geologic material that filled them differ in many ways. Defining what exactly in the structure and geology leads to these differences would likely require more detailed, in-situ attenuation measurements.

We plot the Qp-Qs relation derived from the Tualatin Basin P- and Ps-arrivals in Figure 4.6B as well. Since we assume the Ps-phase is associated with a conversion off of an imbedded layer, the Qp-Qs relation should specifically reflect the average attenuation in the basin above that layer. As such, comparing the relationships in Figure 4.6B provides insight into how waves are attenuated as they travel at different depths within basin. In general, the P- and Ps-waves show less relative attenuation than the S- and Sp-waves. Because the calculation averages attenuation along a ray's path within the basin, this result implies that the materials below the imbedded layer may be more attenuating than those above the imbedded layer, assuming the Qp/Qs relation is relatively constant on both sides of the layer. However, the curves describing the relationship for each ratio fall within or near the other's standard deviation, so the difference may simply reflect the uncertainty in the observations.

4. Conclusions

Using observations of converted P- and S-waves from local earthquakes, we estimate the depth-to-basement and attenuation behavior beneath seismometers in the Seattle and Tualatin Basins. Depths are calculated considering the differential travel time between direct seismic wave arrivals and their associated converted phases generated at the bottom of the basin and internal interfaces. For the Seattle Basin, the depth calculation employs average velocity values from an existing tomographically-derived velocity model (Stephenson et al., 2017), whereas velocity values in the Tualatin Basin are derived from regional well data. Interface depths calculated for the Seattle and Tualatin Basins generally agree with existing estimates from other geophysical methods. We also map the depth to a layer of spatially-extensive volcanic materials within the Tualatin Basin, which produces a clear Ps conversion evident in seismic records.

Relationships between average Qp and Qs in the basins are defined using spectral ratios between the parent and converted phases (Clouser and Langston 1991). In applying the predicted linear Qp/Qs relationship of Li et al., 2006, we calculate an average Qp of 73 and a Qs of 60 in the Seattle Basin. This Qs value falls within the range estimated for the Seattle Basin in the independent analysis of Pratt & Brocher, 2006. Similar analysis for the Tualatin Basin reveals a higher degree of average attenuation than in the Seattle Basin, though in a range that is still consistent with global sedimentary basins. Regardless, the difference between the basins implies that, for the purpose of ground motion simulation, the same attenuation model should not be applied in both areas. Further analysis of earthquake records or active source surveying is needed within the Tualatin Basin to help refine its attenuation model.

Because of the agreement between the results in this paper and those of prior studies, we suggest that the methods herein would be useful if applied in basins with little prior structural

characterization. Namely, basins in areas with a moderate amount of local seismicity and long-term monitoring, but with little or no geophysical characterization. Paired with a reasonable estimate of velocity structure, the methods may be used to develop simple depth-to-basement models that are useful in geologic characterization, seismic hazard analysis, and earthquake source characterization.

5. Supplement I: Description of sources and values for velocity data within the Tualatin Basin

All well data in this section was taken from the Oregon Department of Geology and Mineral Industries' oil and gas well log viewer (DOGAMI, 2020). Velocity in the lower portion of the fluvial sediments was calculated by averaging the P-wave velocity in the 1000 ft of sediments above the CRBG contact in the Oregon Natural Gas DeShazer 13-22 well (1620 m/s); likewise, the value of the CRBG volcanics was determined by averaging the velocity in the 500 ft of CRBG volcanics sampled in the DeShazer 13-22 well (4950 m/s). Velocity at the top of the Eocene/Oligocene marine sediments was chosen by averaging the upper 1000 ft of the Nahama and Weagent Klohs 1 well (2500 m/s). And velocity in the basement material was calculated by averaging the upper 900 ft of the Siletz Formation encountered in the Reserve Bruer 1 well (3800 m/s). For the basin sediments directly above the Siletz formation (i.e., the bottom of the Yamhill Formation), a velocity of 3600 m/s was chosen, which parallels the 200 m/s difference seen at the basin/basement interface in the Seattle Basin (Stephenson et al., 2017).

6. Figures

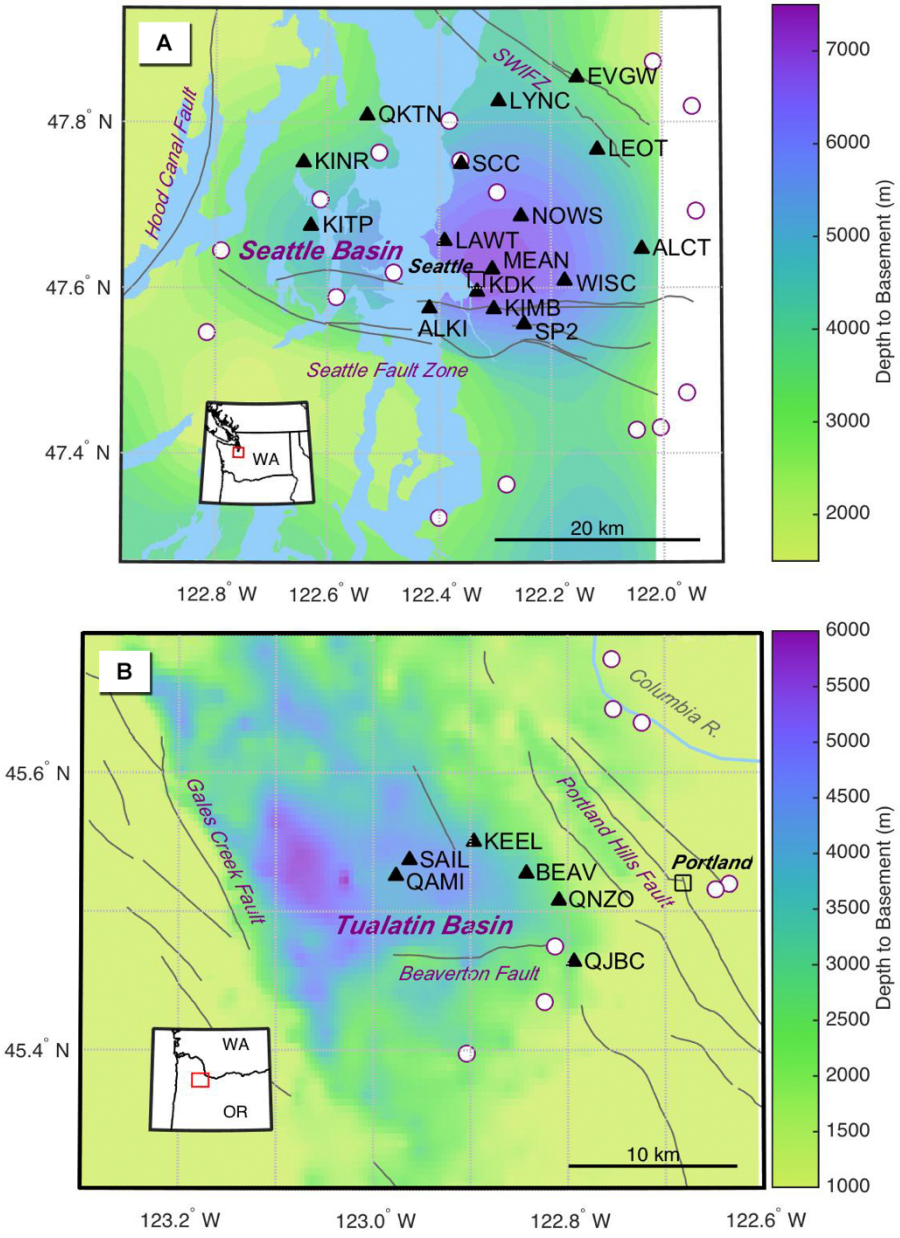

Figure 4.1. Maps of the study regions.
Stations (black triangles) and earthquakes (white circles) used in the analysis of (A) the Seattle Basin and (B) the Tualatin Basin. Depth-to-basement values in the Seattle Basin were taken from the Stephenson et al., 2017, Cascadia Velocity Model (CVM); Tualatin Basin depths were taken from McPhee et al., 2014. SWIFZ = Southern Whidbey Island Fault Zone.

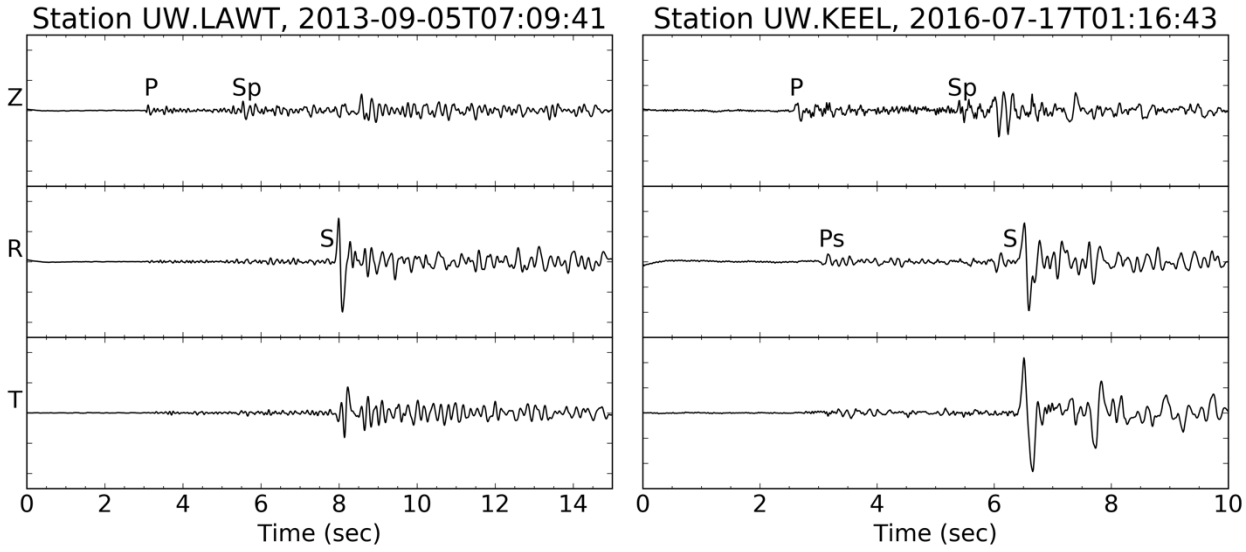

Figure 4.2. Three-component seismograms from Seattle Basin station LAWT and Tualatin Basin station KEEL showing the different converted phase arrival times.

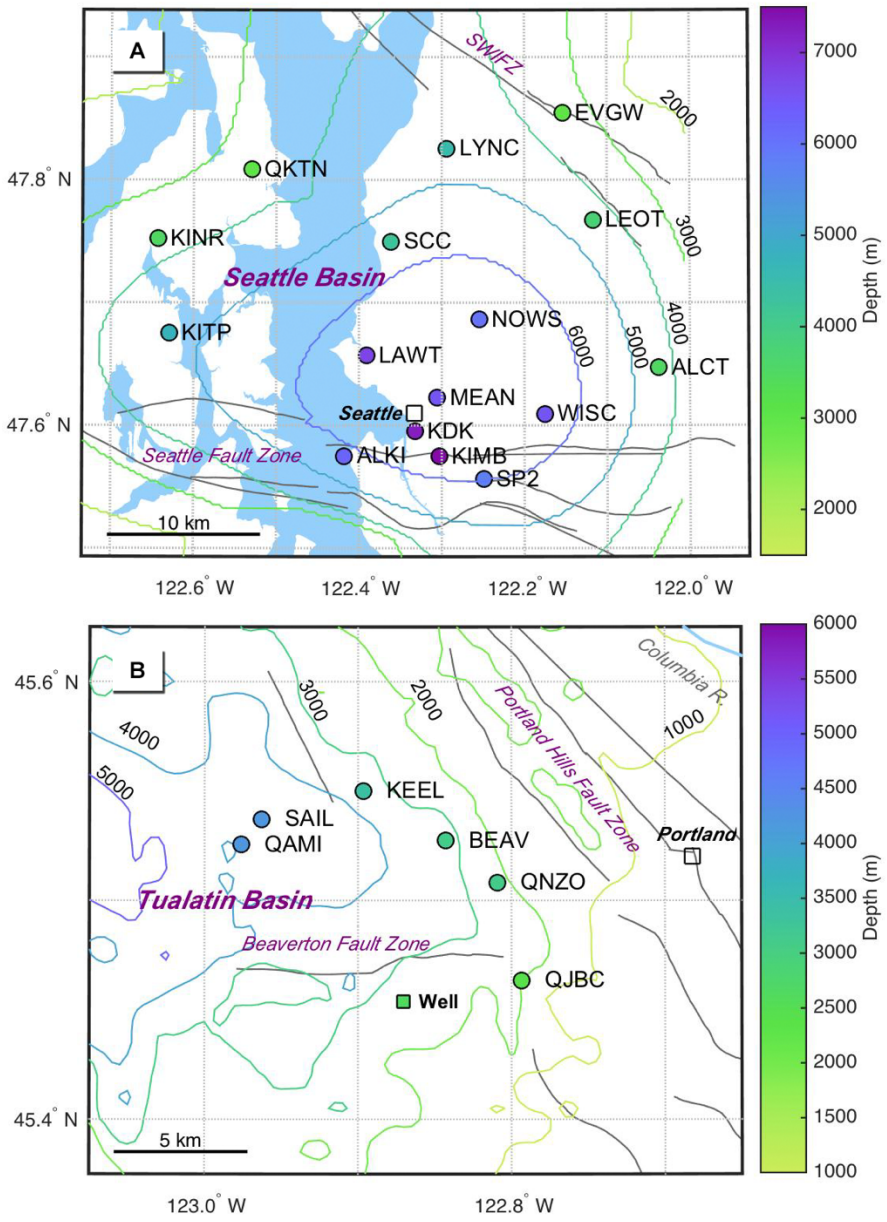

Figure 4.3. Estimated depth-to-basement at stations in (A) the Seattle Basin and (B) the Tualatin Basin based on this study (colored circles).
Depth contours in the Seattle Basin were taken from the Stephenson et al., 2017, Cascadia Velocity Model (CVM); Tualatin Basin contours were taken from McPhee et al., 2014.

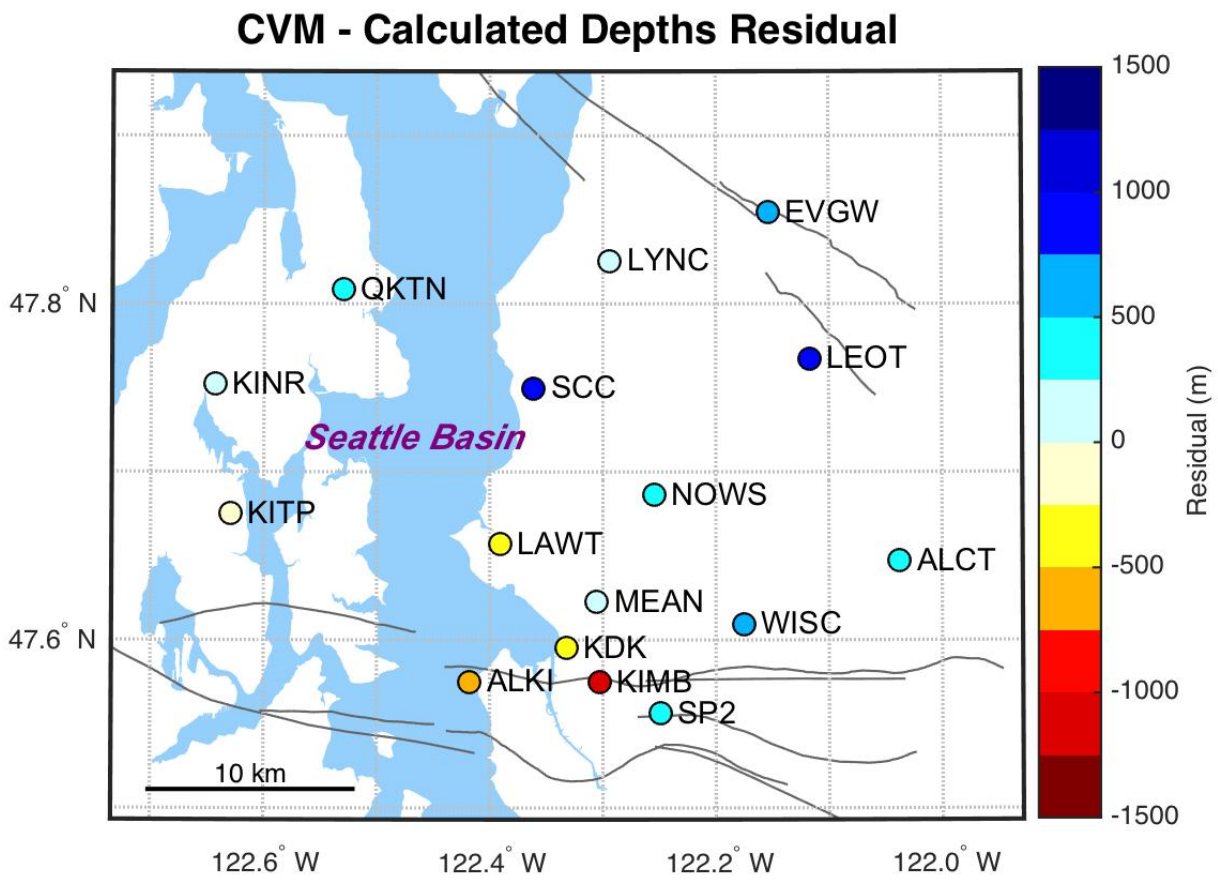

Figure 4.4. Map of residuals between the depth-to-basement values estimated in the Cascadia Velocity Model (CVM) and the values calculated in this study.
A positive residual implies that the calculated depth-to-basement is shallower than predicted by the CVM.

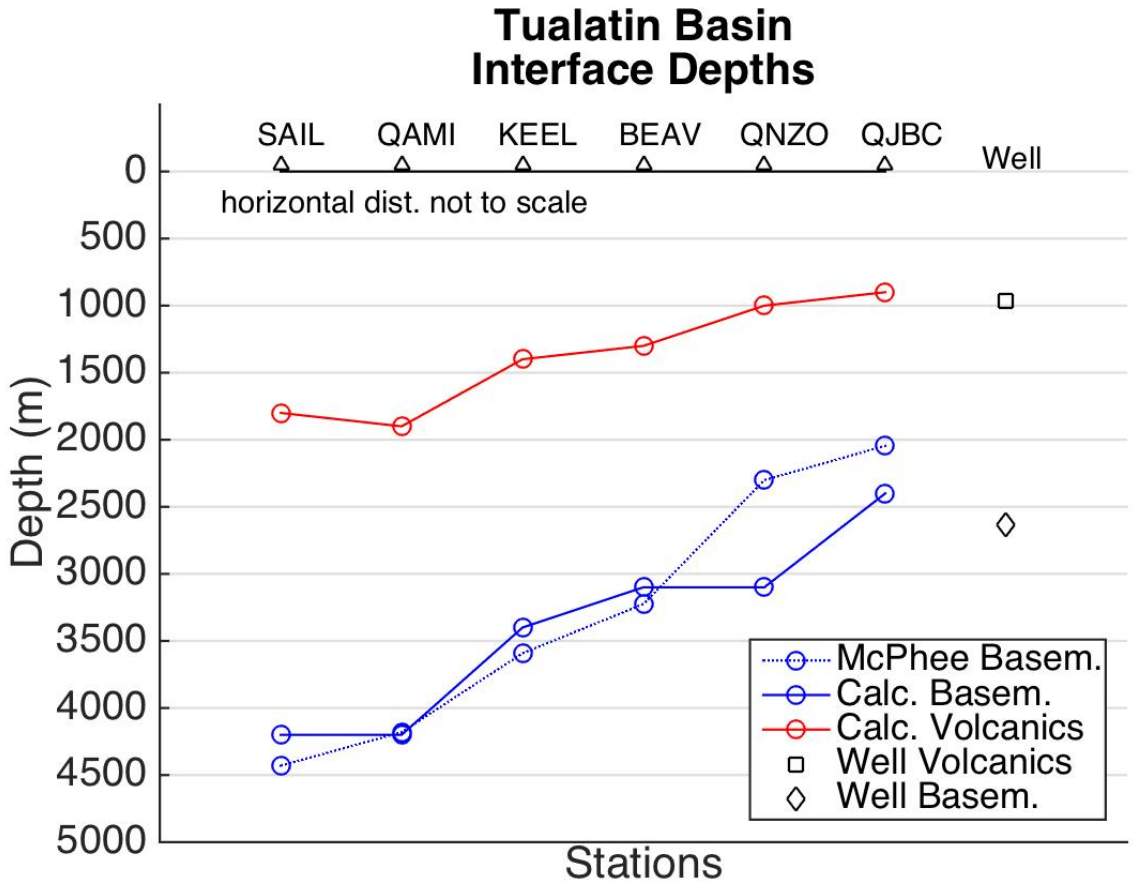

Figure 4.5. Estimated depths of interfaces beneath stations in the Tualatin Basin.
The stations are listed in an approximately northwest-to-southeast order. The solid blue line represents the depth-to-basement values calculated in this study, while the dotted blue line represents the depth-to-basement values from McPhee et al., 2014. The solid red line represents the estimated depth to the top of the imbedded volcanics layer. The black square and diamond represent the depth to the top of the volcanics layer and to the Siletz Fm., respectively, in the Texaco Cooper Mountain #1 well (DOGAMI, 2020).

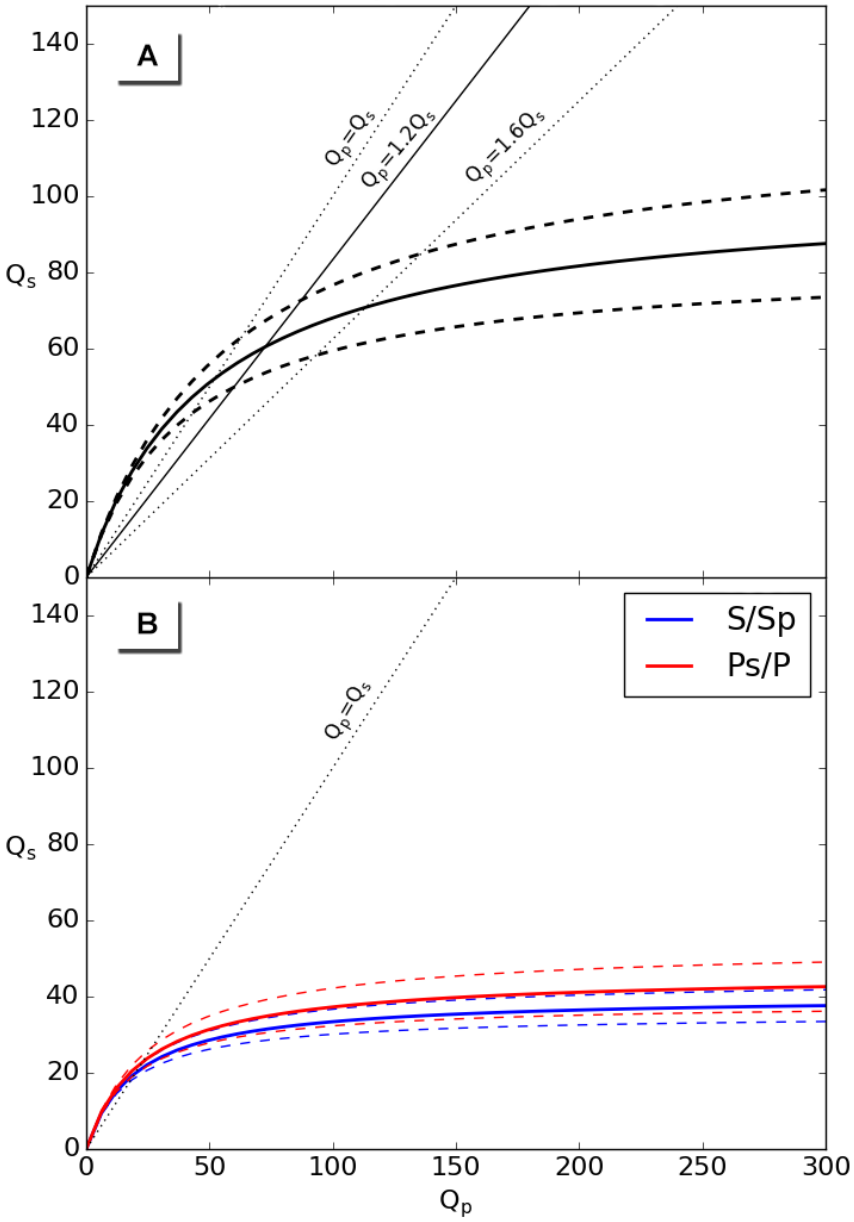

Figure 4.6. Averaged QP and QS relations (solid curves) and their standard deviations (dashed curves) for the Seattle and Tualatin Basin.
(A) Seattle Basin attenuation relations. Solid and dotted lines represent the range of Seattle Basin Q_P/Q_S relations presented in Li et al., 2006. (B) Tualatin Basin attenuation relations. The red curve represents the attenuation relationship derived using Ps- and P-arrivals, while the blue curve represents the attenuation relationship derived using the S- and Sp-arrivals.

7. Tables

Table 4.1: Differential travel times and depth estimates for Seattle Basin stations. T_{S-Sp} is the average differential S and Sp phase travel time; SD is the standard deviation of the average T_{S-Sp} value; and the residual describes the difference between the Cascadia Velocity Model (CVM) and calculated basin depth values.

Station	T_{S-Sp} (sec)	SD (sec)	No. Data	Calculated Depth (m)	CVM Depth (m)	Residual (m)
ALCT	1.31	0.16	2	3750	4200	450
ALKI	2.03	0.04	2	6250	5700	-550
EVGW	1.03	0.01	2	2750	3300	550
KDK	2.52	0.05	5	7250	6900	-350
KIMB	2.45	0.28	2	7500	6300	-1200
KINR	1.55	0.09	3	3500	3600	100
KITP	1.90	0.07	5	4750	4500	-250
LAWT	2.40	0.03	3	6750	6300	-450
LEOT	1.34	0.12	2	3750	4500	750
LYNC	1.55	0.32	4	4500	4500	0
MEAN	2.46	0.01	2	6750	6900	150
NOWS	2.18	0.14	2	6000	6300	300
QKTN	1.12	0.03	3	3000	3300	300
SCC	1.64	0.06	3	4250	5100	850
SP2	1.91	0.11	3	5750	6000	250
WISC	2.16	0.12	2	5750	6300	550

Table 4.2. Differential travel times and depth estimates for Tualatin Basin stations. T_{S-Sp} is the average differential S and Sp phase travel time, and T_{Ps-P} is the average differential Ps and P travel time; SD is the standard deviation of the average differential travel time value; and the residual describes the difference between the McPhee et al., 2014, basin depth estimates and the estimates calculated in this study.

Station	T_{S-Sp}, or T_{Ps-P} (sec)	SD (sec)	No. Data	Calculated Depth (m)	McPhee Depth (m)	Residual (m)
S & Sp-Phases:						
BEAV	1.03	0.06	7	3100	3225	125
SAIL	1.46	0.01	3	4200	4430	230
KEEL	1.11	0.05	4	3400	3592	192
QAMI	1.47	0.07	2	4200	4180	-20
QJBC	0.70	-	1	2400	2045	-355
QNZO	1.02	0.06	3	3100	2301	-799
P & Ps-Phases:						

BEAV	0.51	0.04	8	1300	-	-
SAIL	0.78	0.02	4	1800	-	-
KEEL	0.53	0.02	4	1400	-	-
QAMI	0.8	0.02	2	1900	-	-
QJBC	0.29	-	1	900	-	-
QNZO	0.40	0.02	3	1000	-	-

Table 4.3. Spectral ratio slopes for the Seattle and Tualatin Basins. SD is the standard deviation of the spectral ratio data with respect to the slope.

Station	**Slope (sec)**	**Intercept**	**Correlation Coefficient**	**SD**	**No. Data**
Seattle Basin:					
ALCT	0.080	-0.833	0.653	0.019	2
ALKI	0.114	-0.766	0.804	0.017	2
EVGW	0.089	-1.492	0.898	0.009	2
KDK	0.138	-2.089	0.887	0.015	2
KIMB	0.116	-1.231	0.922	0.010	2
KINR	0.118	-1.613	0.975	0.007	3
KITP	0.090	-1.140	0.940	0.011	5
LAWT	0.187	-2.557	0.975	0.011	3
LEOT	0.074	-0.507	0.778	0.012	2
LYNC	0.074	-1.276	0.813	0.011	2
MEAN	0.131	-1.423	0.957	0.008	2
NOWS	0.164	-2.209	0.926	0.010	1
SCC	0.084	-0.873	0.767	0.014	2
SP2	0.110	-0.283	0.849	0.017	3
QKTN	0.080	-1.080	0.897	0.010	3
WISC	0.137	-1.280	0.922	0.012	2
Tualatin Basin:					
Slopes from Ps/P Ratios					
BEAV	0.060	-0.368	0.897	0.012	8
KEEL	0.079	-0.297	0.794	0.017	4
QAMI	0.135	-0.201	0.922	0.012	2
QJBC	0.038	0.049	0.453	0.011	1
QNZO	0.060	-0.151	0.684	0.016	3
SAIL	0.083	-0.213	0.841	0.015	4
Slopes from S/Sp Ratios					
BEAV	0.172	-3.078	0.987	0.011	7
KEEL	0.199	-2.820	0.966	0.015	4

QAMI	0.238	-3.276	0.940	0.018	1
QNZO	0.139	-2.262	0.899	0.017	3
SAIL	0.205	-3.003	0.979	0.011	3

V. Summary and Future Work

In this thesis, we explored three different problems related to seismic hazard and earthquake science in the Pacific Northwest.

In the first chapter, we investigated the present-day distribution of microseismicity in the Cascadia Subduction Zone by developing a catalog of earthquakes recorded on ocean bottom seismometers (OBS). Of the recorded earthquakes, 271 had epicenters located between the deformation front and the shoreline. We observed that the distribution of near-plate-interface earthquakes follows a distinct along-strike trend, which we relate to changes in the surface roughness of the subducting plate and the volume of subducted sediments.

We then explored how topography affects estimates of earthquake ground motions by simulating M7 Seattle Fault earthquakes in a 3-D model space considering surface topography. We demonstrated that average ground motions in models with topography are near those predicted in flat models, though significant amplifications were common. Ground motion amplification was greatest at the top of topographic features (e.g., hilltops, cliffs, and ridge crests), while ground motions were less amplified (or de-amplified) at topographic lows (e.g., the foot of cliffs, valley bottoms, and channel bottoms). This amplification was most significant in S- and surface waves and had little effect on P-waves. Generally, amplification at the top of a topographic feature was greatest near a characteristic resonance frequency and at an azimuth perpendicular to the feature's primary axis of elongation. However, variability in amplification was high from one event to the next, likely due to the influence of localized focusing and scattering of seismic waves.

Finally, we employed converted phases from local earthquakes to calculate the depth to basement in the Seattle and Tualatin Basins. By using simple estimates of the 1-D velocity

model, we successfully reproduced basin depths estimated from other geophysical surveys. We additionally mapped the depth to the surface of an imbedded volcanics layer in the Tualatin Basin. Then, by taking the spectral ratio between converted and parent seismic phases, we were able to estimate a Qp-Qs relationship within both basins, finding that the Tualatin Basin likely attenuates body waves more significantly than the Seattle Basin.

The findings presented here will be built upon and improved as more work is done to clarify lingering uncertainties in regional geologic structure. Perhaps the most direct way future work will benefit is through refinements in velocity structure. Offshore, large-scale, active source seismic surveys are planned that will improve the velocity model in the accretionary wedge. With these new velocity models, the earthquakes we located in Chapter 2 may be relocated, which would likely help to reduce uncertainty in event locations. Onshore, better resolution of shallow velocity structure (namely, the distribution and depth of shallow soil layers) will allow us to adequately account for soil resonance in earthquake simulations considering topography. The recent publication of regionally extensive soil profiles should make this task somewhat easier (Ahdi et al., 2017), and additional work in the Issaquah Alps and on the Kitsap Peninsula would further improve results.

With respect to the simulations of topographic effects, further tests exploring lower magnitude finite fault earthquakes (~M6) would help resolve questions around the variability of topographic response with source location. The location of the source never technically changed in the M7 simulations, so the sensitivity of topographic effects to source location was not well tested. An M6 test would allow us to move the source location along the fault surface and better constrain this sensitivity. Additionally, M6 tests would allow us to better constrain the effects of

directivity on topographic amplification, which is typically most influential off the ends of the fault plane.

Finally, more structural characterization is needed within the Tualatin Basin. Large-scale, active source seismic experiments would provide a means to both probe the depth of the basin, as well as its attenuation structure. Such information would be useful both for understanding the tectonic origin of the basin and for modeling earthquake wave propagation in the Portland metro area.

VI. Acknowledgements

The work in this thesis benefitted from the expertise and encouragement of many individuals. Firstly, I would like to thank Erin Wirth for her thoughtful advising and expertise over the last three years, particularly as I worked on getting my simulations running for my third chapter, as well as for encouraging me to research the strange signals that ultimately laid the foundations for my fourth chapter. I would like to thank John Vidale for giving me the opportunity to come to UW, and for always taking the time to provide guidance and answer my questions in the first two years of my graduate work.

The other members of my dissertation committee, including Ken Creager, Art Frankel, and Will Wilcock, have provided valuable guidance throughout my time at UW. From teaching classes, to reading drafts of my papers, to providing feedback on research ideas, much of my academic success has been facilitated through their patient work. Thank you to the coauthors on my first paper, including Emily Roland and Shuoshuo Han. Emily provided much help and resources in wrangling the CI data in Antelope, while Shuoshuo was critical in helping me interpret how her research was intrinsically tied to the earthquakes I detected. Thank you to Heidi Houston and David Schmidt, who were always happy to provide guidance when it was needed.

Additional thanks to the staff at the PNSN, including Paul Bodin, Renate Hartog, and Amy Wright, who have helped me pull and interpret regional seismic data on many occasions. To the USGS staff, particularly Joan Gomberg, Alex Grant, and Alicia Hotovec-Ellis, for their valuable insights. To the UW graduate community and the seismology research group, including Emma Myers, Carolyn Nuyen, Mika Thompson, Carl Ulberg, Shelley Chestler, Kelley Hall, and

Ariane Ducellier, for helping to build such a supportive research group. And to the ESS administrative and technical staff, for making my experience at UW run smoothly.

Finally, I would like to thank my family, who have always supported me on the long path to my doctorate. To my friends, who have been there to provide much needed distractions on the days when science was not cooperating. To Mike, for being a perpetual cheerleader. And finally, to Calin, the love of my life, for encouraging me to pursue my passion these last ten years, and for always being there to help me recognize my own potential.

VII. References

1. Chapter 1

Bucknam, R. C., Hemphill-haley, E., & Leopold, E. B. (1992). Abrupt Uplift within the Past 1700 Years at Southern Puget Sound , Washington. *Science*, *258*(5088), 1611–1614.

DeMets, C., Gordon, R. G., & Argus, D. F. (2010). Geologically current plate motions. *Geophysical Journal International*, *181*, 1–80. https://doi.org/doi: 10.1111/j.1365-246X.2009.04491.x

Goldfinger, C., Nelson, H. C., Morey, A. E., Johnson, J. E., Patton, J. R., Karabanov, E., Gutierrez-Pastor, J., Eriksson, A. T., Gracia, E., Dunhill, G., Enkin, R. J., Dallimore, A., & Vallier, T. (2012). *Turbidite event history — Methods and implications for Holocene paleoseismicity of the Cascadia subduction zone: USGS Professional Paper 1661-F*. https://pubs.usgs.gov/pp/pp1661f/

Nelson, A. R., Johnson, S. Y., Kelsey, H. M., Wells, R. E., Sherrod, B. L., Pezzopane, S. K., Bradley, L. A., Koehler, R. D., & Bucknam, R. C. (2003). Late Holocene earthquakes on the Toe Jam Hill fault, Seattle fault zone, Bainbridge Island, Washington. *Bulletin of the Geological Society of America*, *115*(11), 1388–1403. https://doi.org/10.1130/B25262.1

Pratt, T. L., Johnson, S., Potter, C., Stephenson, W., & Finn, C. (1997). Seismic reflection images beneath Puget Sound, western Washington State: The Puget Lowland thrust sheet hypothesis. *Journal of Geophysical Research: Solid Earth*, *102*(B12), 27469–27489. https://doi.org/10.1029/97JB01830

Satake, K., Wang, K., & Atwater, B. F. (2003). Fault slip and seismic moment of the 1700 Cascadia earthquake inferred from Japanese tsunami descriptions. *Journal of Geophysical Research*, *108*(B11, 2535). https://doi.org/10.1029/2003JB002521

Stone, I., Vidale, J. E., Han, S., & Roland, E. (2018). Catalog of Offshore Seismicity in Cascadia: Insights Into the Regional Distribution of Microseismicity and its Relation to Subduction Processes. *Journal of Geophysical Research: Solid Earth*, *123*(1), 641–652. https://doi.org/10.1002/2017JB014966

Wada, I., Wang, K., He, J., & Hyndman, R. D. (2008). Weakening of the subduction interface and its effects on surface heat flow, slab dehydration, and mantle wedge serpentinization. *Journal of Geophysical Research: Solid Earth*, *113*(4), 1–15. https://doi.org/10.1029/2007JB005190

Wells, R. E., Weaver, C. S., & Blakely, R. J. (1998). Fore-arc migration in Cascadia and its neotectonic significance. *Geology*, *26*(8), 759–762. https://doi.org/10.1130/0091-7613(1998)026<0759:FAMICA>2.3.CO;2

2. Chapter 2

Adam, J., Klaeschen, D., Kukowski, N., & Flueh, E. (2004). Upward delamination of Cascadia Basin sediment infill with landward frontal accretion thrusting caused by rapid glacial age material flux. *Tectonics*, *23*(3), 1–21. http://doi.org/10.1029/2002TC001475

Booth-Rea, G., Klaeschen, D., Grevemeyer, I., & Reston, T. (2008). Heterogeneous deformation in the Cascadia convergent margin and its relation to thermal gradient (Washington, NW

USA). *Tectonics*, *27*(4), 1–15. http://doi.org/10.1029/2007TC002209
Burgette, R. J., Weldon, R. J., & Schmidt, D. A. (2009). Interseismic uplift rates for western Oregon and along-strike variation in locking on the Cascadia subduction zone. *Journal of Geophysical Research: Solid Earth*, *114*(B1), 1–24. http://doi.org/10.1029/2008JB005679
Canales, J. P., Carbotte, S. M., Nedimovic, M. R., & Carton, H. (2017). Dry Juan de Fuca slab revealed by quantification of water entering Cascadia subduction zone. *Nature Geoscience, 10,* 864-870. http://doi.org/10.1038/ngeo3050
Chen, X., & McGuire, J. J. (2016). Measuring earthquake source parameters in the Mendocino Triple Junction region using a dense OBS array: implications for fault strength variations. *Earth and Planetary Science Letters*, *453*. 276–287. http://doi.org/10.1016/j.epsl.2016.08.022
Contreras-Reyes, E., & Osses, A. (2010). Lithospheric flexure modelling seaward of the Chile trench: Implications for oceanic plate weakening in the Trench Outer Rise region. *Geophysical Journal International*, *182*(1), 97–112. http://doi.org/10.1111/j.1365-246X.2010.04629.x
DeMets, C., Gordon, R. G., & Argus, D. F. (2010). Geologically current plate motions. *Geophysical Journal International*, *181*, 1–80. http://doi.org/doi: 10.1111/j.1365-246X.2009.04491.x
Dziak, R., Hammond, S., & Fox, C. (2011). A 20-Year Hydroacoustic Time Series of Seismic and Volcanic Events in the Northeast Pacific Ocean. *Oceanography*, *24*(3), 280–293. http://doi.org/10.5670/oceanog.2011.79
Flueh, E. R., Fisher, M. A., Bialas, J., Childs, J. R., Klaeschen, D., Kukowski, N., … Vidal, N. (1998). New seismic images of the cascadia subduction zone from cruise SO 108-ORWELL. *Tectonophysics*, *293*(1–2), 69–84. http://doi.org/10.1016/S0040-1951(98)00091-2
Gerdom, M., Tréhu, A. M., Flueh, E. R., & Klaeschen, D. (2000). The continental margin off oregon from seismic investigations. *Tectonophysics*, *329*(1–4), 79–97. http://doi.org/10.1016/S0040-1951(00)00190-6
Goldfinger, C., Nelson, C. H., & Johnson, J. E. (2003). Holocene earthquake records from the Cascadia subduction zone and northern San Andreas fault based on precise dating of offshore turbidites. *Annual Review of Earth and Planetary Sciences*, *31*, 555–577. http://doi.org/10.1146/annurev.earth.31.100901.141246
Goldfinger, C., Nelson, H. C., Morey, A. E., Johnson, J. E., Patton, J. R., Karabanov, E., … Vallier, T. (2012). *Turbidite event history — Methods and implications for Holocene paleoseismicity of the Cascadia subduction zone: USGS Professional Paper 1661-F*. Retrieved from https://pubs.usgs.gov/pp/pp1661f/
Gulick, S. P. S., Meltzer, A. M., & Clarke, S. H. (1998). Seismic structure of the southern Cascadia subduction zone and accretionary prism north of the Mendocino triple junction. *Journal of Geophysical Research*, *103*(B11), 27207-27222. http://doi.org/10.1029/98JB02526
Gulick, S. P. S., Meltzer, A. S., Henstock, T. J., & Levander, A. (2001). Internal deformation of the southern Gorda plate: Fragmentattion of a weak plate near the Mendocino triple junction. *Geology*, *29*(8), 691–694. http://doi.org/10.1130/0091-7613(2001)029<0691:IDOTSG>2.0.CO;2
Gulick, S. P. S., & Meltzer, A. S. (2002). Effect of the northward-migrating Mendocino triple junction on the Eel River forearc basin, California: Structural evolution. *Bulletin of the*

Geological Society of America, 114(12), 1505-1519. http://doi.org/10.1130/0016-7606(2002)114<1505:EOTNMM>2.0.CO;2

Han, S., Bangs, N., Carbotte, S., Saffer, D., & Gibson, J. (2017). Links between sediment consolidation and Cascadia megathrust slip behavior, *Nature Geoscience, 10,* 954-959. http://doi.org/10.1038/s41561-017-0007-2

Han, S., Carbotte, S. M., Canales, J. P., Nedimovic, M. R., Carton, H., Gibson, J. C., & Horning, G. W. (2016). Seismic reflection imaging of the Juan de Fuca plate from ridge to trench: New constraints on the distribution of faulting and evolution of the crust prior to subduction. *Journal of Geophysical Research B: Solid Earth*, *121*(3), 1849–1872. http://doi.org/10.1002/2015JB012416

Havskov, J., & Ottemoller, L. (2010). Magnitudes. *Routine data processing in earthquake seismology: With sample data, exercises and software* (pp. 151-188).

Horning, G., Canales, J. P., Carbotte, S. M., Han, S., Carton, H., Nedimović, M. R., & van Keken, P. E. (2016). A 2-D tomographic model of the Juan de Fuca plate from accretion at axial seamount to subduction at the Cascadia margin from an active source ocean bottom seismometer survey. *Journal of Geophysical Research: Solid Earth*, *121*(8), 5859–5879. http://doi.org/10.1002/2016JB013228

Hyndman, R. D., Riddihough, R. P., & Herzer, R. (1979). The Nootka Fault Zone - a new plate boundary off western Canada. *Geophysical Journal International*, *58*(3), 667–683. http://doi.org/10.1111/j.1365-246X.1979.tb04801.x

Hyndman, R. D., & Wang, K. (1995). The rupture zone of Cascadia great earthquakes from current defomration and the thermal regime. *Journal of Geophysical Research*, *100*(B11), 22133–22154.

Jennings, P. C., & Kanamori, H. (1983). Effect of distance on local magnitudes found from strong-motion records. *Bulletin of the Seismological Society of America, 73*(1), 265-280.

Klein, F. W. (2002). *User's guide to HYPOINVERSE-2000, a Fortran program to solve for earthquake locations and magnitudes: USGS Open File Report 02-171*.

MacKay, M. E. (1995). Structural variation and landward vergence at the toe of the Oregon accretionary prism. *Tectonics*, *14*(6), 1309–1320. http://doi.org/10.1029/95TC02320

MacKay, M. E., Moore, G. F., Cochrane, G. R., Casey Moore, J., & Kulm, L. V. D. (1992). Landward vergence and oblique structural trends in the Oregon margin accretionary prism: Implications and effect on fluid flow. *Earth and Planetary Science Letters*, *109*(3–4), 477–491. http://doi.org/10.1016/0012-821X(92)90108-8

McCaffrey, R., King, R. W., Payne, S. J., & Lancaster, M. (2013). Active tectonics of northwestern U.S. inferred from GPS-derived surface velocities. *Journal of Geophysical Research: Solid Earth*, *118*(2), 709–723. http://doi.org/10.1029/2012JB009473

McCrory, P. a., Blair, J. L., Waldhauser, F., & Oppenheimer, D. H. (2012). Juan de Fuca slab geometry and its relation to Wadati-Benioff zone seismicity. *Journal of Geophysical Research: Solid Earth*, *117*(9), 1–24. http://doi.org/10.1029/2012JB009407

Morton, E. A., & Bilek, S. L. (2015). Preliminary Event Detection of Earthquakes Using the Cascadia Initiative Data. *Seismological Research Letters*, *86*(5), 1270–1277. http://doi.org/10.1785/0220150098

Nishikawa, T., & Ide, S. (2017). Detection of earthquake swarms at subduction zones globally : insights into tectonic controls on swarm activity. *Journal of Geophysical Research: Solid Earth*, *122*, 5325–5343. http://doi.org/10.1002/2017JB014188

Obana, K., Kodaira, S., & Kaneda, Y. (2006). Seismicity related to heterogeneous structure

along the western Nankai trough off Shikoku Island. *Geophysical Research Letters*, *33*(23), 1–5. http://doi.org/10.1029/2006GL028179

Obana, K., Scherwath, M., Yamamoto, Y., Kodaira, S., Wang, K., Spence, G., … Kao, H. (2015). Earthquake Activity in Northern Cascadia Subduction Zone Off Vancouver Island Revealed by Ocean-Bottom Seismograph Observations. *Bulletin of the Seismological Society of America*, *105*(1). http://doi.org/10.1785/0120140095

Oppenheimer, D., Beroza, G., Carver, G., Dengler, L., Eaton, J., Gee, L. S., … Valentine, D. (1993). The Cape Mendocino, California, earthquakes of April 1992 - Subduction at the triple junction. *Science*, *261*(5120), 433–438. http://doi.org/10.1126/science.261.5120.433

Richter, C. F. (1935). An instrumental earthquake magnitude scale. *Bulletin of the Seismological Society of America, 25*(1), 1-32.

Saffer, D. M., & Tobin, H. J. (2011). Hydrogeology and Mechanics of Subduction Zone Forearcs: Fluid Flow and Pore Pressure. *Annual Review of Earth and Planetary Sciences*, *39*(1), 157–186. http://doi.org/10.1146/annurev-earth-040610-133408

Satake, K., Wang, K., & Atwater, B. F. (2003). Fault slip and seismic moment of the 1700 Cascadia earthquake inferred from Japanese tsunami descriptions. *Journal of Geophysical Research*, *108*(B11, 2535). http://doi.org/10.1029/2003JB002521

Scherwath, M., Spence, G., Obana, K., Kodaira, S., Wang, K., Riedel, M., … Collins, J. (2011). Seafloor Seismometers Monitor Northern Cascadia Earthquakes. *EOS, Transactions, American Geophysical Union*, *92*(47), 421–440. http://doi.org/10.1029/2006GL028179.Wang

Schmalzle, G. M., McCaffrey, R., & Creager, K. C. (2014). Central Cascadia subduction zone creep. *Geochemistry, Geophysics, Geosystems*, *15*(4), 1515–1532. http://doi.org/10.1002/2013GC005172

Toomey, D. R., Allen, R. M., Barclay, A. H., Bell, S. W., Bromirski, P. D., Carlson, R. L., … Wilcock, W. S. D. (2014). A Sea Change In Seismological Studies of Subduction Zones. *Oceanography*, *27*(2), 138–150. http://doi.org/10.5670/oceanog.2014.49

Tréhu, A. M., Blakely, R. J., & Williams, M. C. (2012). Subducted seamounts and recent earthquakes beneath the central cascadia forearc. *Geology*, *40*(2), 103–106. http://doi.org/10.1130/G32460.1

Tréhu, A. M., Braunmiller, J., & Davis, E. (2015). Seismicity of the Central Cascadia Continental Margin near 44.5 N: A Decadal View. *Seismological Research Letters*, *86*(3), 819–829. http://doi.org/10.1785/0220140207

Tréhu, A. M., Braunmiller, J., & Nabelek, J. L. (2008). Probable low-angle thrust earthquakes on the Juan de Fuca-North America plate boundary. *Geology*, *36*(2), 127–130. http://doi.org/10.1130/G24145A.1

Unruh, J., & Humphrey, J. (2017) Seismogenic deformation between the Sierran microplate and Oregon Coast block, California, USA. *Geology, 45*(5), 415-418. http://doi.org/10.1130/G38696.1

Wang, K., & Bilek, S. L. (2014). Invited review paper: Fault creep caused by subduction of rough seafloor relief. *Tectonophysics*, *610*, 1–24. http://doi.org/10.1016/j.tecto.2013.11.024

Wang, K., & Tréhu, A. M. (2016). Invited review paper: Some outstanding issues in the study of great megathrust earthquakes-The Cascadia example. *Journal of Geodynamics*, *98*, 1–18. http://doi.org/10.1016/j.jog.2016.03.010

Williams, M. C., Tréhu, A. M., & Braunmiller, J. (2011). Seismicity at the Cascadia plate boundary beneath the Oregon continental shelf. *Bulletin of the Seismological Society of*

America, *101*(3), 940–950. http://doi.org/10.1785/0120100198
Wilson, D. S. (1993). Confidence intervals for motion and deformation of the Juan de Fuca plate. *Journal of Geophysical Research, 98*(B9), 16053-16071. http://dx.doi.org/10.1029/93JB01227

3. Chapter 3

Abrahamson, N. A., Silva, W. J., & Kamai, R. (2014). Summary of the ASK14 ground motion relation for active crustal regions. *Earthquake Spectra*, *30*(3), 1025–1055. https://doi.org/10.1193/070913EQS198M
Allstadt, K., Vidale, J. E., & Frankel, A. D. (2013). A scenario study of seismically induced landsliding in seattle using broadband synthetic seismograms. *Bulletin of the Seismological Society of America*, *103*(6), 2971–2992. https://doi.org/10.1785/0120130051
Ashford, S. A., & Sitar, N. (1997). Analysis of topographic amplification of inclined shear waves in a steep coastal bluff. *Bulletin of the Seismological Society of America*, *87*(3), 692–700.
Bard, P. Y. (1982). Diffracted waves and displacement field over two dimensional topographies. *Geophys. J. R. Astron. Soc.*, *71*(March), 731–760.
Blakely, R. J., Wells, R. E., Weaver, C. S., & Johnson, S. Y. (2002). Location, structure, and seismicity of the Seattle fault zone, Washington: Evidence from aeromagnetic anomalies, geologic mapping, and seismic-reflection data. *Bulletin of the Geological Society of America*, *114*(1), 169–177. https://doi.org/10.1130/0016-7606(2002)114<0169:LSASOT>2.0.CO;2
Boore, D. M. (1972). A note on the effect of simple topography on seismic SH waves. *Bulletin of the Seismological Society of America*, *62*(1), 275–284.
Boore, D. M., Stewart, J. P., Seyhan, E., & Atkinson, G. M. (2014). NGA-West2 equations for predicting PGA, PGV, and 5% damped PSA for shallow crustal earthquakes. *Earthquake Spectra*, *30*(3), 1057–1085. https://doi.org/10.1193/070113EQS184M
Bouchon, M., Schultz, C. A., & Toksöz, M. N. (1996). Effect of three-dimensional topography on seismic motion. *Journal of Geophysical Research*, *101*(B3), 5835–5846.
Brune, J. N. (1970). Tectonic stress and the spectra of seismic shear waves from earthquakes. *Journal of Geophysical Research*, *75*(26), 4997–5009. https://doi.org/10.1029/JB075i026p04997
Campbell, K. W., & Bozorgnia, Y. (2014). NGA-West2 ground motion model for the average horizontal components of PGA, PGV, and 5% damped linear acceleration response spectra. *Earthquake Spectra*, *30*(3), 1087–1114. https://doi.org/10.1193/062913EQS175M
Celebi, M. (1987). Topographical and geological amplifications determined from strong-motion and aftershock records of the 3 March 1985 Chile earthquake. *Bulletin of the Seismological Society of America*, *77*(4), 1147–1167.
Chiou, B. S. J., & Youngs, R. R. (2014). Update of the Chiou and Youngs NGA model for the average horizontal component of peak ground motion and response spectra. *Earthquake Spectra*, *30*(3), 1117–1153. https://doi.org/10.1193/072813EQS219M
Davis, L. L., & West, L. R. (1973). Observed effects of topography on ground motion. *Bulletin of the Seismological Society of America*, *63*(1), 747–763.
Fichtner, A. The spectral-element method. *Full Seismic Waveform Modelling and Inversion.* Kolumban Hutter, Ed. New York: Springer. 2011. Pp. 182-210.
Finlayson, D. P., 2005. Combined bathymetry and topography of the Puget Lowland,

Washington State. University of Washington. https://www.ocean.washington.edu/data/pugetsound/psdem2005.html. (Accessed September 2020).
Frankel, A. (2013). Rupture history of the 2011 M 9 Tohoku Japan earthquake determined from strong-motion and high-rate GPS recordings: Subevents radiating energy in different frequency bands. *Bulletin of the Seismological Society of America*, *103*(2B), 1290–1306. https://doi.org/10.1785/0120120148
Frankel, A. D., Carver, D. L., & Williams, R. A. (2002). Nonlinear and linear site response and basin effects in Seattle for the M 6.8 Nisqually, Washington, earthquake. *Bulletin of the Seismological Society of America*, *92*(6), 2090–2109. https://doi.org/10.1785/0120010254
Frankel, A. D., Stephenson, W. J., & Carver, D. (2009). Sedimentary Basin Effects in Seattle , Washington : Ground-Motion Observations and 3D Simulations. *Bulletin of the Seismological Society of America*, *99*(3), 1579–1611. https://doi.org/10.1785/0120080203
Frankel, A. D., Stephenson, W. J., Carver, D. L., Williams, R. A., Odum, J. K., & Rhea, S. (2007). Seismic Hazard Maps for Seattle, Washington, Incorporating 3D Sedimentary Basin Effects, Nonlinear Site Response, and Rupture Directivity. In *USGS Open File Report 2007-1175*.
Frankel, A. D., Thorne, P., & Rohay, A. (2014). *Three-dimensional ground-motion simulations of earthquakes for the Hanford Area, Washington, USGS Open-File Report 2013-1289*. https://doi.org/10.3133/ofr20131289
Frankel, A. D., Wirth, E. A., Marafi, N., Vidale, J., & Stephenson, W. J. (2018). Broadband synthetic seismograms for magnitude 9 earthquakes on the cascadia megathrust based on 3D simulations and stochastic synthetics, Part 1: Methodology and overall results. *Bulletin of the Seismological Society of America*, *108*(5), 2347–2369. https://doi.org/10.1785/0120180034
Geli, L., Bard, P.-Y., & Jullien, B. (1988). The effect of topography on earthquake ground motion: A review and new results. *Bulletin of the Seismological Society of America*, *78*(1), 42–63.
Hartzell, S. H., Carver, D. L., & King, K. W. (1994). Initial investigation of site and topographic effects at Robinwood Ridge, California. *Bulletin - Seismological Society of America*, *84*(5), 1336–1349.
Hartzell, S., Harmsen, S., & Frankel, A. (2010). Effects of 3D random correlated velocity perturbations on predicted ground motions. *Bulletin of the Seismological Society of America*, *100*(4), 1415–1426. https://doi.org/10.1785/0120090060
Hartzell, S., Meremonte, M., Ramírez-Guzmán, L., & McNamara, D. (2014). Ground motion in the presence of complex topography: Earthquake and ambient noise sources. *Bulletin of the Seismological Society of America*, *104*(1), 451–466. https://doi.org/10.1785/0120130088
Hough, S. E., Altidor, J. R., Anglade, D., Given, D., Janvier, M. G., Maharrey, J. Z., Meremonte, M., Mildor, B. S. L., Prepetit, C., & Yong, A. (2010). Localized damage caused by topographic amplification during the 2010 M7.0 Haiti earthquake. *Nature Geoscience*, *3*(11), 778–782. https://doi.org/10.1038/ngeo988
Imperatori, W., & Mai, P. M. (2015). The role of topography and lateral velocity heterogeneities on near-source scattering and ground-motion variability. *Geophysical Journal International*, *202*(3), 2163–2181. https://doi.org/10.1093/gji/ggv281
Komatitsch, D., Liu, Q., Tromp, J., Süss, P., Stidham, C., & Shaw, J. H. (2004). Simulations of ground motion in the Los Angeles basin based upon the spectral-element method. *Bulletin*

of the Seismological Society of America, *94*(1), 187–206. https://doi.org/10.1785/0120030077

Lovati, S., Bakavoli, M.K.H., Massa, M. *et al.* Estimation of topographical effects at Narni ridge (Central Italy): comparisons between experimental results and numerical modelling. *Bull Earthquake Eng* **9,** 1987–2005 (2011). https://doi.org/10.1007/s10518-011-9315-x

Magnoni, F., Casarotti, E., Michelini, A., Piersanti, A., Komatitsch, D., Peter, D., & Tromp, J. (2014). Spectral-element simulations of seismic waves generated by the 2009 L'Aquila earthquake. *Bulletin of the Seismological Society of America*, *104*(1), 73–94. https://doi.org/10.1785/0120130106

Mai, P. M., & Beroza, G. C. (2002). A spatial random field model to characterize complexity in earthquake slip. *Journal of Geophysical Research: Solid Earth*, *107*(B11), ESE 10-1-ESE 10-21. https://doi.org/10.1029/2001jb000588

Martel, L., Munasinghe, M., & Farnell, G. W. (1977). Transmission and reflection of Rayleigh wave through a step. *Bulletin of the Seismological Society of America*, *67*(5), 1277–1290.

Massa, M., Barani, S., & Lovati, S. (2014). Overview of topographic effects based on experimental observations: Meaning, causes and possible interpretations. *Geophysical Journal International*, *197*, 1537–1550. https://doi.org/10.1093/gji/ggt341

Moschetti, M. P., Hartzell, S., Ramírez-Guzmán, L., Frankel, A. D., Angster, S. J., & Stephenson, W. J. (2017). 3D ground-motion simulations of Mw 7 earthquakes on the Salt Lake City segment of the Wasatch Fault Zone: Variability of long-period ($T \geq 1$ s) ground motions and sensitivity to kinematic rupture parameters. *Bulletin of the Seismological Society of America*, *107*(4), 1704–1723. https://doi.org/10.1785/0120160307

Paolucci, R. (2002). Amplification of earthquake ground motion by steep topographic irregularities. *Earthquake Engineering and Structural Dynamics*, *31*(10), 1831–1853. https://doi.org/10.1002/eqe.192

Pedersen, H., Le Brun, B., Hatzfeld, D., Campillo, M., & Bard, P. Y. (1994). Ground-motion amplitude across ridges. *Bulletin of the Seismological Society of America*, *84*(6), 1786–1800.

Pischiutta, M., Cultrera, G., Caserta, A., Luzi, L., & Rovelli, A. (2010). Topographic effects on the hill of Nocera Umbra, central Italy. *Geophysical Journal International*, *182*(2), 977–987. https://doi.org/10.1111/j.1365-246X.2010.04654.x

Ramachandran, K., Hyndman, R. D., & Brocher, T. M. (2006). Regional P wave velocity structure of the Northern Cascadia Subduction Zone. *Journal of Geophysical Research: Solid Earth*, *111*(12), 1–15. https://doi.org/10.1029/2005JB004108

Rodgers, A. J., Petersson, N. A., & Sjogreen, B. (2010). Simulation of topographic effects on seismic waves from shallow explosions near the North Korean nuclear test site with emphasis on shear wave generation. *Journal of Geophysical Research: Solid Earth*, *115*(11). https://doi.org/10.1029/2010JB007707

Sánchez-Sesma, F. J. (1990). Elementary solutions for response of a wedge-shaped medium to incident SH and SV waves. *Bulletin of the Seismological Society of America*, *80*(3), 737–742.

Sánchez-Sesma, F. J., Herrera, I., & Avilés, J. (1982). A boundary method for elastic wave diffracation: Application to scattering of SH waves by surface irregularities. *Bulletin of the Seismological Society of America*, *72*(2), 473–490.

Sánchez-Sesma, F. (1985). Diffraction of Elastic Sh Waves By Wedges. *Bulletin of the Seismological Society of Americae Seismological Society of America*, *75*(5), 1435–1446.

https://doi.org/10.2138/am-2001-2-311
Somerville, P., Irikura, K., Graves, R., Sawada, S., Wald, D., Abrahamson, N., Iwasaki, Y., Kagawa, T., Smith, N., & Kowada, A. (1999). Characterizing Crustal Earthquake Slip Models for the Prediction of Strong Ground Motion. *Seismological Research Letters*, *70*(1), 59–80. https://doi.org/10.1785/gssrl.70.1.59
Spudich, P., Hellweg, M., & Lee, W. H. K. (1996). Directional topographic site response at Tarzana observed in aftershocks of the 1994 Northridge, California, earthquake: Implications for mainshock motions. *Bulletin of the Seismological Society of America*, *86*(1B), S193–S208.
Stephenson, W. J., Reitman, N. G., & Angster, S. J. (2017). P- and S-wave velocity models incorporating the Cascadia subduction zone for 3D earthquake ground motion simulations—Update for Open-File Report 2007–1348. In *USGS Open File Report 2017-1152*. https://doi.org/10.3133/ofr20171152
Stolte, A. C., Cox, B. R., & Lee, R. C. (2017). An experimental topographic amplification study at Los Alamos national laboratory using ambient vibrations. *Bulletin of the Seismological Society of America*, *107*(3), 1386–1401. https://doi.org/10.1785/0120160269
Thompson, M., Wirth, E. A., Frankel, A. D., Hartog, J. R., & Vidale, J. E. (2020). Basin amplification effects in the Puget Lowland, Washington, from strong-motion recordings and 3D simulations. *Bulletin of the Seismological Society of America*, *110*(2), 534–555. https://doi.org/10.1785/0120190211
U.S. Geological Survey (USGS), 2017. 1/3rd arc-second Digital Elevation Models (DEMs). https://www.usgs.gov/core-science-systems/ngp/3dep. Last accessed 21 Sept., 2020.
Wirth, E. A., Chang, S. W., & Frankel, A. D. (2018). *2018 report on incorporating sedimentary basin response into the design of tall buildings in Seattle, Washington: USGS Open-File Report 2018-1149*. https://doi.org/10.3133/ofr20181149
Wirth, E. A., Frankel, A. D., Marafi, N., Vidale, J. E., & Stephenson, W. J. (2018). Broadband synthetic seismograms for magnitude 9 earthquakes on the cascadia megathrust based on 3D simulations and stochastic synthetics, Part 2: Rupture parameters and variability. *Bulletin of the Seismological Society of America*, *108*(5), 2370–2388. https://doi.org/10.1785/0120180029
Wirth, E. A., Frankel, A. D., & Vidale, J. E. (2017). *Evaluating a Kinematic Method for Generating Broadband Ground Motions for Great Subduction Zone Earthquakes : Application to the 2003 M w 8 . 3 Tokachi-Oki Earthquake*. *107*(4), 1737–1753. https://doi.org/10.1785/0120170065

4. Chapter 4

Asimaki, Domniki, Kami Mohammadi, Henry B. Mason, Rachel K. Adams, Sudhir Rajaure, and Diwakar Khadka. 2017. "Observations and Simulations of Basin Effects in the Kathmandu Valley during the 2015 Gorkha, Nepal, Earthquake Sequence." *Earthquake Spectra* 33 (Special issue 1): S35–53. https://doi.org/10.1193/013117EQS022M.
Audet, Pascal, Michael G. Bostock, Devin C. Boyarko, Michael R. Brudzinski, and Richard M. Allen. 2010. "Slab Morphology in the Cascadia Fore Arc and Its Relation to Episodic Tremor and Slip." *Journal of Geophysical Research: Solid Earth* 115 (B00A16): 1–15. https://doi.org/10.1029/2008JB006053.
Blakely, Richard J., Ray E. Wells, Terry L. Tolan, Marvin H. Beeson, Anne M. Trehu, and Lee

M. Liberty. 2000. “New Aeromagnetic Data Reveal Large Strike-Slip (?) Faults Inthe Northern Willamette Valley, Oregon.” *Bulletin of the Geological Society of America* 112 (7): 1225–33. https://doi.org/10.1130/0016-7606(2000)112<1225:NADRLS>2.0.CO;2.

Blakely, Richard J., Ray E. Wells, Craig S. Weaver, and Samuel Y. Johnson. 2002. “Location, Structure, and Seismicity of the Seattle Fault Zone, Washington: Evidence from Aeromagnetic Anomalies, Geologic Mapping, and Seismic-Reflection Data.” *Bulletin of the Geological Society of America* 114 (1): 169–77. https://doi.org/10.1130/0016-7606(2002)114<0169:LSASOT>2.0.CO;2.

Brink, U. S. ten, P. C. Molzer, M. A. Fisher, R. J. Blakely, R. C. Bucknam, T. Parsons, R. S. Crosson, and K. C. Creager. 2002. “Subsurface Geometry and Evolution of the Seattle Fault Zone and the Seattle Basin, Washington.” *Bulletin of the Seismological Society of America* 92 (5): 1737–53. https://doi.org/10.1785/0120010229.

Brocher, Thomas M., Richard J. Blakely, and Ray E. Wells. 2004. “Interpretation of the Seattle Uplift, Washington, as a Passive-Roof Duplex.” *Bulletin of the Seismological Society of America* 94 (4): 1379–1401. https://doi.org/10.1785/012003190.

Brocher, Thomas M., Tom Parsons, Richard J. Blakely, Nikolas I. Christensen, Michael A. Fisher, and Ray E. Wells. 2001. “Upper Crustal Structure in Puget Lowland, Washington: Results from the 1998 Seismic Hazards Investigation in Puget Sound.” *Journal of Geophysical Research: Solid Earth* 106 (B7): 13541–64. https://doi.org/10.1029/2001jb000154.

Chen, KC, JM Chiu, and YT Yang. 1994. “Qp-Qs Relations in the Sedimentary Basin of the Upper Mississippi Embayment Using Converted Phases.” *Bulletin of the Seismological Society of America* 84 (6): 1861–68. http://www.bssaonline.org/content/84/6/1861.short.

Clouser, Robert H, and Charles A Langston. 1991. “Qp-Qs Relations in a Sedimentary Basin Using Converted Phases.” *Bulletin of the Seismological Society of America* 81 (3): 733–50. http://link.springer.com/10.1007/s00024-006-0158-3.

Frankel, Arthur D., David L. Carver, and Robert A. Williams. 2002. “Nonlinear and Linear Site Response and Basin Effects in Seattle for the M 6.8 Nisqually, Washington, Earthquake.” *Bulletin of the Seismological Society of America* 92 (6): 2090–2109. https://doi.org/10.1785/0120010254.

Frankel, Arthur D., and William J. Stephenson. 2000. “Three-Dimensional Simulations of Ground Motions in the Seattle Region for Earthquakes in the Seattle Fault Zone.” *Bulletin of the Seismological Society of America* 90 (5): 1251–67. https://doi.org/10.1785/0119990159.

Frankel, Arthur D., William J. Stephenson, and David Carver. 2009. “Sedimentary Basin Effects in Seattle , Washington : Ground-Motion Observations and 3D Simulations.” *Bulletin of the Seismological Society of America* 99 (3): 1579–1611. https://doi.org/10.1785/0120080203.

Hartzell, Stephen, Edward Cranswick, Arthur Frankel, David Carver, and Mark Meremonte. 1997. “Variability of Site Response in the Los Angeles Urban Area.” *Bulletin of the Seismological Society of America* 87 (6): 1377–1400.

Johnson, S. Y., C. J. Potter, and J. M. Armentrout. 1994. “Origin and Evolution of the Seattle Fault and Seattle Basin, Washington.” *Geology* 22 (1): 71–74. https://doi.org/10.1130/0091-7613(1994)022<0071:OAEOTS>2.3.CO;2.

Johnson, Samuel Y., Shawn V. Dadisman, Jonathan R. Childs, and William D. Stanley. 1999. “Active Tectonics of the Seattle Fault and Central Puget Sound, Washington - Implications for Earthquake Hazards.” *Bulletin of the Geological Society of America* 111 (7): 1042–53.

https://doi.org/10.1130/0016-7606(1999)111<1042:ATOTSF>2.3.CO;2.
Jones, Francis Avery. 1996. "Thickness of Unconsolidated Deposits in the Puget Sound Lowland, Washington and British Columbia." *Water-Resources Investigations Report 94-4133*.
Kawase, H. 1996. "The Cause of the Damage Belt in Kobe: 'The Basin-Edge Effect,' Constructive Interference of the Direct S-Wave with the Basin-Induced Diffracted/Rayleigh Waves." *Seismological Research Letters* 67 (5): 25–34. https://doi.org/10.1785/gssrl.67.5.25.
Li, Qin, William S.D. Wilcock, Thomas L. Pratt, Catherine M. Snelson, and Thomas M. Brocher. 2006. "Seismic Attenuation Structure of the Seattle Basin, Washington State from Explosive-Source Refraction Data." *Bulletin of the Seismological Society of America* 96 (2): 553–71. https://doi.org/10.1785/0120040164.
Liberty, Lee M., and Thomas L. Pratt. 2008. "Structure of the Eastern Seattle Fault Zone, Washington State: New Insights from Seismic Reflection Data." *Bulletin of the Seismological Society of America* 98 (4): 1681–95. https://doi.org/10.1785/0120070145.
McPhee, D. K., V. E. Langenheim, R. E. Wells, and R. J. Blakely. 2014. "Tectonic Evolution of the Tualatin Basin, Northwest Oregon, as Revealed by Inversion of Gravity Data." *Geosphere* 10 (2): 264–75. https://doi.org/10.1130/GES00929.1.
Newton, V. C. 1969. "Subsurface Geology of the Lower Columbia and Willamette Basins, Oregon: Oil and Gas Investigations No. 2." *State of Oregon Department of Geology and Mineral Industries*.
Oregon Department of Geology and Mineral Industries (DOGAMI), 2020, Oil & Gas Well Log Viewer. https://www.oregongeology.org/mlrr/oilgas-logs.htm. (Accessed July 2020).
Planke, S., and H. Cambray. 1998. "Seismic Properties of Flood Basalts from Hole 917A Downhole Data, Southeast Greenland Volcanic Margin." In *Proceedings of the Ocean Drilling Program: Scientific Results*, edited by A. D. Saunders, H. C. Larsen, and S. W. Wise, 152:453–62. https://doi.org/10.2973/odp.proc.sr.152.247.1998.
Pratt, Thomas L., and Thomas M. Brocher. 2006. "Site Response and Attenuation in the Puget Lowland, Washington State." *Bulletin of the Seismological Society of America* 96 (2): 536–52. https://doi.org/10.1785/0120040200.
Pratt, Thomas L., Samuel Johnson, Christopher Potter, William Stephenson, and Carol Finn. 1997. "Seismic Reflection Images beneath Puget Sound, Western Washington State: The Puget Lowland Thrust Sheet Hypothesis." *Journal of Geophysical Research: Solid Earth* 102 (B12): 27469–89. https://doi.org/10.1029/97JB01830.
Pratt, Thomas L., Kathy G. Troost, Jack K. Odum, and William J. Stephenson. 2015. "Kinematics of Shallow Backthrusts in the Seattle Fault Zone, Washington State." *Geosphere* 11 (6): 1948–74. https://doi.org/10.1130/GES01179.1.
Ramachandran, K., R. D. Hyndman, and T. M. Brocher. 2006. "Regional P Wave Velocity Structure of the Northern Cascadia Subduction Zone." *Journal of Geophysical Research: Solid Earth* 111 (12): 1–15. https://doi.org/10.1029/2005JB004108.
Snelson, Catherine M., Thomas M. Brocher, Kate C. Miller, Thomas L. Pratt, and Anne M. Tréhu. 2007. "Seismic Amplification within the Seattle Basin, Washington State: Insights from SHIPS Seismic Tomography Experiments." *Bulletin of the Seismological Society of America* 97 (5): 1432–48. https://doi.org/10.1785/0120050204.
Stephenson, William J., Arthur D. Frankel, Jack K. Odum, Robert A. Williams, and Thomas L. Pratt. 2006. "Toward Resolving an Earthquake Ground Motion Mystery in West Seattle,

Washington State: Shallow Seismic Focusing May Cause Anomalous Chimney Damage." *Geophysical Research Letters* 33 (6): 2–5. https://doi.org/10.1029/2005GL025037.
Stephenson, William J, Nadine G Reitman, and Stephen J Angster. 2017. "P- and S-Wave Velocity Models Incorporating the Cascadia Subduction Zone for 3D Earthquake Ground Motion Simulations—Update for Open-File Report 2007–1348." *USGS Open File Report 2017-1152*. https://doi.org/10.3133/ofr20171152.
Wagoner, T. M. Van, R. S. Crosson, K. C. Creager, G. Medema, L. Preston, N. P. Symons, and T. M. Brocher. 2002. "Crustal Structure and Relocated Earthquakes in the Puget Lowland, Washington, from High-Resolution Seismic Tomography." *Journal of Geophysical Research: Solid Earth* 107 (B12): ESE 22-1-ESE 22-23. https://doi.org/10.1029/2001jb000710.
Wells, R.E., Haugerud, R.A., Niem, A.R., Niem, W.A., Ma, L., Evarts, R.C., O'Connor, J.E., Madin, I.P., Sherrod, D.R.,Beeson, M.H., Tolan, T.L., Wheeler, K.L., Hanson, W.B., and Sawlan, M.G., 2020, Geologic map of the greater Portland metropolitan area and surrounding region, Oregon and Washington: *U.S. Geological Survey Scientific Investigations Map 3443,* pamphlet 55 p., 2 sheets, scale 1:63,360. https://doi.org/10.3133/sim3443.
Wells, Ray E., Craig S. Weaver, and Richard J. Blakely. 1998. "Fore-Arc Migration in Cascadia and Its Neotectonic Significance." *Geology* 26 (8): 759–62. https://doi.org/10.1130/0091-7613(1998)026<0759:FAMICA>2.3.CO;2.
Werner, K. S., E. P. Graven, and T. A. Berkman. 1991. "Direction of Maximum Horizontal Compression in Western Oregon Determined by Borehole Breakouts." *Tectonics* 10 (5): 948–58.
Yeats, R.S., Graven, E.P., Werner, K.S., Goldfinger, C., and Popowski, T.A., 1996, Tectonics of the Willamette Valley, Oregon, in Rogers, A.M., et al., eds., *Assessing earthquake hazards and reducing risk in the Pacific Northwest: U.S. Geological Survey Professional Paper 1560*, p. 183–222.

5. Chapter 5

Ahdi, S. K., Stewart, J. P., Ancheta, T. D., Kwak, D. Y., & Mitra, D. (2017). Development of Vs profile database and proxy-based models for Vs30 prediction in the pacific northwest region of North America. *Bulletin of the Seismological Society of America*, *107*(4), 1781–1801. https://doi.org/10.1785/0120160335